Dottorato di Fisica

Università degli Studi di Pisa
Scuola di Dottorato in Scienze di base, "G. Galilei"

Université Paris-Sud XI

Ph.D. Thesis

Reaction and Structure Models for Nuclei Far from Stability

Candidate:

Guillaume Blanchon

(XX Ciclo)

Supervisors

Dr. Angela Bonaccorso, Dr. Nicolas Alamanos, Prof. T. Suomijärvi.

June 2008

Contents

Introduction

In a pioneer experiment, in the 80's, Tanihata et al. [1] measured the interaction cross sections for all known Li isotopes (^{6}Li-^{11}Li). In this first experiments the interest was focused on what is the probability that the projectile enters into interaction with the target so that it does not emerge as the same nucleus. The authors extracted the root mean square radii (rms) of those isotopes from the interaction cross sections with a Glauber model. The nucleus ^{11}Li showed to have a remarkably large radius suggesting a large deformation or a long tail in the matter distribution. This experiment opened the way to more studies on exotic nuclei. By exotic, we mean nuclei that contain many more or many fewer neutrons than a stable isotope of the same element. In the chart of nuclei, see Fig. 1, they lie far from the stability line. Therefore their ground states are usually unstable against $\beta-$decay. Their lifetime is, typically, of the order of a millisecond to a second, which is much longer than the time scale ('the period') of nucleonic motion ($\sim 10^{-23}$s) inside the nucleus. Therefore, these exotic nuclei have lifetimes long enough to posses well-defined many-body structures as bound (or quasibound) systems of nucleons. The main interest of these nuclei is that they exhibit unusual features unkown in stable nuclei such as halo, neutron skin or new magic numbers. These phenomena were not clearly expected on the basis of the models developed to reproduce characteristics of stable nuclei. Indeed, they have required a number of new treatments. Because of their rapid decay, it is rather difficult to make targets with them, even if new techniques, such as chemical methods, are starting to be available. Therefore exotic nuclei so far have been studied by forming secondary beams of them from a primary reaction product. Going back to the case of ^{11}Li, it is observed that much of the increased cross section comes from neutron removal channels. Moreover, for these processes, the momentum distribution of the core fragment has been found to be anomalously narrow, from which it has been inferred that neutrons are removed from orbits whose momentum distribution is narrow. According to the uncertainty principle, this implies large spatial distribution of the neutron(s) removed with respect to the residue. These observations have been accounted for by the hypothesis that these nuclei have neutron halos. The peculiarity of this structure is that the valence neutrons have a very high probability of presence at a large distance from the core. These distances are larger than the typical dimension of the mean-field of light nuclei. This means that they are tunneling well outside the classically allowed region. Thus halo nuclei have been considered as inert cores surrounded by one or two external nucleons. As we shall see

in the following, the assumption of an inert core should be treated with caution when the core nucleus has a low excitation energy. The binding of the halo nucleons to the core is extremely weak, so that they are likely to be kicked off during collisions. Up to now, only one- and two-neutron halo nuclei have been observed. The best known are ^{11}Be (with a one-neutron halo), and ^{6}He, ^{11}Li and ^{14}Be (with two-neutron halo). The existence of proton halos has been suggested in some proton-rich nuclei, such as ^{8}B. However, the presence of the Coulomb potential for the halo proton reduces the tunneling probability and the fraction of the wave function found outside the core region is smaller in a proton halo as compared to a neutron halo state with the same separation energy and angular momentum. Up to now, ^{8}B is the only confirmed proton halo nucleus in its ground state.

The characteristic features of halo phenomena are connected not only with the specific structure

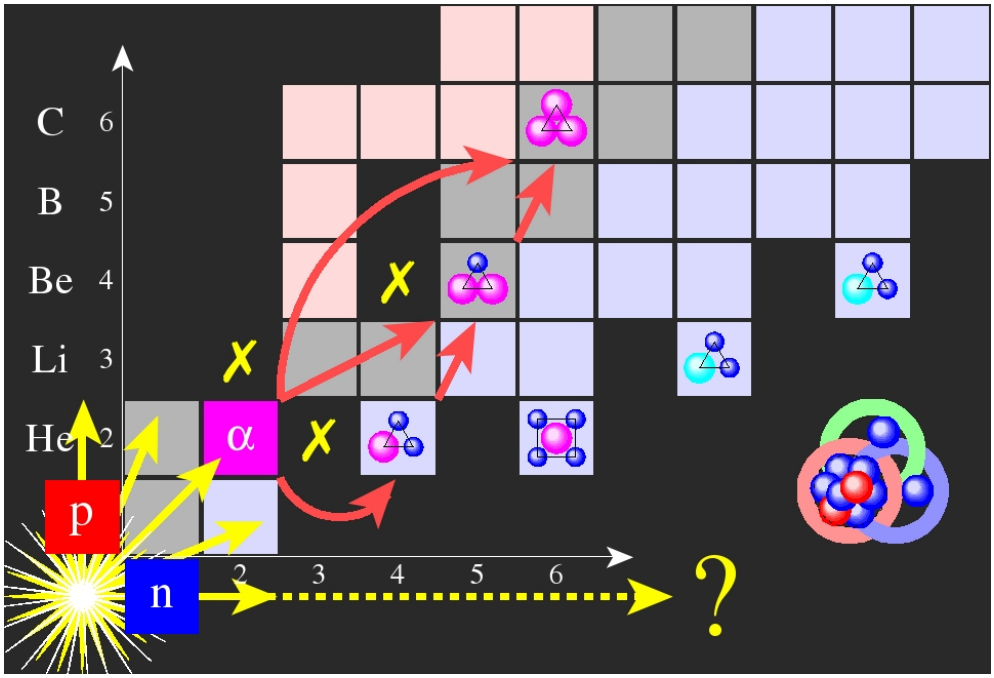

Figure 1: The Segré chart for light nuclei. The well established many-neutron haloes, ^{6,8}He, ^{11}Li and ^{14}Be, are indicated on the neutron drip line. Figure extracted from [2].

of the ground state wave function (weak binding and large extension) but also with excitation of halo degrees of freedom, reflected in the structure of the low-lying continuum which, near the three-body breakup threshold, reveals accumulation of the transition strength for different multipole excitations. In neutron-rich nuclei, in fact, a considerable dipole strength has been observed at low excitation energies. As an explanation for this, a new mode of dipole oscillation, the so-called soft dipole mode has been proposed. This mode has been visualized as an oscillation of the halo neutrons against the core. However it has been shown that the soft dipole mode is not a collective oscillation but rather a single particle threshold effect.

Over three decades ago, Efimov proposed a model, in which a three-body system can support bound states under conditions such that none of the three pairs constituting it are bound or one or two pairs are barely bound. He showed that regardless of the nature of the pair-wise interactions, when any pair is near the binding threshold (that is, large negative scattering length), an effective, attractive, inverse-quadratic potential in the radial variable of the three-body system supports an infinite number of weakly bound states. A system is called Borromean if it is bound

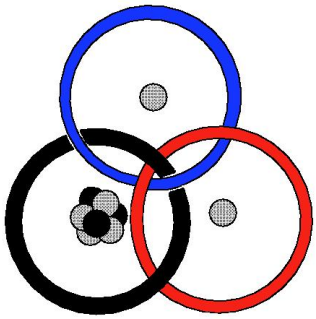

Figure 2: The three-body 'borromean' system ^{11}Li composed of two neutrons and a ^{9}Li core. When one bond is broken the system falls apart, just like the rings of the Borromean family crest.

but can be decomposed into three subsystems, any two of which cannot form a bound state, see Fig. 2. The name comes from the coat of arms of the famous Milanese family Borromeo. It contains three rings each of which is interlaced with the other two such that by breaking any of them, the other two release each other. The number of bound states for Borromean systems is almost always limited to the ground state. The effective two-body interactions must be weak enough to exclude bound states and strong enough to bind the three-body system. Therefore one or more two-body resonances must be present at low energy. A comprehensive review of the first twenty years of theoretical work on light exotic nuclei can be found in [3].

The theoretical approaches to the description of the two-neutron halo structure are mostly semi-phenomenological three-body calculations based on the core+n+n picture [4]-[7], see Fig. 3. The occupancy of the states of the core is generally taken into account by an orthogonality condition. It is investigated (i) whether the known three-body binding can be reproduced by two-body forces appropriate to the description of the subsystems, $C+n$ and $n+n$; (ii) whether the known properties of the system can be reproduced by a phenomenological adjustment of the interactions. The properties of core plus one-neutron system are essential and models rely on the knowledge of angular momentum and parity as well as energies and corresponding neutron-core effective potential. Therefore spectroscopic strength for neutron resonances in the field of the core. The reaction theory makes the link between these structure models and the experimental results.

Nuclear structure studies are primarily concerned with the properties of discrete states, i.e., bound states and resonances. In reactions, however, nuclear systems are in scattering states. The coupling between bound and scattering states is particularly important in nuclei far from stability. As a consequence, the interpretation of experimental results depends on a very critical way on the reliability of the reaction models. Coulomb breakup is of particular interest. In order to correctly extract information about the structure of these nuclei from experimental cross sections, an accurate theoretical description of this mechanism is necessary.

This work is concerned with the study of one- and two-neutron halo nuclei. There is also a final chapter presenting the prospectives for studies of heavier exotic systems. In a first part we shall concentrate on the study of reaction models and on the way to extract structure information. Then there is a chapter dealing with structure models for the Beryllium isotopes.

In the first two chapters, this thesis is concerned with transfer to the continuum and projectile fragmentation. Breakup reactions $N + A \rightarrow N' + C + n1 + n2$ involving a two-neutron Borromean nucleus scattered from a target represent at least a four-body problem. An exact solution has not been feasible up to now and approximate methods are required, these approximations are explained in the next sections. The reactions with halo nuclei are characterised by weakly bound projectiles, and that requires specific treatment. In conventional reaction theory, a weakly bound projectile poses a formidable problem: the coupling to continuum states should be taken into account because the breakup effects can become important in each channel. When, however, the projectile-target relative motion is much faster than that of the halo nucleons within the projectile, the situation becomes much simpler. In describing such reactions one can essentially neglect the inner motion in the nuclei, which is a kind of adiabatic approximation.

On the other hand, the study of unbound systems showing resonances very close to particle threshold is giving rise to the "spectroscopy in the continuum" [8] and some of the most recent applications have been discussed in Refs. [9]-[12]. Ideally one would like to study the neutron elastic scattering at very low energies on the ”core" nuclei. This is however not feasible at the moment as many such cores, like ^{9}Li, ^{12}Be or ^{15}B are themselves unstable and therefore they cannot be used as targets. Other indirect methods instead have been used so far, mainly aiming at the determination of the energy and angular momentum of the continuum states. This information should help fixing the parameters and form of the neutron-core interaction. We remind the reader that the problem of a consistent treatment of the nucleon-nucleus interaction yielding at the same time bound and unbound states has already been studied for normal nuclei [13, 14] and it would be extremely interesting to see how generalizations of such approaches could be obtained from studies of exotic nuclei.

The reactions used so far to study unbound nuclei from the experimental point of view can be grouped as: projectile breakup following which the neutron-core coincidences have been

recorded and the neutron energy spectrum relative to the core has been reconstructed [8], [15]-[18]; multiparticle transfer reactions [19, 20] or just one proton [9] transfer. In a few other cases, the neutron transfer from a deuteron [11] or ^{9}Be target [11, 12], both having low neutron separation energy, has been induced and the neutron has undergone a final state interaction with the projectile of, for example ^{9}Li. In this way the ^{10}Li resonances have been populated in what can be defined a "transfer to the continuum reaction" [21]-[26]. Thus the neutron-core interaction could be determined in a way which is somehow close to the determination of the optical potential from the elastic scattering of normal nuclei.

In both the transfer Fig. 4 or the projectile fragmentation, Fig. 5 methods the neutron-core interaction that one is trying to determine appears in the reaction as a "final state" interaction and therefore reliable information on its form and on the values of its parameters can be extracted only if the primary reaction is perfectly under control from the point of view of the reaction theory. This has been possible thanks to very accurate and systematic studies of transfer to the continuum reactions in normally bound nuclei [28],[29]-[34].

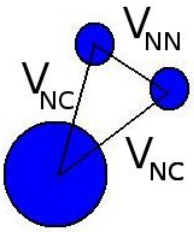

Figure 3: Two interactions in the three-body system: V_{NC}: neutron-core potential, V_{NN}: neutron-neutron potential.

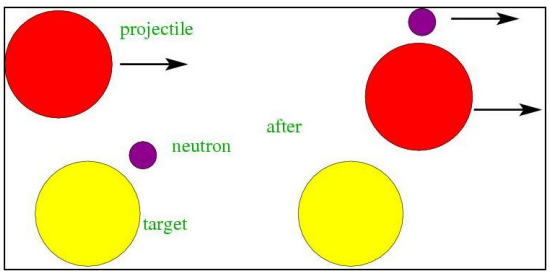

Figure 4: Schema of transfer reaction.

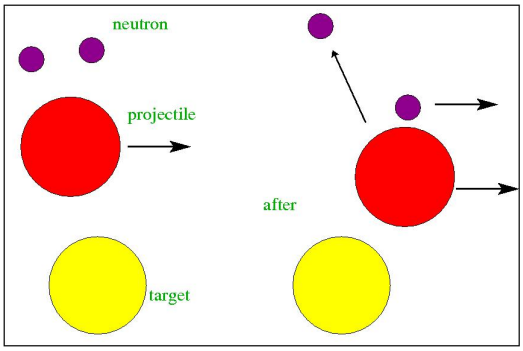

Figure 5: Schema of fragmentation reaction.

This thesis contains therefore four main parts. In a first part, we study transfer to the the continuum reaction. We argue and show that among the several methods discussed above to perform spectroscopy in the continuum, the neutron transfer method looks very promising since

the reaction theory exists and has been already tested in many cases [21]-[27]. This has been possible thanks to very accurate and systematic studies of transfer to the continuum reactions in normally bound nuclei [28],[29]-[34]. We show that the theory of transfer reactions from bound to continuum states is well suited to extract structure information from data obtained by performing “spectroscopy in the continuum". The low energy unbound states of nuclei such as ^{10}Li and ^{5}He can be analyzed and the neutron-core interaction, necessary to describe the corresponding borromean nuclei ^{11}Li and ^{6}He can be determined in a semi-phenomenological way. An application to the study of ^{10}Li is then discussed and it is shown that the scattering length for *s*-states at threshold can be obtained from the ratio of experimental and theoretical cross sections. The scattering single particle states of the system n+^{9}Li are obtained in a potential model. The corresponding S-matrix is used to calculate the transfer cross section as a function of the neutron continuum energy with respect to ^{9}Li. Three different reactions are calculated ^{9}Li(d,p)^{10}Li, ^{9}Li(^{9}Be,^{8}Be)^{10}Li, ^{9}Li(^{13}C,^{12}C)^{10}Li, to check the sensitivity of the results to the target used and in particular to the transfer matching conditions. Thus the sensitivity of the structure information extracted from experimental data on the reaction mechanism is assessed.

In the next chapter, we present a simple time dependent model for the excitation of a nucleon from a bound state to a continuum resonant state in a neutron-core complex potential which acts as a final state interaction. The final state is described by an optical model S-matrix so that both resonant and non-resonant states of any continuum energy can be studied as well as deeply bound initial states. It is shown that, due to the coupling between the initial and final states, the neutron-core free particle phase shifts are modified, in the exit channel, by an additional phase. The effect of the additional phase on the breakup spectra is clarified. As an example the population of the low energy resonances of ^{11}Be and of the unbound ^{13}Be is discussed. Finally, we suggest that the excitation energy spectra of an unbound nucleus might reflect the structure of the parent nucleus from whose fragmentation they are obtained.

In the third chapter, we are interested in the nuclear structure of halo nuclei. We use the particle-particle Random Phase Approximation (RPA) to study a range of Beryllium isotopes from ^{8}Be to the neutron-halo nucleus ^{14}Be. First we do a quick review of the RPA formalism in order to show the main specificities of the calculation and to define the notations. Then we present the derivation of the one- and two-body densities of the valence neutrons of halo nuclei in the particle-particle RPA formalism. These densities are useful to calculate several observable as rms, transition rates or average distance between the neutrons of the halo. Results obtained with our method are compared with available experimental data with success.

In order to explore ever-more exotic regions of the nuclear chart, towards the limits of stability of nuclei, European physicists have built several large-scale facilities in various countries of the European Union. Today they are collaborating in planning a new radioactive ion beam (RIB) facility which will permit to investigate hitherto unreachable parts of the nuclear chart. In the fourth part, we shall look at some coupled-channels calculation related to experiments faisible at the forthcoming facility EURISOL. This work is really preliminary. First we present

a series of tools to study transfer reaction within the coupled-channels formalism. These tools have not been developed by us as the previous ones (fragmentation and transfer reaction). They are basically used to extract spectroscopic factors. Then we proceed to some test of sensitivity of the optical potential in order to see what can be expected from the comparison of theoretical models and experimental results.

The conclusions and prospects of this work are given in the final section.

The first two chapters of this thesis have been already published in three articles: [35], [36] and [37].

Chapter 1

Transfer to the continuum

1.1 Introduction

We apply the transfer to the continuum method, very well understood for normally bound nuclei [28], to light unbound nuclei which recently have attracted much attention [9]-[12] in connection with exotic and halo nuclei. Halo nuclei are very complicated systems to describe. In particular the accuracy of reaction theories used to extract structure information is a key issue. From the structure point of view, simple semi-phenomenological models have been proposed which exhibit the properties of those nuclei in terms of one (or two) single nucleon wave functions and which make also easy the calculation of cross sections for various reactions initiated by such projectiles [38]. We will discuss in detail structures models in Chapter 3. One-neutron halo nuclei can be described in a two-body model as a core plus one neutron. All the complexity of the many-body problem, when two-body correlations are important, can be put in an effective one-body potential between the extra neutron and the core, that is the Hartree-Fock potential plus the contribution due to the particle-core vibration couplings. This contribution which is small in normal nuclei is so strong in nuclei such as ^{11}Be or ^{10}Li for example that it might be responsible for an inversion of $1/2^+$ and $1/2^-$ states [39, 40]. It also induces a strong modification of the wave functions which become mixtures of one-single nucleon state and more complicated ones formed of a single nucleon coupled with core vibrations. As a consequence the one-nucleon spectroscopic factors are smaller than one. They in turn can be extracted from one-neutron removal cross sections if one has a good description of the reaction. Then the comparison between theoretical and measured spectroscopic factors constitutes a strong test of the model.

On the other hand, two-neutron halo nuclei such as ^{6}He, ^{11}Li have a two-neutron halo due to the properties of the single extra neutrons which are unbound in the field of the core, the two-neutron pair being weakly bound due to the neutron-neutron pairing force. In a three-body

model those nuclei are described as a core plus two neutrons. The properties of core plus one neutron system are essential and the model relies on the knowledge of angular momentum and parity as well as energies and corresponding neutron-core effective potential, therefore spectroscopic strength for neutron resonances in the field of the core. Again these information can be directly obtained from the analysis of one-neutron breakup or transfer cross sections.
The two borromean nuclei that have been studied more extensively so far are ^{6}He [41], and ^{11}Li [42]-[45]. The two neutron halo is build on a core which in same cases is itself a radioactive nucleus (i.e.^{9}Li which is the core of ^{11}Li). They are "borromean" since the corresponding (A-1) nuclei are unbound. Thus ^{5}He, ^{10}Li, as well as ^{13}Be and ^{16}B exist only as neutron plus core resonance states and it takes an extra neutron and its paring energy to finally bind ^{11}Li and ^{6}He. However the two neutron separation energy is typically very small (ε_{2n}=0.3MeV in ^{11}Li).

1.2 Cross section

A full description of the treatment of the scattering equation for a nucleus which decays by single neutron breakup following its interaction with another nucleus, can be found in Refs. [21, 22, 46]. There it was shown that within the semiclassical approach for the projectile-target relative motion, the cross section differential in ε_f, the final, continuum, neutron energy with respect to the target is

$$\frac{d\sigma}{d\varepsilon_f} = C^2S \int_0^\infty d\mathbf{b_c} \frac{dP_t(b_c)}{d\varepsilon_f} P_{ct}(b_c), \tag{1.1}$$

(see Eq. (2.3) of [26]) and C^2S is the spectroscopic factor for the initial single particle orbital. The core survival probability $P_{ct}(b_c) = |S_{ct}|^2$ [26] in Eq.(1.1) takes into account the peripheral nature of the reaction and naturally excludes the possibility of large overlaps between projectile and target. P_{ct} is defined in terms of a S-matrix function of the core-target distance of closest approach b_c. A simple parameterization is $P_{ct}(b_c) = e^{(-\ln 2 exp[(R_s - b_c)/a])}$, where the strong absorption radius $R_s \approx 1.4(A_p^{1/3} + A_t^{1/3})fm$ is defined as the distance of closest approach for a trajectory that is 50% absorbed from the elastic channel and $a = 0.6fm$ is a diffuseness parameter. The values of R_s thus obtained agree within a few percent with those of the Kox parameterization [64].

1.3 Transfer to the continuum theory

Therefore according to [21] the matrix element in the amplitude for a transition from a nucleon bound state ψ_i in the projectile to a final continuum state ψ_f

$$A_{fi} = \frac{1}{i\hbar}\int_{-\infty}^{\infty} dt < \psi_f(t)|V(\mathbf{r})|\psi_i(t) >, \tag{1.2}$$

can be reduced to an overlap integral between the asymptotic parts of the wave functions for the initial and final state. Here V is the interaction responsible for the neutron transition to the continuum. In the case of a light exotic nucleus interacting with another light nucleus $V(r)$ is just the neutron-target optical potential $V(r) = U(r) + iW(r)$, and the differential probability with respect to the neutron energy can be written as

$$\begin{aligned}
\frac{dP_t(b_c)}{d\varepsilon_f} &= \frac{1}{8\pi^3}\frac{m}{\hbar^2 k_f}\frac{1}{2l_i+1}\Sigma_{m_i}|A_{fi}|^2 \\
&\approx \frac{4\pi}{2k_f^2}\Sigma_{j_f}(|1-\bar{S}_{j_f}|^2 + 1 - |\bar{S}_{j_f}|^2)(2j_f+1)(1+F_{l_f,l_i,j_f,j_i})B_{l_f,l_i} \\
&= \sigma_{nN}(\varepsilon_f)\mathscr{F},
\end{aligned} \tag{1.3}$$

where A_{fi} is given by Eq.(1.2) and we have averaged over the neutron initial states and summed the neutron final states.

Equation (1.3) has a very transparent structure which makes it suitable to describe the kind of reactions we are interested in this chapter. In fact the term

$$\sigma_{nN}(\varepsilon_f) = \frac{4\pi}{2k_f^2}\Sigma_{j_f}(|1-\bar{S}_{j_f}|^2 + 1 - |\bar{S}_{j_f}|^2)(2j_f+1), \tag{1.4}$$

gives the neutron-nucleus free particle cross section. $\bar{S}_{j_f}$ is the neutron-nucleus optical model S-matrix, which is calculated for each nucleon final energy in the continuum with an energy dependent optical model. The two terms $|1-\bar{S}_{j_f}|^2$ and $1-|\bar{S}_{j_f}|^2$ represent the shape elastic scattering and the absorption respectively. For the cases described in this work only the shape elastic term will contribute, since we will discuss scattering states below the first core excited state and therefore we will use a real optical potential.

The term

$$\mathscr{F} = (1+F_{l_f,l_i,j_f,j_i})B_{l_f,l_i}, \tag{1.5}$$

represents what in the theory of final state interactions [47] has been called the enhancement factor. F_{l_f,l_i,j_f,j_i} is an l to j coupling factor between the angular momenta of the neutron in the initial and final states. It is also energy dependent and reflects the spin matching conditions well known for transfer between bound states [48]-[51]. The term

$$B_{l_f,l_i} = \frac{1}{4\pi}\left[\frac{k_f}{mv^2}\right]|C_i|^2\frac{e^{-2\eta b_c}}{2\eta b_c}M_{l_f l_i}, \tag{1.6}$$

contains the matching conditions between the initial and final neutron energies and the relative motion energy per particle $\frac{mv^2}{2}$ at the distance of closest approach. $\eta = \sqrt{k_1^2+\gamma_i^2}$ is the transverse component of the neutron momentum which is conserved in the neutron transition, $\gamma_i = \frac{\sqrt{-2m\varepsilon_i}}{\hbar}$ and $k_f = \frac{\sqrt{2m\varepsilon_f}}{\hbar}$ are the neutron momenta in the initial and final states and $k_1 = \frac{\varepsilon_f-\varepsilon_i-mv^2/2}{\hbar v}$ is the parallel component of the neutron momentum in the initial state. Also b_c is the core-target impact parameter, C_i is the initial state asymptotic normalization constant and $M_{l_f l_i}$ is a factor depending on the angular parts of the initial and final wave functions [23, 26].

An important characteristic of the present formalism is that the transfer probability Eq.(1.3) contains the factor $1/k_f^2$ which corresponds to the inverse of the neutron entrance channel flux. It was noticed in Ref.[52] that if a transfer to the continuum formalism does not contain such factor then the model cross sections will always vanish at zero energy, which is unphysical. Our calculated cross section instead will have in the case of a virtual state of exactly zero energy and $l = 0$ a divergent-like behavior at zero energy, in accordance to experimental data and to the physical expectations for a s-state at threshold. It should be also noticed that in the term B_{l_f,l_i} there is a modulating factor $\frac{k_f}{mv^2} \approx \frac{v_f}{v^2}$ which takes into account the matching between the projectile velocity at the distance of closest approach v and the neutron final velocity in the continuum v_f.

An interesting case is when the final continuum energy approaches zero. Then only the $l = 0$ partial wave contributes and using $\frac{1}{4}|1-\bar{S}_0|^2 = \sin^2\delta_0$, Eq.(1.1) becomes very simple if it is written as differential in the final neutron momentum, in particular if the neutron initial state is also $l = 0$ and we assume unit spectroscopic factor. In that case the spin coupling factor $(1+F_{l_f,l_i,j_f,j_i})$ and the $M_{l_f l_i}$ factor are independent of energy such that the differential cross section finally reads:

$$\frac{d\sigma}{dk_f} = (\sin\delta_0)^2|C_i|^2\left[\frac{\hbar}{mv}\right]^2\int_0^\infty d\mathbf{b_c}\frac{e^{-2\eta b_c}}{\eta b_c}e^{(-\ln 2 exp[(R_s-b_c)/a])}. \tag{1.7}$$

If the LHS of the previous equation is measured experimentally, then $(\sin\delta_0)^2$ can be obtained by doing the ratio between $d\sigma_{exp}/dk_f$ and the remaining terms in the RHS of Eq.(1.7), in the limit of zero energy. In fact the above equation is well behaved, because the only depen-

dence on the neutron energy is contained in the term $\frac{e^{-2\eta b_c}}{\eta b_c}$, where η goes to a constant in the limit of zero energy. Finally the scattering length can be obtained from $a_s = -\lim_{k\to 0} \frac{tan\delta_0}{k}$. It is interesting to note the similarity between Eq.(1.7) and the corresponding formula of the theory of transfer between bound states

$$\sigma(\varepsilon_f) = \frac{\pi}{2}|C_i C_f|^2 \left[\frac{\hbar}{mv}\right]^2 \int_0^\infty d\mathbf{b_c} \frac{e^{-2\eta b_c}}{\eta b_c} e^{(-\ln 2 exp[(R_s - b_c)/a])}, \tag{1.8}$$

as discussed in [21] where it was shown that the term $(\sin\delta_0)^2$ after integrating over the final continuum energy, plays the same role as the asymptotic normalization constant of the final bound state C_f^2.

1.4 Application to ^{10}Li structure

Since the link between reaction theory and structure model is made by the optical potential determining the S-matrix in Eq.(1.3), once that the theory has fitted position and shape of the continuum n-nucleus energy distribution, what can be deduced are the parameters of a model potential. Therefore we are now going to use such a model to describe the properties of ^{10}Li. ^{10}Li is unbound and in its low energy continuum four states (two spin doublets) are expected to be present due to the coupling with the $3/2^-$ p-state of the extra proton in the ^{9}Li core. The states with a total spin of 1^- or 2^- would be due to the coupling with a neutron in a s-state, while coupling with the p-state would give 1^+ or 2^+. There is already a rich literature on the subject both from the experimental [11] as well as from the theoretical point of view [42]-[43]. In particular the best evidences are in favor of ^{10}Li having a 1^- ground state due to an s-virtual state close to the threshold. Recently a proton pickup experiment d(^{11}Be,^{3}He)^{10}Li [9] has definitely confirmed the earlier hypothesis that the ground state of ^{10}Li is the 2s virtual state and that the $1p_{1/2}$ orbit gives an excited state.

Table 1.1: Woods-Saxon and spin-orbit potential parameters.

V_0 (MeV)	r_0 (fm)	a (fm)	V_{so} (MeV)	a_{so} (fm)
-39.83	1.27	0.75	7.07	0.75

To describe the valence neutron in ^{10}Li we assume that the single neutron Hamiltonian with respect to ^{9}Li has the form

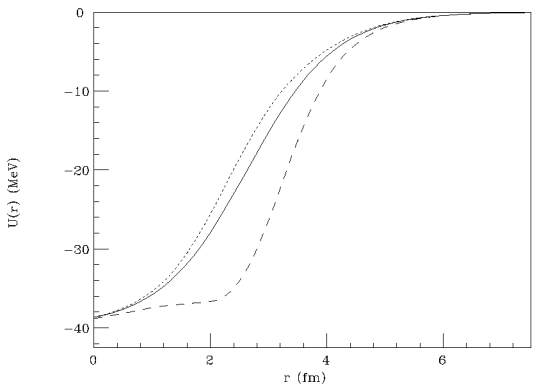

Figure 1.1: Woods-Saxon potential (solid line) and Woods-Saxon plus surface correction according to Eq.(1.10) for the l=0 state (long dashed line) and the l=1 state (short dashed line).

$$h = t + U, \tag{1.9}$$

where t is the kinetic energy and

$$U(r) = V_{WS} + \delta V \tag{1.10}$$

is the real part of the neutron-core interaction. V_{WS} is the usual Woods-Saxon potential plus spin-orbit

$$V_{WS}(r) = \frac{V_0}{1+e^{(r-R)/a}} - \left(\frac{\hbar}{m_\pi c}\right)^2 \frac{V_{so}}{ar}\frac{e^{(r-R)/a}}{(1+e^{(r-R)/a})^2}\mathbf{l}\cdot\sigma, \tag{1.11}$$

and δV is a correction which originates from particle-vibration couplings. They are important for low energy states but can be neglected at higher energies. If Bohr and Mottelson collective model is used for the transition amplitudes between zero and one phonon states, calculation of such couplings suggest the following form [53]:

$$\delta V(r) = 16\alpha e^{2(r-R)/a}/(1+e^{(r-R)/a})^4 \tag{1.12}$$

where $R \approx r_0 A^{1/3}$. The parameters of V_{WS} for the n-^{9}Li interaction used in this work are those given in Table 1.1 In Table 1.2 we give the scattering lengths and energy obtained for the $2s$ and $1p_{1/2}$ states, with different values of the strength α. Eq.(1.12) will be justified microscopically in Chapter 3.

1.5 Results and discussion

It would be therefore interesting and important if an experiment could determine the energies of the unbound ^{10}Li states such that the interaction parameters could be deduced. Two ^{9}Li(d,p)^{10}Li experiments have recently been performed. One at MSU at 20 A.MeV [11] and the other at the CERN REX-ISOLDE facility at 2 A.MeV [12]. For such transfer to the continuum reactions the theory underlined in Sec. 2 is very accurate. It should be noticed that the theory has usually been applied to projectile breakup reactions, in order to study single particle excitations in the target. Here it will be applied to single neutron target breakup leading to excitations of the n-projectile continuum.

Table 1.2: Scattering length of the s-state, energy and width of unbound p-state and strength parameter for the δV potential.

	ε_{res} (MeV)	Γ (MeV)	a_s (fm)	α (MeV)
$2s_{1/2}$			323	-12.5
			-17.20	-10.0
$1p_{1/2}$	0.595	0.48		3.3

In order to study the sensitivity of the results on the target, and therefore on the spin selection rules for transfer and on the energies assumed for the s and p states, we have calculated the reaction ^{9}Li$(X,X-1)^{10}$Li at 2 A.MeV for three targets d, ^{9}Be, ^{13}C. The ^{13}C target has been chosen because in such a case the neutron transfer from the $p_{1/2}$ initial state to the $p_{1/2}$ final state in ^{10}Li will be a non spin flip transition $j_i = l_i - 1/2 \rightarrow j_f = l_f - 1/2$ while the transfer to the $s_{1/2}$ state would be a spin-flip transition which are enhanced at low incident energy [48]-[51]. ^{14}N would also be a good target, having a valence neutron in a $p_{1/2}$ state, but the absolute cross sections would be smaller as the separation energy is larger (10.55 MeV) than in ^{13}C. It would however provide good matching conditions at higher beam energies ($E_{inc} \approx 10$ A.MeV). For the other two cases, the initial state is a $s_{1/2}$ in the deuteron and a $p_{3/2}$ in ^{9}Be thus in both cases $j_i = l_i + 1/2$. Then the transfer to the 2s state is a non spin-flip transition which is hindered, while the transfer to the $p_{1/2}$ is enhanced at low incident energy. The initial state parameters are given in Table 1.3 For each initial state a unit spectroscopic factor was assumed.

We show in Fig. 1.2 the neutron energy spectrum relative to ^{9}Li obtained with the interaction and single particle energies of Tables 1.1 and 1.2. We define as the resonance energy of the p-state the energy at which $\delta_{j_f} = \pi/2$. This is also the energy at which $|1-\bar{S}_{j_f}|^2$ in Eq.(1.3) gets its maximum value as it can be seen in Fig. 1.3. The results of Fig. 1.2 show that the peak of the cross section for transfer to the p- state will determine without ambiguity the position of the p-state in a target independent way. The measured width instead would depend on the

Table 1.3: Targets and initial state parameters of the bound neutron.

Target	d	^{9}Be	^{13}C
$\varepsilon_i(MeV)$	-2.22	-1.66	-4.95
l_i	0	1	1
j_i	1/2	3/2	1/2
$C_i(fm^{-\frac{1}{2}})$	0.95	0.68	1.88

reaction mechanism, but the "true" resonance width can however be obtained from the phase shift energy variation near resonance, given by the formula [47] $d\delta_{j_f}/d\varepsilon_f|_{\varepsilon_{res}} = 2/\Gamma$, once that the resonance energy is fixed. Using this formula we obtained, in the case of the p-state in ^{10}Li, the value $\Gamma = 0.48MeV$ given in Table 1.2. From Fig. 1.2 one can see that the target dependence would influence the extracted width by about 10-15%. It is important to notice that in the approach of this work the line shape is determined by the energy dependence of the phase shift and S-matrix and eventually it could be influenced by an energy dependence of the potential parameters. Fig. 1.3 shows indeed the energy dependence of $|1-\bar{S}_{j_f}|$ for l=1. Therefore there is no need to introduce any a priori form for the resonance shape and width.

For the s final state we see that there is a larger probability of population in the spin-flip reaction initiated by the carbon target. An important question is whether a measure of the line-shape (or spectral function) and absolute value of the cross section will determine the characteristics of the state, and therefore the interaction, also in this case. We have already shown in Sec. 1.2 that in principle it should be possible. However in order to elucidate better this question we first remind some of the peculiarities of the low energy scattering of neutral particles in the $l = 0$ partial wave [47, 52]. It is well known that because of the absence of the centrifugal barrier the energy and width of an s-state are difficult to define. Therefore we will in the following study the energy dependence of the phase shift in various potentials and determine for each case the values of the scattering length. The potential parameters are those of Table 1.1 and Table 1.4. Fig. 1.4 shows the behavior, as a function of the neutron momentum, of $\frac{tan\delta_0}{k}$ (dotdashed curve) for the potential (2) of Table 1.4, of the cross section (full curve) at the strong absorption radius calculated in the case of a deuteron target and of the factor $\frac{e^{-2\eta b_c}}{\eta b_c}$ (dashed curve) from Eq.(1.7). The latter has a very smooth behavior and therefore it is easy to see that $(\sin\delta_0)^2$ and then $|a_s|$, could be determined from the ratio between the experimental cross section and the remaining part of the RHS of Eq.(1.7).

The sensitivity of the results for transfer to an s-state, on the potential assumed, is illustrated by Figs. 1.5a, 1.5b, 1.5c, 1.5d. In Fig. 1.5a the $l = 0$ phase shift is plotted as a function of the continuum energy. There are several potentials which give a similar behavior of the phase shift but different scattering lengths, (cf. Table 1.4) and in particular a different line shape for

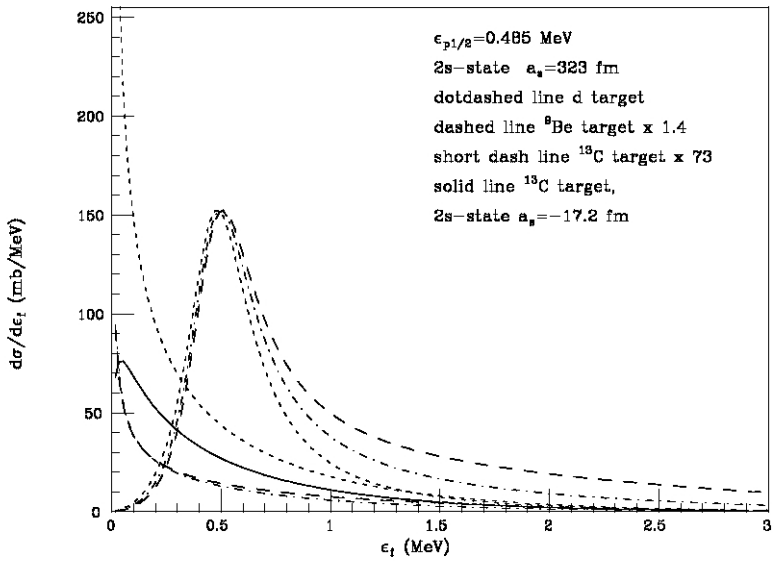

Figure 1.2: Neutron-^{9}Li relative energy spectra for transfer to the *s* and *p* continuum states in ^{10}Li given in Table 1.2 Dotdashed lines are absolute cross sections for transfer from a deuteron target, dashed lines from a ^{9}Be target, and short dashed line from a ^{13}C target. The Be and C cross section have been renormalized to the deuteron cross sections by the factors indicated on the figure. The solid line is the transfer cross section from the C target to the second s-state given in Table 1.2.

the transfer cross section from a deuteron target to an *s*-state, as shown in Figs. 1.5c, 1.5d. The curves from bottom to top in Fig. 1.5a, correspond to calculations in the potentials of Table 1.4 in increasing order of depth. Therefore the dashed and solid lines in Fig. 1.5c correspond to unbound states with negative scattering lengths, while the long dotdashed line corresponds to a virtual state with a large scattering length consistent with infinity and therefore of zero energy. Then the other three, short dashed, dotted and short dashdotted curves, cases (4), (5) and (6) of Table 1.4 respectively, correspond to weakly bound states close to threshold. Our results for the phase shifts and scattering length are consistent with those of the thesis of S. Pita [9] and with the well known theory of low energy scattering of neutral particles in s-wave. We have indeed in Fig. 1.5a that for unbound states the phase shift is zero at zero energy, then increases up to a maximum value and then decreases again. Because it never increases going through the value $\pi/2$ when the energy increases, as instead it might happen for $l > 0$ states, then the states corresponding to cases (1),(2) of Table 1.4 cannot be defined as resonances, even though they give rise to an enhancement of the cross section (see Ref.[47], Eq.(4.235) and following discussion). Furthermore they do not give rise to singularities in the scattering amplitude on the

Table 1.4: Strengths of the *s*-state potential in Eq.(1.10) and corresponding scattering lengths. Labels in the first column identify the corresponding curves in Fig. 1.5.

	V_0 (MeV)	α (MeV)	a_s (fm)
(1)	-39.83	-4.0	-2.4
(2)	–	-10.0	-17.2
(3)	–	-12.2	-318
(4)	–	-13.5	45.1
(5)	–	-15.0	21.4
(6)	-42.80	-13.3	12.9

physical sheet of the complex energy plane. For each of them instead, the scattering amplitude has a pole at negative energy $\varepsilon_f = -|\varepsilon_{(1,2)}|$ on the un-physical sheet. These poles represent bound states close to threshold which give the same free particle scattering cross section as the unbound states, namely $\sigma = 4\pi/(k_f^2 + \kappa^2)$ where $\kappa^2 = 2m|\varepsilon|/\hbar^2$ (see Ref.[**?**], Eq. (133.8) and following discussion). Therefore cases (1),(2) are broad states with a width of 1-2MeV. In case (3) instead the phase shift value is very close to $\pi/2$ at zero energy corresponding to a virtual state. In fact the S-matrix gets its maximum value of $|1-\bar{S}| = 2$ in Fig. 1.5b. Cases (4), (5) and (6) are from potentials which barely bind states very close to threshold. The phase shift approaches the value π at zero energy and the cross sections shown in Fig. 1.5d are a typical example of how weakly bound states can affect scattering at low energy.

On the other hand, what is clear is that because of the sharp rise towards zero of the factor $1/k_f$ and of the less fast decreasing of the $|1-\bar{S}|^2$ term of Eq.(1.3) for $l = 0$, shown in Fig. 1.5b, the peak of the *s*-state transfer cross section would always be “downshifted" with respect to the maximum of $|1-\bar{S}|$, furthermore a maximum for this term always exists irrespective of the fact that the *s*-state at threshold is bound or unbound. The absolute value of the corresponding transfer cross sections in Fig. 1.5c, 1.5d increases and has the typical divergent-like behavior in correspondence to cases (3) and (4) of Table 1.4. Then for the more bound states (dotted and dotdashed line), the transfer cross section decreases again. One such state is obtained decreasing both the depth of the Woods-Saxon and of the surface term and it corresponds to the smallest positive scattering length in Table 1.4 ($a_s = 12.9 fm$). The cross section that one would measure in the continuum, shown in Fig. 1.5d is just a reflection of the fact that the wave function for a weakly bound s-state has a long tail and thus some of the transfer strength is in the continuum. In fact, in the region over which the matrix element in Eq.(1.2) is different from zero, the behavior of bound and unbound state wave functions with energies very close to threshold, is almost the same, due to the very large wave length.

Therefore although it would seem quite hard to search experimentally for the energy and “nature" of weakly bound or just unbound s-states in exotic nuclei we hope to have shown that

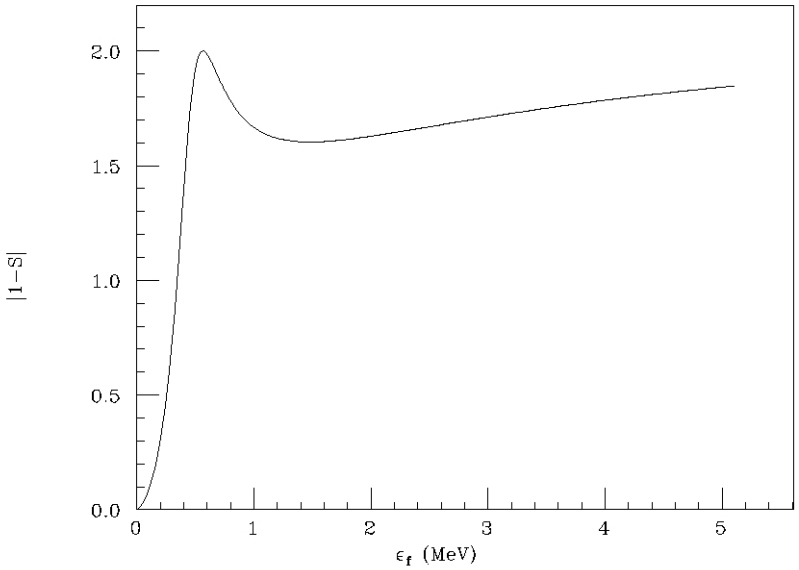

Figure 1.3: Energy dependence of $|1-\bar{S}|$ for l=1.

the absolute value of the cross section right at threshold together with the line shape should determine the scattering length of the state. It appears that in the case of ^{10}Li states with scattering lengths larger than $|a_s| \sim 20fm$ would all lead to a divergent-like behavior of $\sigma(\varepsilon_f)$ when $\varepsilon_f \to 0$. The absolute value of a_s can be determined from the experimental spectrum as discussed in relation to Eq.(1.7) and then the parameters of the n-^{9}Li interaction will be fixed as well. Those are the so called virtual states. One should also be aware that, as shown in Fig. 1.5d, resonant-like structures seen in the low energy continuum could be an indication of weakly bound *s*-states as well as of unbound *s*-states. In order to disentangle these two situations one would obviously need complementary measurements. If the *s*-state is expected to be the ground state, then the mass measurement of the nucleus will determine whether it is bound or unbound. In the specific case of ^{10}Li we know indeed that it is unbound. In other cases one could use different targets and/or different incident energies to study the variation of the maximum of the structures and thus deduce the energy of the final state from the matching conditions with the initial state.

Finally as the neutron scattering will happen in all partial waves, if there is an unbound or virtual *s*-state the corresponding cross section would seat on top of a background due to scattering on all partial waves, as one goes away from threshold. The behavior of such a background would be different for different potentials and therefore a whole calculation with all relevant

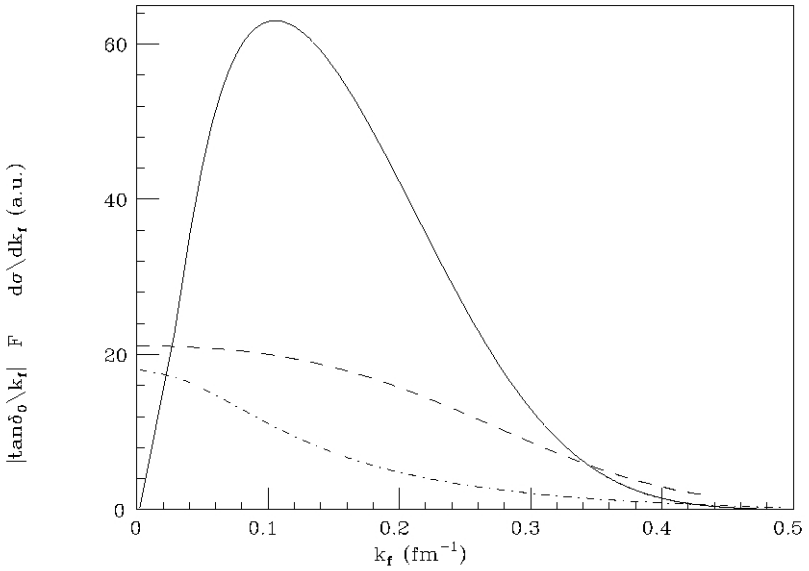

Figure 1.4: $\frac{tan\delta_0}{k}$ (dotdashed curve) from phase shift for case (2) of Table 1.4, factor $F = \frac{e^{-2\eta b_c}}{\eta b_c}$ (dashed curve) at $b_c = R_s$ from Eq.(1.7) and cross section (full curve) for a deuteron target.

partial waves, as contained in our formula Eq.(1.3) and a comparison with good resolution data, should help extracting the correct n-core interaction. On the other hand it is important to stress that in the case discussed in this work there is no spreading width of the single particle states since the n-^{9}Li interaction is real at such low energies. In fact the first excited state of ^{9}Li is at $E^* = 2.7MeV$. For “normal" nuclei instead the single particle resonances appear at higher excitation energies (approximately 4-6MeV), and for higher l-values (l=6-10). Then it was shown in Ref. [25] that the spreading width is much larger than the escape width due to the influence of the imaginary part of the potential.

Finally we conclude that if a transfer to the continuum experiment could measure with sufficient accuracy (energy resolution) the line-shapes or energy distribution functions for the s and p-states in ^{10}Li our theory would be able to fix accurately the energy of the p-state and the scattering length of the s-state. Those in turn could be used to test microscopic models of the n-^{9}Li interaction. The integral of the energy distribution will determine the total spectroscopic strength of the state. From our results it appears that such an integral would depend on the neutron initial state in the target in a way which is however perfectly under control in the theory, since it is all contained in the B-term given by Eq.(1.6). Thus the spectroscopic strength of the state would be determined by the comparison between measured and calculated values of the

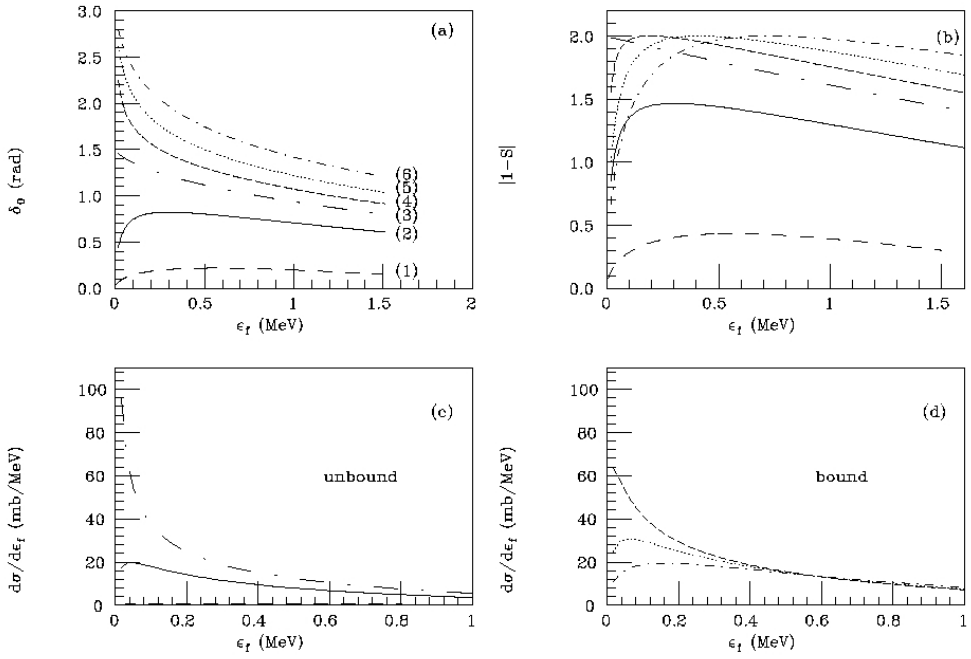

Figure 1.5: Phase shift (a), shape elastic factor $|1 - \bar{S}|$ (b) and cross section (c,d) as a function of the neutron continuum energy for an *s*-state and a deuteron target. Figure (c) contains the results for unbound states with negative scattering length, while figure (d) for bound states with positive scattering length. Labels on the curves identify the corresponding potentials in Table 1.4.

whole energy distribution.

1.6 Conclusions

In this first chapter, we have argued that, apart from the experimental difficulties, the transfer to the continuum method is well suited to study unbound systems such as ^{10}Li which are the building blocks of borromean nuclei. There is a very well tested theory to study such reactions, which allows to determine energy distributions for population of unbound states in absolute value. Provided the same information is available from the experimental point of view, the theory would allow the determination of the scattering length of *s*-states and the ”resonance" energy of unbound single particle states, the associated l and j and the total strength. Those studies would eventually be used to determine the neutron-core interaction.

The advantage of our method is that the basic ingredient of the theory is the S-matrix describing the neutron-nucleus scattering. It can be calculated with an energy dependent potential which can incorporate consistently certain peculiarities of unbound nuclei such as ^{10}Li, whose continuum energy 0-0.5MeV range, for example, contains at least two states with l=0,1 obtainable only with two very different potential wells.

Furthermore the spin-orbit interaction can also be included so that at any energy the contribution from all states with given l and j can be obtained. This is very useful because not only the excitation of states of fixed angular momentum can be studied, but also the background due to the presence of all other possible angular momentum states can be calculated and in this way the strength of just one single particle state can be obtained unambiguously from data which would contain the contribution from all angular momenta. The theory has the correct behavior when the continuum energy approaches threshold such that the contribution from virtual states can be distinguished from that from weakly bound or unbound states.

We have calculated neutron transition probabilities for going from an initial bound state in a nucleus to a scattering state including final state interaction with another nucleus. Our way of describing the final state interaction in the continuum is through an optical model S-matrix. A similar approach described in the next chapter, can be applied to the treatment of inelastic projectile excitations in which, following its interaction with the target, a neutron goes from a bound to an unbound state with final state interaction in the same nucleus. This is the process which creates ^{10}Li in the final state in the projectile-breakup-type of experiments [8]. By using such a procedure a very accurate theory of two neutron breakup could be obtained, incorporating properly the two step mechanism implicit in the formation of a neutron-core resonance state in reactions like $^{11}\mathrm{Li} + \mathrm{X} \rightarrow ^{10}\mathrm{Li}^* + \mathrm{n} \rightarrow ^{9}$Li+2n [10].

In fact ^{11}Li breakup and other 2n breakup reactions have often been treated as a process in which the two neutrons are emitted simultaneously in a single breakup process, which corresponds to that assumption of two highly correlated neutrons. This in principle could be improved by considering the second neutron which decays in flight from a resonant state, as seen for ^{6}He, by a breakup form factor different than that of the first neutron and by taking into account explicitly the sequential nature of the process.

Chapter 2

Projectile fragmentation

2.1 Introduction

In this second chapter, we will call projectile fragmentation the elastic breakup (diffraction reaction) of neutron halo nuclei, when the observable studied is the neutron-core relative energy spectrum. This kind of observable has been widely measured in relation to the Coulomb breakup on heavy target. The reaction mechanisms are very different when Coulomb or short-range interactions dominate. For nuclear halos the Coulomb dominates for heavy targets and is quite insignificant for light targets. For medium-heavy targets, short- and long-range contributions may be comparable and interference phenomena occur.Recently results on light targets have also been presented [54]. These data enlighten the effect of the neutron final state interaction with the core of origin, while observables like the core energy or momentum distributions enlighten the effect of the neutron final state interaction with the target.

Projectile fragmentation has been used experimentally also with two neutron halo projectiles. In this case it has been suggested that the reaction might proceed in one step (simultaneous emission of the two neutrons) or two steps (successive emissions) depending on whether the target is heavy and therefore Coulomb breakup (core recoil) is the dominant mechanism or the target is light and then nuclear breakup is the dominant mechanism [55]. The successive emission can be due to different mechanisms. One possibility is that one neutron is ejected because of the interaction with the target, as in the one- neutron fragmentation case, while the other is left behind, for example in a resonance state, which then decays. This second step has been described by the sudden approximation in Ref.[45] under the hypothesis that the first neutron is stripped and that the transparent limit for the second neutron applies. It corresponds to consider the second neutron emitted at large impact parameters such that the neutron-target interaction can be neglected. The two-step mechanism implies that the two neutrons are not

strongly correlated such that the emission can be considered sequential.

However the neutron-target interaction gives rise not only to stripping but also to elastic breakup and in both cases to first order in the interaction the neutron ends-up in a plane wave final state [22]. It can then re-interact with the core which, for example, is going to be ^{10}Be in the case of the one-neutron halo projectile ^{11}Be, while it will be ^{12}Be in the case of the projectile fragmentation of ^{14}Be, since ^{13}Be is not bound. While in the case of ^{11}Be the structure of both its bound and continuum states is well known from other kinds of experiments and therefore projectile fragmentation experiments are useful to enlighten the reaction mechanism and its possible description, in the case of ^{13}Be or of other unbound nuclei the interplay between structure and reaction aspects is still to be clarified.

Experiments with a ^{14}B projectile [10, 56] have also been performed, in which the n-^{12}Be relative energy spectra have been reconstructed by coincidence measurements. In such a nucleus the valence neutron is weakly bound, with separation energy S_n=0.969 MeV, while the valence proton is strongly bound with separation energy S_p=17.3 MeV. Thus the neutron will probably be emitted in the first step and then re-scattered by the core minus one proton nucleus. The projectile-target distances at which this kind of mechanism would be relevant are probably not so large to neglect the effect of the neutron-target interaction. One might wonder therefore on how to describe a neutron which breaks up because of the interaction with the target, is left in a plane wave moving with the same velocity of its original core and re-interacts with it in the final state. This mechanism could be at the origin of the coincidence measurements for a one-neutron halo system like ^{11}Be or for a projectile like ^{14}B. It could be also one of the mechanisms giving rise to ^{13}Be in fragmentation measurements of ^{14}Be. Supposing the two neutrons strongly correlated and being emitted simultaneously due to the interaction with the target, the coincidence measurement of one neutron with the core would evidence the neutron-core final state interaction.

Light unbound nuclei have attracted much attention [35]-[12] in connection with exotic halo nuclei. Besides, a precise understanding of unbound nuclei is essential to determine the position of the driplines in the nuclear mass chart. In two-neutron halo nuclei such as ^{6}He, ^{11}Li, ^{14}Be, the two neutron pair is bound, although weakly, due to the neutron- neutron pairing force, while each single extra neutron is unbound in the field of the core. In a three-body model these nuclei are described as a core plus two neutrons. The properties of core plus one neutron system are essential and structure models rely on the knowledge of angular momentum and parity as well as energies and corresponding neutron-core effective potential, therefore spectroscopic strength for neutron resonances in the field of the core. Ideally one would like to study the neutron elastic scattering at very low energies on the ”core" nuclei. This is however not feasible at the moment as many such cores, like ^{9}Li, ^{12}Be or ^{15}B are themselves unstable and therefore they cannot be used as targets. Other indirect methods instead have been used so far, mainly aiming at the determination of the energy and angular momentum of the continuum states.

Unbound nuclei have been created in several different ways besides the projectile fragmentation [55, 10, 56, 57]-[41] mentioned above: multiparticle transfer reactions [58]-[61] or just one proton [9, 18] stripping.In a few other cases the neutron transfer from a deuteron [60]-[12] has been induced and the neutron has undergone a final state interaction with the projectile of, for example ^{12}Be. In this way the ^{13}Be resonances have been populated in what we have called in the previous chapter a “transfer to the continuum reaction" [21]-[26]. Thus the neutron-core interaction could be determined in a way which is somehow close in spirit to the determination of the optical potential from the elastic scattering on normal nuclei. In both the projectile fragmentation or the transfer method the neutron-core interaction that one is trying to determine appears in the reaction as a "final state" interaction and therefore reliable information on its form and on the values of its parameters can be extracted only if the primary reaction is well under control from the point of view of the reaction theory.

In the previous chapter, we showed that among the methods discussed above to perform spectroscopy in the continuum, the neutron transfer method looks very promising since the reaction theory exists and it has been already tested in many cases [35], [21]-[26]. It is important to remember that the final state interaction of the neutron with the target (or with the projectile, in the case of inverse kinematics reactions) is dominant in the transfer to the continuum method.

In this chapter and in particular in Sec. 2.2 the basic formalism to describe projectile fragmentation, an inelastic-like excitation to the neutron-core continuum [62], is presented and the effect of final state interaction of the neutron with the projectile core is studied. The model is a theory which would then be relevant to the interpretation of neutron-core coincidence measurements in nuclear elastic breakup reactions. In the present work we apply it to the breakup of the halo nuclei ^{11}Be, ^{14}B but also ^{14}Be on light ^{12}C target. In the case of two nucleon breakup we try to describe here only the step in which a neutron is knocked out from the projectile by the neutron-target interaction to first order and then re-interacts in the final state with the core. The case in which a resonance is populated by a sudden process while the other neutron is stripped has been already discussed in Ref.[45] and we will show that there is a simple link with the model presented here. We assume that the neutron which is not detected has been stripped while the other suffers an elastic scattering on the target. But while in Ref.[45] the so-called transparent limit was used for the second neutron, corresponding to no interaction at all between the neutron and the target, we will consider here explicitly the effect of such an interaction on the n-core relative energy spectrum. This will result into a core-target impact parameter dependence for the fragmentation form factor. However, in most of our calculations, we shall also use the no-recoil approximation for the core (cf. Fig. 2.1). On the other hand the influence of a possible second nucleon, when appropriate, is taken into account only by a modification of the neutron-core interaction in the final state. A simple idea for relating the present work to its future development into a two nucleon breakup model is presented in Sec. 2.3. Sec. 2.4 contains the results of our numerical calculations for ^{11}Be which, being already well understood, has been used here as a test case. It also summarizes experimental results and

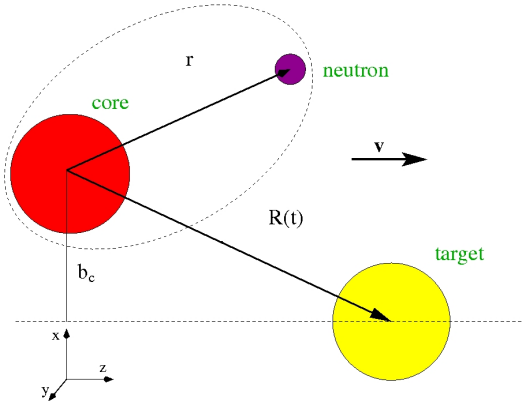

Figure 2.1: Coordinate system used in the calculations

the present theoretical understanding of ^{13}Be. Furthermore details on our assumptions for the potentials needed in the calculations are presented. Numerical results for ^{13}Be are contained in Sec. 2.5. Finally our conclusions are contained in Sec. 2.6.

2.2 Inelastic excitation to the continuum

To first order the inelastic-like excitations can be described by the time dependent perturbation amplitude [22, 62]:

$$A_{fi} = \frac{1}{i\hbar}\int_{-\infty}^{\infty} dt \langle \psi_f(\mathbf{r},t)|V_2(\mathbf{r}-\mathbf{R}(t))|\psi_i(\mathbf{r},t)\rangle, \tag{2.1}$$

for a transition from a nucleon bound state ψ_i to a final state ψ_f which can be a bound state or a continuum state. In this work we shall treat only continuum final states. V_2 is the interaction responsible for the neutron transition (cf. Eq.(2.15) of [22]). Let $\psi_i(\mathbf{r},t) = \phi_i(\mathbf{r})e^{-\frac{i}{\hbar}\varepsilon_i t}$ be the single particle initial state wave function. Its radial part $\phi_i(\mathbf{r})$ is calculated in a potential $V_{WS}(r)$ (cf. Sec. 2.4) which is fixed in space. The coordinate system used in the calculations is shown in Fig.2.1 and it corresponds to the no-recoil approximation for the core. In the case of the very weakly bound ^{11}Be we will drop this approximation and explicitly take into account core recoil by defining **R**(t) as the projectile-target relative motion coordinate. In the special case of exotic nuclei the traditional approach to inelastic excitations needs to be modified. For example the final state can be eigenstate of a potential V_1 modified with respect to V_{WS} because some other particle is emitted during the reaction process as discussed in the introduction. The final state interaction might also have an imaginary part which would take into account the coupling between a continuum state and an excited core. The potential $V_2(\mathbf{r}-\mathbf{R}(t))$ moves past on a

constant velocity path with velocity v in the z-direction with an impact parameter b_c in the x-direction in the plane $y = 0$. These assumption and the other discussed in Sec. 2.4 make our semiclassical model valid at beam energies well above the Coulomb barrier. This is in fact the regime in which projectile fragmentation experiments are usually performed (cf. Sec. 2.4).

The first order time dependent perturbation amplitude then reads

$$A_{fi} = \frac{1}{i\hbar}\int_{-\infty}^{\infty} dt dx dy dz\ \phi_f^*(x,y,z)\phi_i(x,y,z)e^{i\omega t}V_2(x-b_c,y,z-vt), \tag{2.2}$$

where $\hbar\omega$ is the energy difference between the initial and final states. Now change variables and put $z - vt = z'$ or $t = (z - z')/v$. The excitation amplitude becomes

$$A_{fi} = \frac{1}{i\hbar v}\int_{-\infty}^{\infty} dx dy dz dz'\ \phi_f^*(x,y,z)\phi_i(x,y,z)e^{iq(z-z')}V_2(x-b_c,y,z'), \tag{2.3}$$

where

$$q = \frac{\varepsilon_f - \varepsilon_i}{\hbar v}. \tag{2.4}$$

Then

$$A_{fi} = \frac{1}{i\hbar v}\int_{-\infty}^{\infty} dx dy dz\ \phi_f^*(x,y,z)\phi_i(x,y,z)e^{iqz}\tilde{V}_2(x-b_c,y,q), \tag{2.5}$$

where

$$\tilde{V}_2(x-b_c,y,q) = \int_{-\infty}^{\infty} dz V_2(x-b_c,y,z)e^{iqz}. \tag{2.6}$$

In our approach the presence of the target represented by this interaction has the effect of perturbing the initial bound state wave function and allow the transition to the continuum by transferring some momentum to the neutron. For this purpose, although the potential $V_2(r)$ has a radius of the order of the potential of the target, it is enough to choose a simplified form of the interaction. Therefore we choose $V_2(r)$ to be a delta-function potential $V_2(r) = v_2\delta(x)\delta(y)\delta(z)$, with $v_2 \equiv$ [MeV fm^3]. Then the integrals over x and y can be calculated giving

$$A_{fi} = \frac{v_2}{i\hbar v}\int_{-\infty}^{\infty} dz\ \phi_f^*(b_c,0,z)\phi_i(b_c,0,z)e^{iqz}. \tag{2.7}$$

The value of the strength v_2 used in the calculation is discussed in Sec. 2.5 and in Appendix A. From the above equation it is clear what the effect of the n-target δ-interaction is in a time

dependent approach: while in the sudden approach the initial and final state overlap is taken in the whole coordinate space, irrespective of the target and of the beam velocity, here the overlap of the initial and final wave functions is taken at the core- target impact parameter distance on the x-direction which is along the distance of closest approach. The y component is zero (neutron emitted on the reaction plane preferentially) and the z-component, being along the relative velocity axis is boosted by a momentum q.

The delta-function potential should be a good approximation if $\gamma R_T << 1$ and $kR_T << 1$ where R_T is the radius of the target, $\gamma = \sqrt{-2m\varepsilon_i}/\hbar$ is the decay length of the initial single particle wave function corresponding to the nucleon binding energy ε_i and $k = \sqrt{2m\varepsilon_f}/\hbar$ is the nucleon final momentum in the continuum state. In this case the initial and final wave functions are rather constant over the volume of the target and can be replaced by their values at the center. The second condition is related to the first because the cross section becomes small if k is large compared to γ (see Sec. 2.3). We also require that the reaction should be peripheral in the sense that $R_c + R_T < b_c$ where R_c is the projectile core radius. The first condition $\gamma R_T << 1$ means that the projectile should be a good halo nucleus. Another situation where the delta-function potential is a good approximation is when $\gamma R_T >> 1$. That is the initial state should be strongly bound and the initial state wave function decays rapidly inside the target. Then the δ-potential should be located at the surface of the target. If, for example, $V_2(r)$ is a square well potential with radius R_T and if $\gamma R_T >> 1$, then Eq.(2.7) can still be used to estimate the breakup with the following changes:

- b_c is replaced by $b_c - R_T$ i.e. the interaction is located at the surface of the target.
- v_2 is replaced by $\bar{v}_2$ where

$$\bar{v}_2 = \frac{3}{2}\frac{v_2}{(\gamma - ik)^2 R_T^2}. \tag{2.8}$$

Thus the strength is reduced and there is an extra phase. The derivation of Eq.(2.8) is presented in Appendix A.

First we study the simple case where the initial bound state and the final continuum state have $l_i = l_f = 0$, then

$$\phi_i(b_c, 0, z) = -\frac{C_i}{\sqrt{4\pi}}\frac{e^{-\gamma r}}{r}, \tag{2.9}$$

$$\phi_f(b_c, 0, z) = \frac{C_f}{\sqrt{4\pi}} i\frac{k}{2}(h_0^{(-)}(kr) - S h_0^{(+)}(kr)). \tag{2.10}$$

These expressions are the asymptotic forms of the initial and final state wave functions. Their use can be justified when the impact parameter is sufficiently large [45] and $r = \sqrt{b_c^2 + z^2}$.

$$\gamma = \frac{\sqrt{-2m\varepsilon_i}}{\hbar} \quad \text{and} \quad k = \frac{\sqrt{2m\varepsilon_f}}{\hbar}$$

are the neutron momenta in the initial and final states. C_i is the asymptotic normalization constant of the initial state wave function while $C_f = \sqrt{2/L}$ is the normalization constant for the final state. L is a large box radius used to normalize the continuum wave function (cf. Eq.(2.5) of Ref. [21]). The quantity S is the S-matrix representing the final state interaction of the neutron with the projectile core. Then

$$A_{fi} = -\frac{v_2}{\hbar v}\frac{C_i C_f}{8\pi}\int_{-\infty}^{\infty} dz\, \frac{e^{-(\gamma - ik)r} - S^* e^{-(\gamma + ik)r}}{r^2}\cos qz. \tag{2.11}$$

Let us define

$$I_R = Re\int_{-\infty}^{\infty} dz\, \frac{e^{-(\gamma - ik)r}}{r^2}\cos qz, \tag{2.12}$$

and

$$I_I = Im\int_{-\infty}^{\infty} dz\, \frac{e^{-(\gamma - ik)r}}{r^2}\cos qz, \tag{2.13}$$

such that:

$$I(k,q) = I_R + iI_I = |I|e^{iv} \tag{2.14}$$

while

$$\bar{S} = Se^{2iv} = e^{2i(\delta + v)} \tag{2.15}$$

then

$$A_{fi} = C(I - S^* I^*) \tag{2.16}$$

and

$$|A_{fi}|^2 = C^2|I|^2|1 - \bar{S}|^2. \tag{2.17}$$

Where now $C = -\frac{v_2}{\hbar v}\frac{C_i C_f}{8\pi}$.

2.2.1 Wave functions for general l

In the general case of a $l_i > 0$ initial state the amplitude Eq.(2.1) has to be calculated numerically using, for example, the following forms for the wave functions. For the initial bound state

$$\phi_i(\mathbf{r}) = -C_i i^{l_i} \gamma h_{l_i}^{(1)}(i\gamma r) Y_{l_i,m_i}(\theta,\phi). \tag{2.18}$$

Due of the strong core absorption discussed in Sec. 2.4 and to get a simple insight at the physics of unbound nuclei, we use in this work the asymptotic form of the initial state wave function, however the exact wave function, numerical solution of the bound state Schrödinger equation can be used without introducing further complexity in the calculations. For the final continuum state

$$\phi_f(\mathbf{r}) = C_f k \frac{i}{2}(h_{l_f}^{(-)}(kr) - S_{l_f} h_{l_f}^{(+)}(kr)) Y_{l_f,m_f}(\theta,\phi). \tag{2.19}$$

As it was shown in Ref.[21], in the case of narrow isolated resonances the treatment of the continuum states via the S-matrix is equivalent to the R-matrix formalism.

2.2.2 Probability spectrum

The probability to excite a final continuum state of energy ε_f is an average over the initial state

$$P_{in} = \frac{1}{2l_i+1}\Sigma_{m_i,m_f}|A_{fi}|^2 \tag{2.20}$$

and a sum over the final states. Introducing the quantization condition

$$kL = n\pi, \tag{2.21}$$

and the density of final states, according to Ref. [21]

$$\rho(\varepsilon_f)d\varepsilon_f = \frac{L}{\pi}\frac{m}{\hbar^2 k}d\varepsilon_f, \tag{2.22}$$

the probability spectrum reads

$$\frac{dP_{in}}{d\varepsilon_f} = \frac{2}{\pi}\frac{v_2^2}{\hbar^2 v^2}C_i^2\frac{m}{\hbar^2 k}\frac{1}{2l_i+1}\Sigma_{m_i,m_f}|1-\bar{S}_{m_i,m_f}|^2|I_{m_i,m_f}|^2, \tag{2.23}$$

where now

$$|I_{m_i,m_f}|^2 = \left| \int_{-\infty}^{\infty} dz e^{iqz} i^{l_i} \gamma h_{l_i}^{(1)}(i\gamma r) Y_{l_i,m_i}(\theta,0) k \frac{i}{2} h_{l_f}^{(-)}(kr) Y_{l_f,m_f}(\theta,0) \right|^2 . \tag{2.24}$$

For simplicity the equations in this section are obtained without spin variables in the initial and final states. The generalization including spin is given in Appendix B.

2.2.3 Approximate evaluation of the integral $I(k,q)$

In order to study the qualitative effects of the final state interaction we proceed now to an approximate evaluation of the integral $I(k,q)$ for $l_i = l_f = 0$. However the calculations presented in Sec. 2.5 use the exact integrals. For large impact parameters b_c, write $r = \sqrt{b_c^2 + z^2} \approx b_c + z^2/2b_c$. Then

$$\begin{aligned} I(k,q) &\approx \frac{1}{b_c^2} e^{-(\gamma - ik)b_c} \int_{-\infty}^{\infty} dz\, e^{-(\gamma - ik)z^2/2b_c} \cos(qz) \\ &= \frac{1}{b_c^2} \sqrt{\frac{2\pi b_c}{(\gamma - ik)}} e^{-(\gamma - ik)b_c} \exp\left(-\frac{b_c q^2}{2(\gamma - ik)} \right) . \end{aligned} \tag{2.25}$$

Hence the phase ν will be given by

$$\begin{aligned} \nu &= -\frac{1}{2} arg(\gamma - ik) + kb_c - \frac{kb_c q^2}{2(\gamma^2 + k^2)} \\ &= -\frac{1}{2} arg(\gamma - ik) + kb_c \left(1 - \frac{\gamma^2 + k^2}{8\bar{k}^2} \right) \end{aligned} \tag{2.26}$$

where $\bar{k} = mv/\hbar$ and we have used Eq.(2.4) to obtain $q = (\gamma^2 + k^2)/2\bar{k}$. The estimated value of $|I|^2$ is

$$\begin{aligned} |I|^2 &= \frac{1}{b_c^4} \frac{2\pi b_c}{\sqrt{\gamma^2 + k^2}} e^{-2\gamma b_c} \exp\left(-\gamma b_c \frac{\gamma^2 + k^2}{4\bar{k}^2} \right) \\ &= \frac{1}{b_c^3} \frac{2\pi}{\sqrt{\gamma^2 + k^2}} \exp\left(-2\gamma b_c \left(1 + \frac{q}{4\bar{k}} \right) \right) . \end{aligned} \tag{2.27}$$

The above analytical expressions are accurate to within 10% for impact parameters around the strong absorption radius and for neutron-core energies less that 1.5MeV. The agreement improves for larger impact parameters.

The approximate formulae give rise to simple physical interpretations. The first is that we have an explicit expression for the dependence of ν on the neutron wave number k, the core-neutron impact parameter b_c and the adiabaticity parameter $q/\bar{k}$. We will discuss some of the effects of the new phase ν in Sec. 2.5. $|I|^2 \sim \frac{e^{-2\gamma b_c}}{b_c^3}$ can be interpreted as an inelastic-like form factor and it is interesting to compare it to the transfer to the continuum form factor $\frac{e^{-2\eta b_c}}{b_c}$ given in Ref.[21]. The inelastic form factor decreases with the impact parameter much faster than the transfer form factor. This is a well known characteristic for final bound states [63] and it is interesting to see that it persists for final continuum states. Furthermore the slope parameters are in both cases given in lowest order by the initial state decay length γ.

Finally we make connection with the sudden approximation formula Eq.(20) of Ref.[45] which describes the second step of a two neutron breakup reaction as a resonance decay, when the first neutron has been stripped. In our notation it reads

$$\begin{aligned} \frac{d\sigma}{d\varepsilon_f} &\sim \frac{1}{k(\gamma^2+k^2)}\left(\frac{k\cos\delta+\gamma\sin\delta}{\sqrt{\gamma^2+k^2}}\right)^2 \\ &\sim \frac{1}{k}\frac{|\sin(\delta+\beta)|^2}{(\gamma^2+k^2)}, \end{aligned} \tag{2.28}$$

where $\beta = arctan(k/\gamma)$. This formalism also predicts the presence of an extra phase shift β with respect to the free particle scattering determined by δ since $|\sin(\delta+\beta)|^2 = \frac{1}{4}|1-\tilde{S}|^2$ and $\tilde{S} = e^{2i(\delta+\beta)}$. Similarly to our case the effect of β would be to modify the resonance-like structures. In both cases then $\bar{S}$ and $\tilde{S}$ could be interpreted as off-the-energy-shell S-matrices. On the other hand our additional phase ν contains an explicit dependence on the impact parameter and we calculate the potential phase shift and S-matrix by an optical model code. Our S-matrix can in principle be complex to allow for core excitation effects. Also it can consistently, and in the same formalism, describe resonant and non-resonant final continuum states of angular momentum $l_f = 0$ but also $l_f > 0$. In the latter case, the Breit-Wigner assumption for the line shape of the resonances used in other approaches, is naturally given by the optical model calculation of the factor $|1-\bar{S}|^2$ in Eq.(2.23).

In [63], it was shown that the semiclassical treatment of peripheral quasi-elastic reactions is valid for transfer reactions as well as for (inelastic) projectile excitation and therefore we will apply it in the following by simply substituting $P_{in}(b_c)$ to $P_t(b_c)$ in the formula, Eq.(1.1), which gives the cross section in terms of the neutron excitation probability and the core elastic scattering probability. The only difference is that here ε_f is the neutron final energy with respect

to its core of origin.

Because $P_{in}(b_c)$ depends on b_c trough the form factor I_{m_i,m_f}, the final cross sections will get the main contribution from a limited range of impact parameters around the strong absorption radius. As we shall see in the following (cf. figs.7 and 8) this localization makes the tails of the spectra from Eqs.(2.23) and (1.1) to decay faster than Eq. (2.28) towards neutron-core high energies.

2.3 Two-nucleon breakup

This section introduces the basis for a generalization of Eq.(1.1) which will be further expanded elsewhere. The goal is to take into account explicitly the presence of a second, stripped, nucleon as in the cases of projectiles like ^{14}Be which have a two-neutron halo or ^{14}B in which a proton can also emitted.

We start from hypothesis similar to those leading to Eq.(2.3) of Ref.[45] which gives, in the case of two-neutron breakup, the one-neutron-core relative momentum distribution when the other neutron is stripped. Let us call (1) the stripped neutron and (2) the neutron detected in coincidence with the core. Following the approximations proposed by Ref.[45] for the coordinate variables, shown in Fig.2.2, of the core and neutrons with respect to the target one gets: $R_{1\perp}$=$r_{1\perp}$+b_c and $R_{2\perp}$= $r_{2\perp}$+b_c, where the heavy-core approximation has been used. r_1 and r_2 are the coordinates of neutron (1) and (2) with respect to the core, while R_1 and R_2 are with respect to the target.

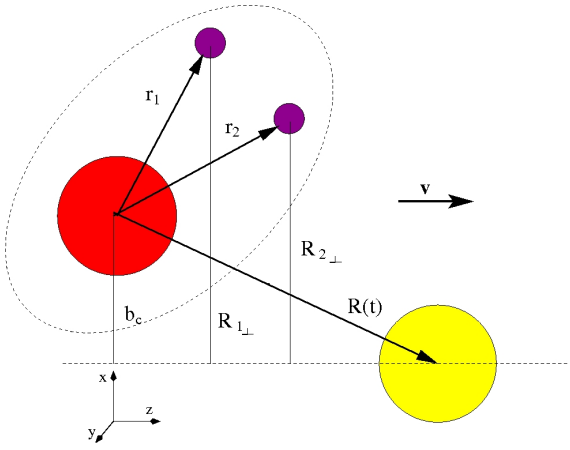

Figure 2.2: Coordinate system used in the calculations of two-nucleon breakup.

Suppose the initial two-neutron wave function to be given by a product of single particle wave-functions, as in the shell model: $\Psi(\mathbf{r}_1,\mathbf{r}_2) = a_1[\phi_1(\mathbf{r}_1)\phi_2(\mathbf{r}_2)]$ with spectroscopic factor

$a_1^2 = C^2S$. For simplicity we consider here only a $l_i = l_f = 0$ transition and thus we do not include spin wave functions. Then the neutron- core cross section differential in the relative energy is:

$$\frac{d\sigma_{-2n}}{d\varepsilon_f} = 2C^2S \int d^2\mathbf{b}_c |S_{ct}(b_c)|^2 \frac{dP_{in}(b_c)}{d\varepsilon_f} \int d^2\mathbf{r}_{1\perp}(1-|S_1(\mathbf{R}_{1\perp})|^2) \int dz |\phi_1(\mathbf{r}_{1\perp},z)|^2. \quad (2.29)$$

Where $dP_{in}(b_c)/d\varepsilon_f$ is given by Eq.(2.23) and, similarly to Eq.(1.1), we are treating the core-target interaction in the eikonal approximation. The $d^2\mathbf{r}_{1\perp}$ integral above gives the neutron (1) stripping probability. For the S_1-matrix we consider a sharp cut-off approximation such that $S_1(\mathbf{R}_{1\perp}) = 0$ if $0 < \mathrm{R}_{1\perp} < \mathrm{R}_T$, while $S_1(\mathrm{R}_{1\perp}) = 1$ if $\mathrm{R}_{1\perp} > \mathrm{R}_T$ and R_T is the target radius.

Thus we obtain a simple expression for the two nucleon breakup cross section, in which one is stripped by the target while the other is elastically scattered and interacts with the core in the final state

$$\frac{d\sigma_{-2n}}{d\varepsilon_f} = 2C^2S \int d^2\mathbf{b_c} |S_{ct}(b_c)|^2 \frac{dP_{in}(b_c)}{d\varepsilon_f} \int d^2\mathbf{r}_{1\perp} \int dz |\phi_1(\mathbf{r}_{1\perp},z)|^2, \quad (2.30)$$

as a product of the neutron (2)-core relative energy distribution and a factor depending on the stripped neutron (1) wave function. For each core- target impact parameter b_c the limits of the integral on $\mathrm{r}_{1\perp}$ are: $\mathrm{b}_c - \mathrm{R}_T < r_{1\perp} < \mathrm{b}_c$.

2.4 Application: The reaction ^{11}Be $\rightarrow$ n+^{10}Be

As a test of our model we calculate the relative energy spectrum n+^{10}Be obtained by the authors of Ref.[54] in the breakup reaction of ^{11}Be on ^{12}C at 70 A.MeV. The structure of ^{11}Be is well known: the valence neutron is bound by 0.503 MeV; the wave function is mainly a 2s state with a spectroscopic factor around 0.8 and there is also a small $\mathrm{d}_{5/2}$ component. The main $\mathrm{d}_{5/2}$ strength is in the continuum centered around 1.25 MeV [33]. We have calculated the initial wave function for the s-state in a simple Woods-Saxon potential with strength fitted to the experimental separation energy and whose parameters are: r_0=1.25 fm, a=0.8 fm. As possible final states we have considered only the s, p and d partial waves calculated in the l-dependent potentials of Table 2.2. The delta-function potential strength has been chosen as -4057.59 MeV fm^3. The authors of Ref.[54] have shown that the effect of Coulomb breakup is noticeable in their n+^{10}Be spectrum. We have also included this contribution, calculating it with the method of Margueron et al. [46] which explicitly takes into account the recoil of the core.

Table 2.1: Experimental bound-state and resonance energies (E_{exp}), width (γ_{exp}) and quantum numbers of ^{11}Be [91, 92]

J^π	l	E_{exp} (MeV±keV)	γ_{exp} (keV)
$\frac{1}{2}^+$	0	-0.504±6	
$\frac{1}{2}^-$	1	-0.184±7	
$\frac{5}{2}^+$	2	1.274±18	100±20

Table 2.1 summarizes the experimental results on the spectrum of single nucleon states in ^{11}Be. If ^{11}Be were simply ^{10}Be(ground state)+n, the simplest shell model would imply that the ground state should have $J^\pi = 1/2^-$ since the lowest available orbit for the extra neutron is a $p_{1/2}$ orbit. However, the ground state has $J^\pi = 1/2^+$. The inversion of $1/2^+$ and $1/2^-$ in ^{11}Be has been known for a long time and it is interpreted as the presence of strong correlations between the neutron and the core. We shall see in the next chapter that, using Eq.(3.102), we reproduce a neutron halo nucleus of the correct radius by putting an $s_{1/2}$ orbit into the correct position to obtain the parity inversion. In our case, we use such a ^{11}Be as a substructure for ^{12}Be, in the calculations presented in chapter 3.

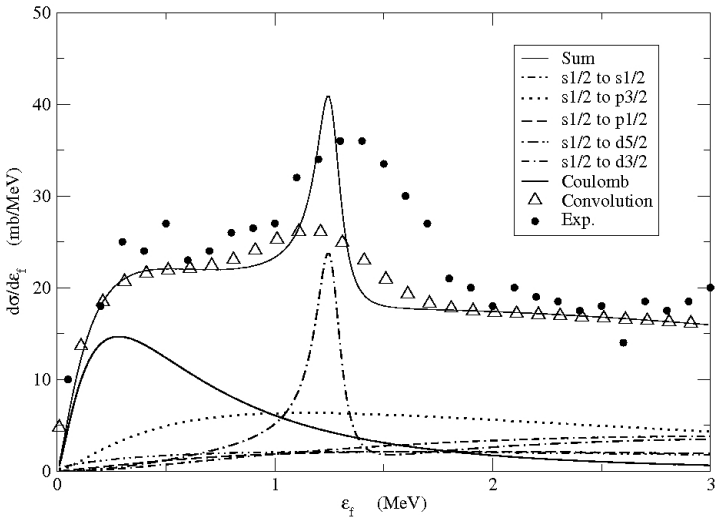

Figure 2.3: n-^{10}Be relative energy spectrum, including Coulomb and nuclear breakup for the reaction ^{11}Be+^{12}C → n+ ^{10}Be+X at 69 A.MeV. Only the contributions from an s initial state with spectroscopic factor C^2S= 0.84 are calculated. The triangles are the total calculated result after convolution with the experimental resolution function. The dots are the experimental points from [54].

The spectrum of Fig.2.3 is very similar to the spectrum obtained in Ref.[65] by solving the time-dependent Schrodinger equation numerically, expanding the projectile wave function

Table 2.2: Woods-Saxon potential parameters for the s, p and d states in the ^{11}Be continuum.

	l=0	l=1	l=2	V_{so}(MeV)	a (fm)	R (fm)
V_0(MeV)	-62.52	-39.74	-63.57	5.25	0.6	2.585

upon a three-dimensional spherical mesh. Similarly to the present model, a classical, straight line trajectory for the core-target scattering was used in Ref.[65]. Also our n-core potentials are very close to those of Ref.[65] and our δ-interaction strength is consistent with the volume integral of their neutron-target interaction.

We have then folded the calculated spectrum through the experimental resolution function of Fukuda et al. [54], as given in Ref.[65]

$$\frac{d\sigma^{conv}_{-1n}}{d\varepsilon} = \int \frac{d\sigma^{theo}_{-1n}}{d\varepsilon_f} g(\varepsilon_f - \varepsilon) d\varepsilon_f,$$
$$g(\varepsilon_f - \varepsilon) = \frac{1}{0.48\sqrt{\varepsilon_f}} \exp\left(-\frac{(\varepsilon - \varepsilon_f)^2}{0.073\varepsilon_f}\right), \tag{2.31}$$

with ε_f the energy in the theoretical calculation. The result is shown in Fig.2.3 by the triangles. The full curve is the total spectrum, sum of Coulomb and nuclear breakup. Each individual transition, due to the nuclear interaction only, is also shown. The dots are the experimental points from [54]. Our calculations include an initial state spectroscopic factor C^2S=0.84. The kind of discrepancy between our calculation and the data in the range 1-2 MeV is very similar to that of the calculations in Ref.[65].

2.5 Application: The reactions ^{14}Be$\rightarrow^{13}$Be +n and ^{14}B$\rightarrow^{13}$Be +p

An interesting unbound nucleus which has recently attracted much attention is ^{13}Be. It has been obtained in several different type of experiments with normal and exotic beams but its structure is not clear yet. One of the aims of this section is to see whether the neutron-^{12}Be relative energy spectra obtained from fragmentation of ^{14}Be or ^{14}B would show differences predictable in a theoretical model. Therefore we start by describing briefly the present knowledge of ^{13}Be.

2.5.1 Structure of ^{13}Be

The first experimental evidence of ^{13}Be was recorded in Ref. [58]. It was the unobserved particle in the two-body reaction ^{14}C(^{7}Li,^{8}B) at 82 MeV. A narrow resonance at 2 MeV above the neutron emission threshold was observed in the spectrum of the measured ^{8}B ions and it was interpreted as being due to the ground state of ^{13}Be. Later on it was identified as a $d_{5/2}$ state in the double-charge exchange experiment ^{13}C(^{14}C,^{14}O) at E_{inc}=337 MeV [59] and in an inverse kinematics (d,p) transfer reaction at 55 A.MeV [60]: both the missing mass method, from the detected proton spectrum, and the invariant mass spectroscopy, from the measurement of all the decay products from the unbound state were used. The $d_{5/2}$ resonance was considered as the ground state of ^{13}Be until the experiment of Ref. [61]. This experiment used a stable beam multi-nucleon transfer process ^{14}C(^{11}B,^{12}N)^{13}Be in which a lower state, unbound by 800 keV was observed. A spin J=1/2 was suggested but without parity assignment. More recently a broad peak has been obtained in several projectile fragmentation experiments [10, 66, 67, 68] and tentatively identified as a $1/2^{+}$ state. The experiment of Ref.[66] used fragmentation of ^{18}O at 80 A.MeV. Neutrons in coincidence with ^{12}Be were detected and the broad peak was observed in their relative velocity spectrum. The spectrum was fitted with a virtual s-state of energy 60 keV while in Ref.[10], which used fragmentation of ^{14}B a virtual s-state could not fit the experimental neutron spectrum. The assumption of an s-resonance of energy 700 keV and width 1.3 MeV leads to a good agreement. In Refs. [10, 56, 67, 68] these unbound states of ^{13}Be have been populated by breakup of ^{14}Be or ^{14}B. Both types of experiments show a low energy peak but only in the breakup of ^{14}B [10, 56] the other peak at 2 MeV corresponding to the $d_{5/2}$ state, is seen clearly. Finally Simon et al. [67] have fitted their spectrum from ^{14}Be breakup with s, p and d components.

Simon et al. [67, 83], see Fig. 2.4 and Fig. 2.5, from a break up experiment of ^{14}Be on a ^{12}C target at 287 A.MeV, studied also ^{13}Be and showed that a possible contribution to the spectrum could come from a $1/2^{-}$ low lying state. This is the hypothesis we made previously when applying our fragmentation model to ^{14}Be. Indeed, we showed that a low-lying s-state would not be populated enough and a contribution from a p-state is needed to interpret the experimental n+^{12}Be spectrum with our fragmentation model. Therefore we wish to test this hypothesis with our fragmentation model and in the next chapter with the p-p RPA structure model. Therefore to disentangle the various theoretical descriptions of ^{13}Be and ^{14}Be one needs more precise experimental information on the structure of both and in particular on their spectroscopic factors.

2.5.2 Structure and experiments of ^{14}Be and ^{14}B

These uncertainties in the interpretation of experimental results as compared to structure calculations were at the origin of our motivations to try to understand whether the neutron-^{12}Be

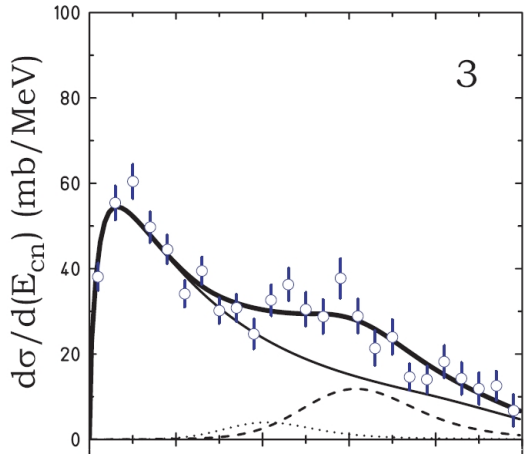

Figure 2.4: GSI, H. Simon et al. Taken from [67] (2004).

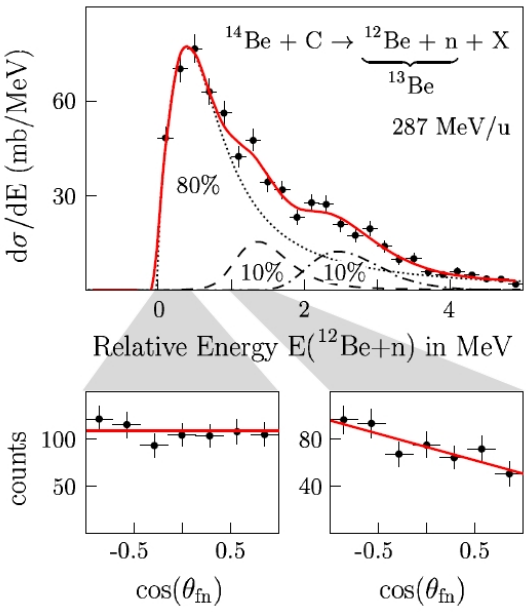

Figure 2.5: GSI, H. Simon et al. Taken from [83] (2002).

relative energy spectra obtained from fragmentation of ^{14}Be or ^{14}B would show differences predictable in a theoretical model. It is likely that if differences will be found in the experimental results with ^{14}B and ^{14}Be beams they could be due to an interplay between structure and reaction effects. The ground state of ^{14}Be has spin $J^{\pi} = 0^{+}$. In a simple model assuming two neutrons added to a ^{12}Be core in its ground state the wave function is:

$$|^{14}Be> = [b_1(2s_{1/2})^2 + b_2(1p_{1/2})^2 + b_3(1d_{5/2})^2] \otimes |^{12}Be, 0^{+}> \tag{2.32}$$

Then the bound neutron can be in a 2s, $1p_{1/2}$ or $1d_{5/2}$ state. However, as it has been discussed in the previous section, the situation is much more complicated [69]-[75] and in particular the calculations of Ref. [76] show that there is a large component $(2s_{1/2}, 1d_{5/2}) \otimes |^{12}Be, 2^{+}>$ with the core in its low energy 2^{+} state which can modify the neutron distribution. A detailed microscopic model of ^{14}Be will be discussed in the following chapter.

The halo structure of ^{14}Be has been confirmed by Zahar et al. [117] in a fragmentation experiment of ^{14}Be on a ^{12}C target. The authors suggest a strong correlation between the two external neutrons.

On the other hand, the two-neutron separation energy of ^{14}Be has been the subject of two experiments. The first, a pion double charge-exchange measurement [100], gave 1.12 ± 0.16 MeV. The second, a time-of-flight experiment [101], gave 1.48 ± 0.14 MeV. The most accepted value is S_{2n}=1.34 $\pm$ 0.11 MeV, being the weighted average of them. An experiment by Labiche et al. [118] studied the dissociation of ^{14}Be at 35 MeV/nucleon on carbon and lead targets in a

kinematically complete measurement. Comparisons of the data with a three-body model calculations suggested that the ground state wave function of ^{14}Be includes a strong $(2s_{1/2})^2$ state admixture. The ^{14}Be rms is known from Ozawa et al. [104] to be 2.94 $\pm$ 0.09 fm. Sugimoto et al. [103], with the break up experiment: ^{14}Be + ^{12}C at 68 A.MeV, obtained a 2^+ state at E_{ex}=1.54(13) MeV. They also extracted the deformation length through a DWBA analysis as $\delta = 1.18 \pm 0.13$fm.

The ^{14}Be has been studied theoretically in different ways. Bertsch and Esbensen investigated ^{13}Be and ^{14}Be using a two-neutron pairing model [69] in which ^{14}Be is described as an inert core and two interacting neutrons. The ^{14}Be two-neutron separation energy, $S_{2n} = 1.34 \pm 0.11$ MeV, was reproduced using a $d_{5/2}$ resonance at 2.4 MeV and an unbound $2s_{1/2}$ ground state in ^{13}Be.

Descouvemont et al. [73] studied ^{14}Be as an inert core surrounded by two external neutrons and they came to the conclusion that the assumption of an inert core should be treated with caution when the core nucleus has a low excitation energy. Their main conclusion from the ^{13}Be study was that a $1/2^+$ state is predicted below the experimentally known $5/2^+$ resonance and should be located very close to the neutron threshold, which is a common feature in the previously observed Borromean systems. It turns out that the GCM can reproduce the ^{14}Be(0^+) and ^{13}Be($5/2^+$) energies simultaneously. They found a slightly negative energy (-19 keV) for the s-state, but this small value was far beyond the accuracy level of the model. Their calculation indicates that core excitations are important in the ^{14}Be wave function since the ^{12}Be (g.s.)+n+n configuration represents 66% only of the total wave function.

The microscopic neutron-^{12}Be potential derived by Descouvemont was used in a Lagrange-mesh calculation of ^{14}Be by Adahchour et al. [74]. The Lagrange-mesh techniques have proved to give a simple and accurate solution of the three-body ^{12}Be+n+n Schrödinger equation. Calculations show that a renormalization of the neutron-core potential, by a factor 1.06, is needed in order to obtain a neutron separation energy of ^{14}Be of 1.18 MeV.

In Ref. [70], the Faddeev three-body approach was used by Thompson and Zhukov, who also treated ^{14}Be as an inert ^{12}Be core interacting with valence nucleons via a single channel l-dependent Woods-Saxon potential. It was found that in order to keep ^{13}Be unbound, and at the same time to describe correctly the binding of ^{14}Be, the position of the $d_{5/2}$ resonance had to be lowered to 1.3 or 1.0 MeV. When they obtain the good binding energy for ^{14}Be, they find a bound ^{13}Be. Therefore this model cannot be considered realistic.

Tarutina et al. [76] described ^{13}Be and ^{14}Be as one and two neutrons outside a deformed ^{12}Be core, which is treated as a rigid rotor and the neutron-core interaction is approximated by a deformed Woods-Saxon potential. The ^{12}Be core is assumed rotational and it is allowed to excite to its first 2^+ state. Their three-body description of ^{14}Be uses the hyperspherical expansion formalism, including the core degrees of freedom. They explore those potential parameters compatible with the known properties of ^{12}Be, ^{13}Be and ^{14}Be. They find that both ^{14}Be and ^{13}Be can be described simultaneously provided the ^{12}Be core has a large positive quadrupole

deformation.
Pacheco and Vinh-Mau [71] used the same particle-particle RPA that we are using in this work. They proposed several different scenarii for the structure of ^{13,14}Be, fixing the $d_{5/2}$ resonance at 2 MeV. Their model however predicts a $1/2^-$ ground state in ^{13}Be.

The ground state of ^{14}B has spin $J^\pi = 2^-$. In a model where it is described as a neutron-proton pair added to a ^{12}Be core in its 0^+ground state with the proton in the $1p_{3/2}$ shell, its wave function may be written as:

$$|^{14}B>=[a_1(p_{3/2},2s_{1/2})+a_2(p_{3/2},d_{5/2})]\otimes|^{12}Be,0^+> \tag{2.33}$$

The present experimental information [77] on ^{14}B is that the neutron is in a state combination of s and d-components with weights 66% and 30% respectively, while shell model calculations show a similar mixture and no component with an excited state of the core. There are two possibilities for the reaction mechanism. One is that a proton is knocked out in the reaction with the target. The remaining ^{13}Be would be left in an unbound s-state with probability $|a_1|^2$, in a $d_{5/2}$-state with probability $|a_2|^2$. These unbound states would decay showing the s-wave threshold and d-wave resonance effects. As mentioned in the introduction, the second possibility is that the neutron is knocked out first due to its small separation energy and that the proton is stripped from the remaining ^{13}B. We show in Sec. 2.5 that this can also lead to resonance-like effects in the cross section.

2.5.3 Asymptotic normalization

In Table 2.3, the asymptotic normalizations are given for the initial state wave function parameters used in the calculation. They have been obtained from a wave function calculated in a Woods-Saxon potential with the following parameters: $r_0 = 1.27A^{1/3}$, $a = 0.75$fm.

2.5.4 Average one-neutron potential

The link between reaction theory and structure model is made by the neutron-core potential determining the S-matrix in Eq.(2.10). Then if the theory fits the position and shape of the continuum n-nucleus energy distribution, obtained for example by a coincidence measurement between the neutron and the core, the parameters of a model potential can be deduced. Our initial bound states are obtained in a simple Woods-Saxon with R= $r_0A^{1/3}$

Table 2.3: Asymptotic normalization constants C_i ($fm^{-1/2}$) for the initial state wave functions of the bound neutron. Potential parameters are: V_0 fitted to give the two energies -0.97 MeV and -1.85 MeV, which are the known neutron binding energies in ^{14}B and in ^{14}Be respectively [78]. The other potential parameters are r_0=1.27fm, a=0.75fm, V_{so}=5.25MeV.

ε_i(MeV)	-0.97	-1.85
l_i, j_i	$C_i(fm^{-1/2})$	
0 1/2	1.31	1.99
1 1/2	0.55	0.88
2 5/2	0.17	0.34

$$V_{WS}(r) = \frac{V_0}{1+e^{(r-R)/a}} - \left(\frac{\hbar}{m_\pi c}\right)^2 \frac{V_{so}}{ar}\frac{e^{(r-R)/a}}{(1+e^{(r-R)/a})^2}\mathbf{l}\cdot\sigma. \tag{2.34}$$

The depth is adjusted to fit the binding energies given in Table 2.3 and Fig.2.12. Other parameters are also given in Table 2.3. To describe the valence neutron in the ^{13}Be continuum we assume that the single neutron Hamiltonian with respect to ^{12}Be has the form

$$h = t + U + iW, \tag{2.35}$$

where t is the kinetic energy and

$$U(r) = V_{WS} + \delta V, \tag{2.36}$$

is the real part of the neutron-core interaction. For the time being the imaginary part is taken equal to zero. V_{WS} is again a Woods-Saxon potential plus spin-orbit whose parameters are given in Table 2.4, and δV is a correction [53]:

$$\delta V(r) = 16\alpha e^{2(r-R)/a}/(1+e^{(r-R)/a})^4, \tag{2.37}$$

which originates from particle-vibration couplings. They are important for low energy states but can be neglected at higher energies. The above form is suggested by a calculation of such couplings using Bohr and Mottelson collective model of the transition amplitudes between zero and one phonon states. Therefore our structure model is not a simple *single-particle in a potential* model but contains in it the full complexity of single-particle vs. collective couplings. The details of our structure model are the subject of next chapter. If simple fittings of experimental data will be obtained, then the parameters of a semi-phenomenological potential can be deduced and linked to a more microscopic model. A more realistic treatment would require the description of both bound and unbound states in a three-body model such as in Refs.[79] and [80].

Table 2.5 gives the energies and widths of the $1p_{1/2}$ and $1d_{5/2}$ states, chosen according to Ref.[53] with different values of the strength α. The widths are obtained from the phase shift variation near resonance energy, according to $d\delta_j/d\varepsilon_f|_{\varepsilon_{res}} = 2/\Gamma_j$, once that the resonance energy is fixed [47]. We stress here that while the position of our $d_{5/2}$ resonance agrees with the experimental evidences discussed in Sec. 2.4.3, the position of our $1p_{1/2}$ resonance is only an hypothesis [53, 81].

2.5.5 Results

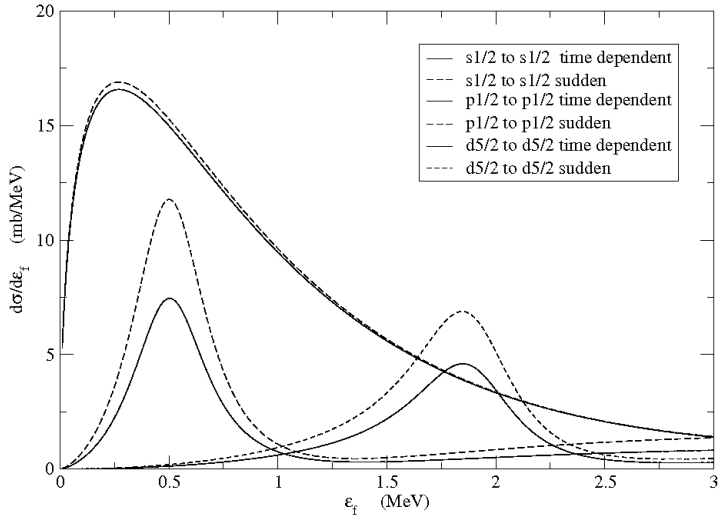

Figure 2.6: Population of resonances in the n-^{12}Be relative energy spectrum. Comparison of sudden (dashed line) and non-sudden (solid line) results for an s $\rightarrow$ s transition with peak at 0.25 MeV, p$\rightarrow$ p with peak at 0.5 MeV and d$\rightarrow$ d transition with peak around 2 MeV. See text for details.

Results obtained with the model outlined in Secs. 2.2 and 2.4 will now be discussed. We

Table 2.4: Woods-Saxon and spin-orbit potential parameters for the continuum final states.

V_0 (MeV)	r_0 (fm)	a (fm)	V_{so} (MeV)	a_{so} (fm)
-39.8	1.27	0.75	6.9	0.75

Table 2.5: Energies and widths of unbound p- and d-states in ^{13}Be and corresponding strength parameters for the δV potential.

	ε_{res} (MeV)	Γ_j (MeV)	α (MeV)
$1p_{1/2}$	0.67	0.28	8.34
$1d_{5/2}$	2.0	0.40	-2.36

describe the reaction corresponding to a neutron initially bound in ^{14}Be or ^{14}B which is then excited into an unbound state of ^{13}Be, assuming that another nucleon has been emitted and stripped by the target, thus not detected in coincidence with the core. The sudden approximation studied in Ref.[69], similar to our q=0 case, was found to be excellent for energy distributions like those discussed in this work.

One of the goals of the present calculations, as far as the reaction model is concerned, is to understand the incident energy dependence of the breakup cross-section and the dependence on the neutron initial binding energy. Related to this is the investigation of the validity of the sudden approximation and the accuracy necessary in calculating the phase shifts. Finally we wish to understand how the presence of p- and d-wave resonances, besides a threshold s-state in the final state, can affect the results.

As a preliminary to a future, more accurate, study of the breakup of ^{14}Be and ^{14}B in a fully time dependent method, we consider the knockout of a single neutron from a bound state in a potential, similarly to the previous calculation for ^{11}Be. The calculations in the present section are made with different potentials for the initial and final state. The initial state is bound with a separation energy in the range 1-2 MeV and the final state is unbound. The continuum energies can be adjusted by varying the parameter α in the potential. By changing the strength α of the δV potential in Eq.(2.37) we will make also the 2s-state just bound near threshold and see what would be the effect on the continuum spectrum. The delta-interaction strength used in Eq.(2.6), is v_2=-8625 MeV fm^3. It has been obtained by imposing that this interaction gives the same volume integral as a n-^{12}C Woods-Saxon potential of strength -50.5 MeV, radius 2.9 fm and diffuseness 0.75 fm. With a diffuseness of 0.5 fm one would obtain v_2=-6717 MeV fm^3. The value v_2=-7481 MeV fm^3 would be obtained from a Woods-Saxon with the same geometry and a depth fitted to give the experimental neutron separation energy in ^{13}C.

First we study the differences between results from Eqs.(2.23) and (1.1), the sudden approximation limit q=0 of those equations and Eq. (2.28). In Fig.2.6 we show the calculation of the differential probability for the transition from a bound s-state to an unbound s-state, a bound p-state to an unbound p-state and a bound d-state to an unbound d-state. The initial state parameters are given in Table 2.3. The full lines correspond to the case ε_i=-1.847 MeV, E$_{inc}$=70

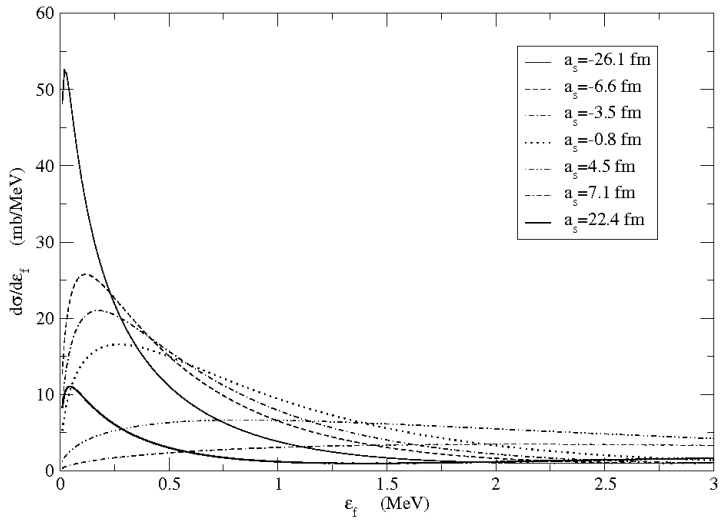

Figure 2.7: Comparison of results obtained considering a final s-state for the n-^{12}Be relative energy spectrum with positive and negative scattering lengths. Scattering lengths are given on the figure and their corresponding δV potential strengths in Table 2.6.

A.MeV corresponding to v=11.35 (fm$\times 10^{22}$ sec^{-1}) and q in the range (0.025 $\rightarrow$ 0.065) fm^{-1}. The dashed lines give the q=0 calculations of Eqs.(2.23) and (1.1). There is a small difference in the absolute value of the probability and the sudden calculation results have slightly different widths in the s to s case. In the other two cases the differences are noticeable. We have considered only the three transitions keeping $j_i = j_f$ as it would happen in an extreme sudden transition. Then we studied the effect of the extra phase in Eqs.(2.23) and (2.28) on the position of the resonance peaks, and we found that the shift is negligible and would not be noticeable for the range of neutron-core energies discussed here. Also we have calculated for several velocities ranging from 10 to 23 (fm$\times 10^{22}$ sec^{-1}) and found no noticeable differences. On the other hand changing the initial binding energy from -0.97 MeV to -1.85 MeV gives a widening of the distribution and a slight shift of the peak value, as shown in Fig.2.12. These two energies are the known neutron binding energies in ^{14}B and in ^{14}Be respectively [78]. In this work we have kept the initial separation energy fixed at the value 1.85 MeV, unless otherwise stated. Our conclusion is that for fragmentation reactions such as those discussed here, the sudden approximation q=0 in Eqs.(2.23) and (1.1), is well justified from the point of view of the independence from the beam velocity. On the other hand the value of the $\varepsilon_f - \varepsilon_i$ difference has an important effect on the results when the final energy increases and for states with $l_f > 0$.

The first peak shown by the experimental spectra of ^{13}Be needs to be studied in great detail

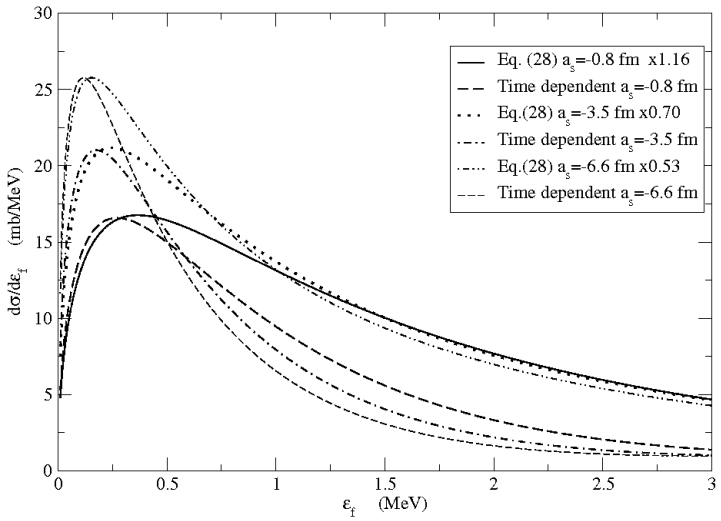

Figure 2.8: Comparison of time dependent calculation for an s to s transition with results of Eq.(2.26) using the same optical model phase shifts corresponding to scattering lengths as indicated. For each case we give in the legend the normalization factor between the two calculations.

as it would help determining the ground state angular momentum and parity. In particular, if it is due to an s-state its characteristics will depend on its closeness to threshold. Therefore we study now such a point.

Low energy s-states

Using the effective range formula [47]

$$k\cot\delta_0 = -\frac{1}{a_s} + \frac{1}{2}r_e k^2, \tag{2.38}$$

in the case of a bound state of small binding energy $\gamma \rightarrow 0$ with $\gamma = \sqrt{-2m\varepsilon_i}/\hbar$ one has

$$-\frac{1}{a_s} = -|\gamma| + \frac{1}{2}r_e\gamma^2. \tag{2.39}$$

Equation (2.39) has been used [82] also to define an *energy* of unbound s-states of near zero energy. Such a procedure is reliable when γR is smaller than about 0.5, where R is the radius of the potential. Therefore the effective range formula is accurate only for very low energies. Thus we have fitted the behavior of our s-state phase shifts from the optical model calculation,

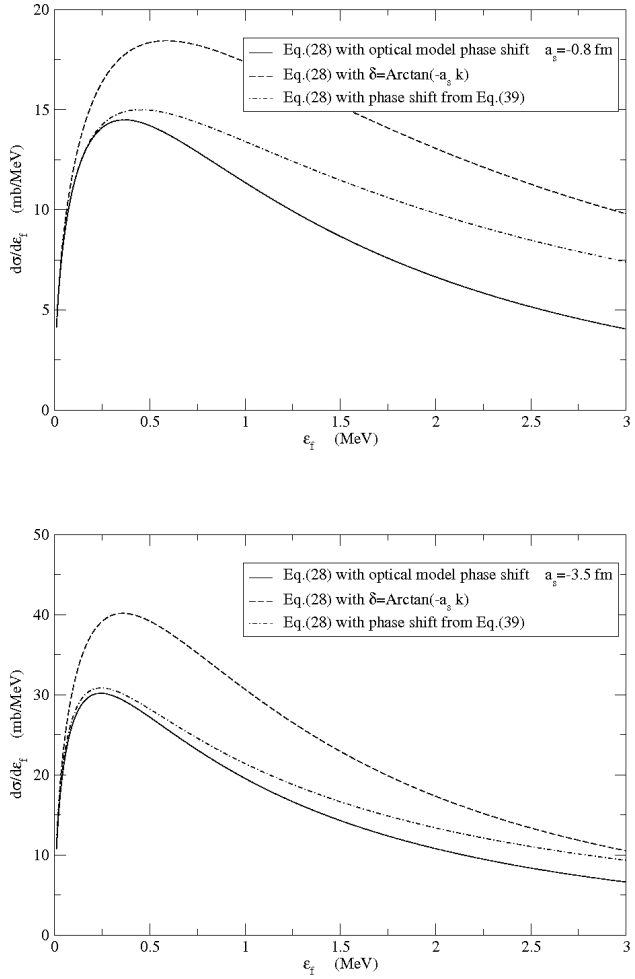

Figure 2.9: Results of Eq.(2.26) using three different prescriptions for the phase shifts corresponding to scattering lengths as indicated.

to Eqs.(2.38) and (2.39) and the corresponding parameters are given in Table 2.6. In the case of a bound state, the effective range values can also consistently be obtained from Eq.(2.39).

Figure 2.7 shows the influence of the phases δ and ν (cf. Eq.(2.15)) on the breakup cross sections.The results shown correspond to final s-states with positive and negative scattering lengths. Several cases are considered and the corresponding potentials, scattering lengths, and effective ranges are given in Table 2.6. The scattering length values were obtained from the phase shifts as $a_s = -\lim_{k\to 0} \frac{tan\delta_0}{k}$, and also cross-checked by solving the Schrödinger equation at zero energy. The bound state energies in the last column were obtained from the solution of the Schrödinger equation in each given potential. Notice that the breakup cross sections for potentials with negative scattering lengths are much larger than those with positive scattering

Table 2.6: Strengths of the s-state δV potential in Eq.(2.37) and corresponding scattering lengths, effective range parameter and *energy parameter* ε. The strength of the central Woods-Saxon part is V_0=-39.8 MeV in all cases (cf. Table 2.4).

α (MeV)	a_s (fm)	r_e (fm)	$\lvert\varepsilon\rvert$ (MeV)
8.0	-0.8	117.0	
4.0	-3.5	17.9	
2.0	-6.6	11.8	
-1.0	-26.1	7.58	
-5.0	22.4	5.9	0.06
-15.0	7.1	3.8	1.34
-35.0	4.5	2.7	6.49

lengths. This effect is mainly due to the influence of the phase ν.

The effective phase in Eq.(2.15) is $\bar{\delta} = \delta + \nu$ and there are interference effects which are especially important for an s-state final state. When k is small $\delta \approx -ka_s$ and it depends on the sign of the scattering length, while $\nu \approx k(b_c + 1/\gamma)$ and it is always positive. The part of the cross section Eq.(1.1) with the probability Eq.(2.23) for $l_f = 0$ and small k, depends on the relative sign of a_s and ν as

$$\frac{d\sigma}{d\varepsilon_f} \propto |\delta + \nu|^2 \approx |-ka_s + \nu|^2. \tag{2.40}$$

When $a_s < 0$ the cross section is increased relative to the value at $\nu = 0$, while for $a_s > 0$ it is reduced. This effect is seen clearly in Fig. 2.7. These interference effects can also explain why the cross section for a_s=4.8 fm is larger than for a_s=7.1 fm. Also, the decrease in the positive values of a_s shown in Table 2.6 corresponds to an increase in the depth of the potential δV. Fig. 2.7 shows that the cross section increases for the smallest values of a_s. As the attraction becomes ever stronger the scattering length changes sign and the cross section becomes larger. This effect is due to the influence of a continuum s-state coming close to threshold. When the final potential has a very weakly bound 2s-state with a_s=22.4 fm one sees a very narrow peak close to threshold (thick solid line) while for a_s= 4.5 fm, corresponding to a more strongly bound state, no peak at all, rather a kind of flat bump (double-dotdashed line).

The calculations presented in Fig. 1.5 of chapter 1, did not include the extra phase ν because the final state interaction with the core of origin was neglected while the final state interaction with respect to the other nucleus was included. In that case the neutron behaved as a free particle in the scattering on the other nucleus. Breakup cross sections depended quite strongly on the magnitude of the scattering length but had a weak dependence on its sign. The reaction

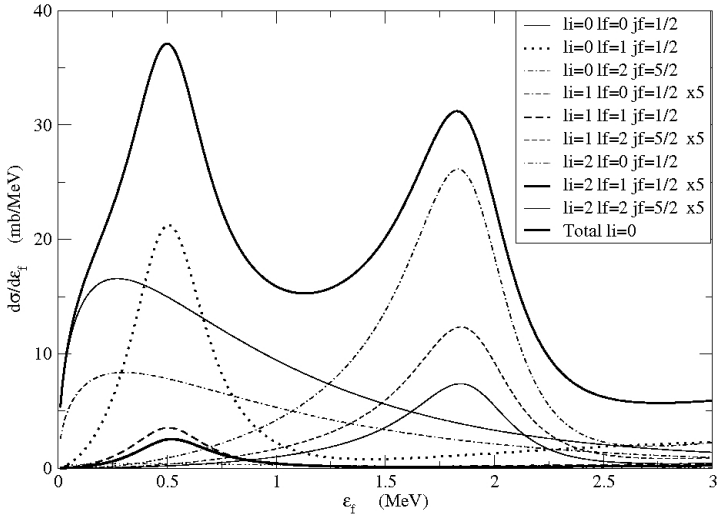

Figure 2.10: Results obtained including the s, p and d states. Each curve corresponds to just one transition as indicated. The solid curve is the sum of all transitions from the s-bound state. To make them visible some curves have been multiplied by a factor of five as indicated in the legend.

mechanism discussed in this work is instead an inelastic-type of excitation in which the final state interaction is with the core of the projectile and therefore the present formalism shows that the S-matrix in Eq.(2.17) as well as in Eq.(2.28) is effectively off-the-energy-shell. In the s $\rightarrow$ s case we show also in Fig. 2.8, a comparison between the results just discussed and those obtained using the optical model phase shifts in Eq.(2.28) and whose absolute values have been normalized to our peaks. As anticipated in Sec. 2.3 and 2.4, the curves from the time dependent model show a faster decrease towards high energies. This is because the form factors in Eq.(2.23) decrease rapidly and they have large values only for impact parameters close to the strong absorption radius.

Since Eq.(2.28) is quite simple to implement in a fit to experimental spectra, we have also studied its sensitivity to the choice of the phase shift. Fig.2.9 shows, for two scattering lengths, results obtained using optical model phase shifts, the second order effective range approximation Eq.(2.38) with values from Table 2.6, and the first order phase shift$\delta \simeq -a_s k$, as indicated. As expected, the latter approximation is reliable only for extremely small values of the final energy. The second order, effective range parameterization works much better, in particular as the scattering length increases.

p- and d-resonances

Fig. 2.10 shows results obtained considering three different possibilities for the initial state: the s, p and d orbitals. For each initial state a unit spectroscopic factor is assumed. We show the

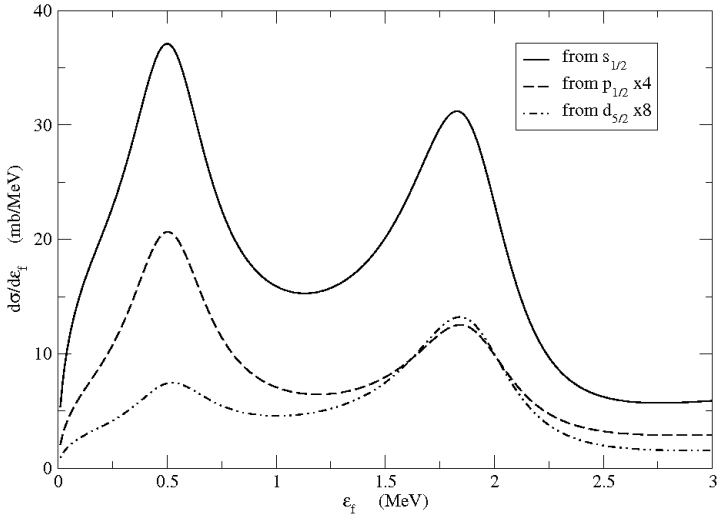

Figure 2.11: Check of the dependence from the initial state angular momentum. Full curve: sum of transitions from s-initial state. Dashed and dotdashed lines: sum of transitions from p and d-initial states respectively. To make them visible these curves have been multiplied by a factor of four and eight respectively.

results of the transition bound to unbound from each initial state to each possible unbound state as indicated. Since there is no information on the location and possible strength of the $d_{3/2}$ resonance we have not attempted to include it. The p and the d-resonance peaks are clearly seen because of the effect of the angular momentum enhancement factor in Eq.(B.8). As indicated some transition strengths have been multiplied by a factor five to make them visible. It is clear from this figure that the dominant components in the neutron knockout spectrum from ^{14}Be and ^{14}B come from the s-wave component in the ground states of those nuclei. Therefore the full curve is the sum of the contributions from the initial s-state alone with unit spectroscopic factor. There can be large peaks due to transitions to the $p_{1/2}$ and $d_{5/2}$ final state, provided they are centered around the energies we have chosen. The results of Fig. 2.11 are shown as a check of the dependence of the transition probability on the initial state angular momentum. The full curve is the sum of transitions from s-initial state. Dashed and dotdashed lines are the sum of transitions from p and d-initial states respectively. Since the transitions from p and d orbitals are negligible, then components in the wave functions of ^{14}Be or ^{14}B with a neutron in such angular momentum states will not play much role in the reaction. Thus it is unlikely that any difference in the neutron breakup spectrum due to different mixtures of these configurations in the two parent nuclei will be seen.

To clarify further the latter point, the sum of all transitions from the s-bound state, is shown again in Fig. 2.12 for two initial binding energies (solid and dashed lines as indicated). Very small changes in the initial binding energy do not give appreciable differences in the final continuum spectra, in particular in the positions of the peaks. They however give differences in the absolute cross section value and in the relative height of the s- and d-state peak. The dotdashed

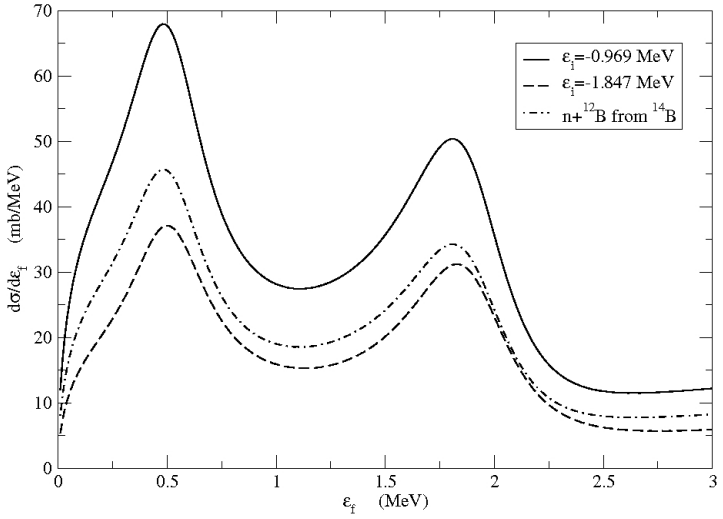

Figure 2.12: Check of the dependence from the initial binding energy of the sum of transitions from s-initial state. Full curve: ε_i= -0.97 MeV as in ^{14}B; dashed curve: ε_i=-1.85 MeV as in ^{14}Be [78]. Dotdashed line: sum of transitions from *s*, *p* and *d*-initial states including spectroscopic factors of 0.66, 0.04 and 0.30 respectively as in ^{14}B [77] with ε_i= -0.97 MeV.

line is the result obtained using the neutron initial binding energy in ^{14}B , which is -0.969 MeV, and summing transitions from s, p and d-initial states including experimental spectroscopic factors [77] of 0.66, 0.04 and 0.30 respectively. According to the simple model for two nucleon breakup presented in Sec. 2.3, the presence of a $1p_{3/2}$ proton in the initial state would give the same contribution to the breakup of each neutron component and therefore the shape of the spectra should not be modified. On the other hand in the case of ^{14}Be the two neutrons are in the same state for each component of the initial wave function. Therefore since the p and d wave functions have less pronounced tails, the last integral of Eq.(2.30), which gives the stripping probability of one of the two neutrons, will naturally diminish the absolute value of the p and d resonances peaks with respect to the final s-state peak.

We notice also that there is a shift between the peaks of the energy spectra and the resonance energies obtained from the phase shifts and given in Table 4. The shift is due to a combined effect of the 1/k factor in Eq.(2.23), of the matching between initial separation energy, peak energy of the resonance and relative beam energy per nucleon and only in a small measure to the presence of the extra phase ν. In the ^{14} Be case it is less noticeable because the initial separation energy is very small. The resonance energy was 1.27 MeV while the peak is at 1.25 MeV. For ^{13}Be the resonance energies are 0.67 MeV (p-state) and 2 MeV (d-state) while the peaks are at 0.5 MeV and 1.8 MeV respectively. One notices that the shift increases increasing the resonance energy.

Therefore two differences might be expected in the experimental energy spectra of ^{13}Be when produced by ^{14}Be rather than ^{14}B projectile fragmentation: a first peak at energy smaller

than 0.5 MeV due to the s-continuum state, and then two more diffuse bumps if the projectile is ^{14}Be; two well definite peaks of not too different strength, one centered at 0.5 MeV due to the $p_{1/2}$ resonance and another around 2 MeV due to the $d_{5/2}$ resonance if the projectile is ^{14}B. Such an hypothesis agrees also with the conclusion of Ref.[17] of a s-state very close to threshold. The three different experiments [10, 17, 83] would therefore be complementary and allow to determine the characteristics of ^{13}Be low energy continuum. To give another example

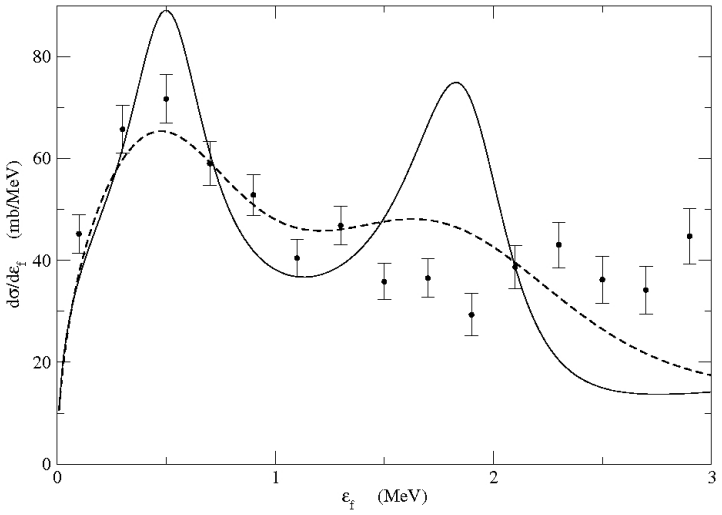

Figure 2.13: Sum of all transitions from the s initial state with ε_f=-1.85 MeV (solid line). Experimental points from H. Simon et al. [83] for the reaction ^{14}Be+^{12}C $\rightarrow$ n+^{12}Be+X at 250 A.MeV. Dashed line is the folding of the calculated spectrum with the experimental resolution curve.

of a possible comparison with available data, we show in Fig. 2.13 the experimental points from H. Simon et al. [83] for the reaction ^{14}Be+^{12}C $\rightarrow$ n+^{12}Be+X at 250 A.MeV. The normalization factor of the data to mb/MeV is 0.843. The solid line gives the sum of all transitions from the s initial state with ε_f=-1.85 MeV (solid line), as in previous figures, renormalized with a factor 2.4. The dashed line is the folding of the calculated spectrum with the experimental resolution curve. Therefore the calculation underestimate the absolute experimental cross section by a factor of 2. In view of the incertitude in the strength of our n-target δ-potential and on the initial state spectroscopic factor which has been taken as unit, we can consider our absolute cross sections quite reasonable.

Finally we wanted to address the issue of possible core excitation effects which in Ref.[76] have been shown to be of fundamental importance for reproducing simultaneously the ^{13}Be and ^{14}Be characteristics. Those effects can be modeled in the present approach by considering a small imaginary part in the neutron-core final optical potential (cf. Eq.(2.35)). This is a standard procedure for continuum states where most often the potential is also energy dependent [13]. A surface potential of Woods-Saxon derivative form has been taken with strengths W_0 equal to -0.5, -1.0 and -1.5 MeV for the d-state only. The results are shown in Fig. 2.14. The effect of

the imaginary potential is to wash out the d-resonance peak. Several structure models predict indeed the $d_{5/2}$ resonance coupled to an excited ^{12}Be core. We have found the same smoothing off effect if the s-state is calculated including an imaginary potential. It seems therefore that the spectrum of unbound nuclei could partially reflect the structure of the bound parent nucleus and that reaction mechanism models used to extract structure information should carefully include the effects discussed above. The model presented here seems to be quite promising in this respect.

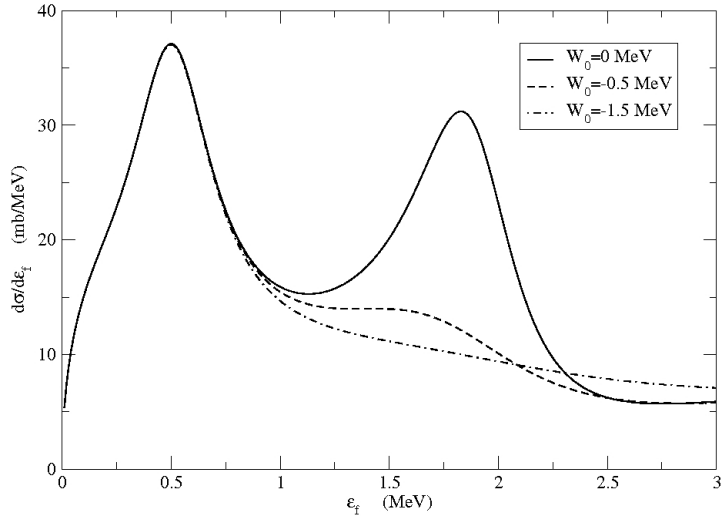

Figure 2.14: Sum of all transitions from the s initial state with ε_f=-1.85 MeV including core excitation via an imaginary part of the optical potential for the d-resonance only.

2.6 Application: The reaction ^{11}Li $\rightarrow$ ^{10}Li+n

2.6.1 One neutron average potential

In this section, we apply the fragmentation model to the study of the relative energy spectrum n+^{9}Li obtained by the authors of Ref. [84] in the breakup reaction of ^{11}Li on ^{12}C at 264 A.MeV. The structure of ^{11}Li is already well known from a number of experiments and theoretical works [84]-[44]: the two neutron separation energy is 0.3$\pm$0.27 MeV [78]; the wave function is combination of a 2s state with a spectroscopic factor 0.31, a $p_{1/2}$ with spectroscopic factor 0.45 [85] and there is also a small $d_{5/2}$ component. The main $d_{5/2}$ strength is in the continuum centered around 1.55 MeV [84].

In this section, the initial wave function for the *s*-state is calculated in a Woods-Saxon potential with R= $r_0 A^{1/3}$ as before and strength fitted to the separation energy 0.3 MeV[78] and has

the parameters given in Table 2.7.

Table 2.7: Asymptotic normalization constants C_i ($fm^{-1/2}$) for the initial state components wave functions of the bound neutron. Spectroscopic factors from Ref. [85]. Potential parameters are: V_0 fitted to give the separation energy 0.3 MeV [78]. The other potential parameters are r_0=1.27 fm, a=0.75 fm, V_{so}=5.25 MeV.

ε_i		-0.3 MeV	
l_i,	j_i	$C_i(fm^{-1/2})$	C^2S
0	1/2	0.76	0.31
1	1/2	0.24	0.45

Table 2.8: Woods-Saxon and spin-orbit potential parameters for the continuum final states of the system n + ^{9}Li.

V_0 (MeV)	r_0 (fm)	a (fm)	V_{so} (MeV)	a_{so} (fm)
-39.8	1.27	0.75	7.07	0.75

To describe the valence neutron in the ^{10}Li continuum we assume that the single neutron Hamiltonian with respect to ^{9}Li has the form already given in Sec. 2.3.5. The imaginary part of the final potential is taken equal to zero. The Woods-Saxon potential plus spin-orbit whose parameters are given in Table 2.8.

The continuum energies can be adjusted by varying the parameter α in the potential, see Eq.(2.37). As possible final states we have considered only the s, p and d partial waves calculated in the potential of Table 2.8 plus Eq.(2.37), according to Ref. [53], with different values of the strength α. Table 2.9 gives the energies and widths of the $1p_{1/2}$ and $1d_{5/2}$ states and the corresponding values of α. The widths are obtained from the phase shift variation near resonance energy, according to $d\delta_j/d\varepsilon_f|_{\varepsilon_{res}} = 2/\Gamma_j$, once that the resonance energy is fixed [47]. Notice that the values of α for the s and d states are very similar, therefore these two states are basically obtained in the same potential.

The delta-interaction strength used in Eq. (2.6), is v_2=-8625 MeV fm^3 again since also in this case the target was ^{12}C.

2.6.2 Results

We consider the knockout of a single neutron from a bound state in a potential, similarly to the previous calculation for ^{11}Be, ^{14}Be and ^{14}B. The reaction corresponds to a neutron initially

Table 2.9: Scattering length of the 2s continuum state, energies and widths of the p- and d-resonances in ^{10}Li and corresponding strength parameters for the δV potential.

	ε_{res} MeV	Γ_j MeV	a_s fm^{-1}	α MeV
$2s_{1/2}$			-17.2	-10.0
$1p_{1/2}$	0.63	0.35		3.3
$1d_{5/2}$	1.55	0.18		-9.8

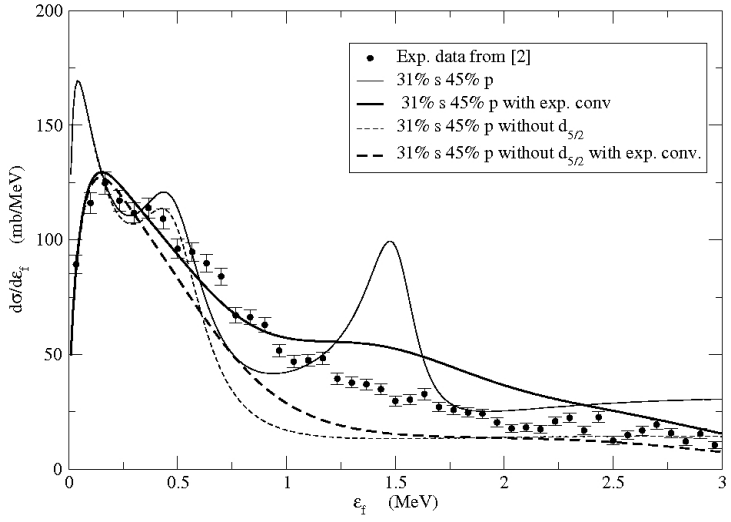

Figure 2.15: n-^{9}Li relative energy spectrum, for the reaction ^{11}Li+^{12}C $\rightarrow$ n+^{9}Li+X at 264 A.MeV. Only the contributions from an s and p initial state with experimental spectroscopic factors [85] C^2S= 0.31 and 0.45 respectively are included. The thin solid curve is the total calculated result. The thick solid curve curve is after convolution with the experimental resolution function. The thin dashed curve is the calculation without the d-resonance while the thick dashed curve is the same calculation after convolution. The symbols with error bars are the experimental points from [84]. Calculations are normalized to the data.

bound in ^{11}Li which is then excited into an unbound state of ^{10}Li, assuming that another nucleon has been emitted and stripped by the target, thus not detected in coincidence with the core.

In Fig. 2.15, the symbols with error bars are the experimental points from [84]. The thin full curve is the calculated total spectrum, sum of the contributions from the s and p components of the initial wave function, with the parameters of Table 2.7 and the experimental spectroscopic factors from Ref. [85]. Using the theoretical spectroscopic factors from Refs. [70], [53] gives very small differences in the shape of the total spectrum which however become unnoticeable after convolution with the experimental resolution function. The s, p and d final continuum

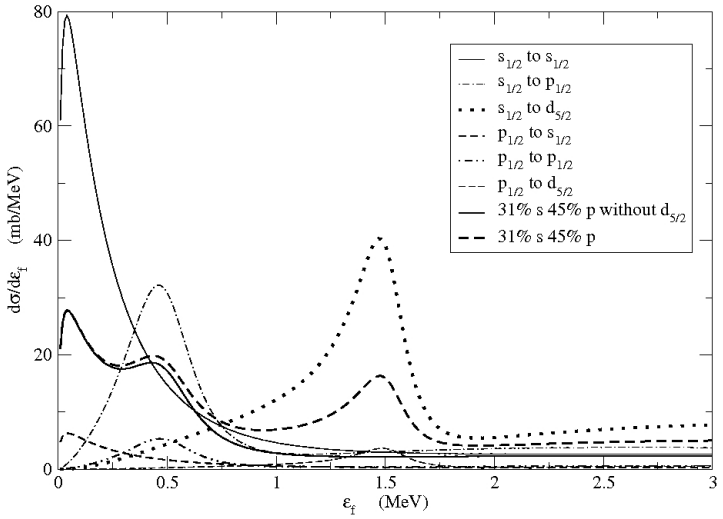

Figure 2.16: The individual transitions, bound to unbound from the s and p initial state components, taken with unit spectroscopic factors, to the s,p and d unbound state as indicated. The thick dashed line is the sum of all transitions, including the spectroscopic factors for the initial state components while the thick solid line is does not include transitions to the d-resonance.

states have the parameters of Table 2.9. Notice that these parameters are perfectly consistent with those extracted from the data and given by Table 4 of Ref. [84]. The thick solid curve is the same calculation after convolution with the experimental resolution function. The dashed curve is the calculation without the d-resonance after convolution while the thin dashed curve is the bare calculation without the d-resonance contribution. The agreement between the thick solid curve and the data is quite good and it shows the importance of including the d-resonance to reproduce the tail of the experimental spectrum. The Coulomb breakup spectrum from the s component of the initial state was also calculated but since it gives a contribution of less than 5% to the peak of the spectrum, it has been omitted from the figures.

The individual transitions, bound to unbound from each initial state component to each possible unbound state as indicated, are shown in Fig. 2.16. We give also in Fig. 2.17 the comparison for the s to s transition of our calculation with the calculation according to the sudden formula Eq.(20) of [45]. Both calculations were done with the *exact* phase shift, obtained by solving numerically the Schrödinger equation with the potential given by Eqs.(2.37). Contrary to what it was found for ^{13}Be, we find here that in the case of the ^{10}Li virtual state, the scattering length is large enough, i.e. the state is close enough to threshold, to justify the use of the sudden approximation. Furthermore we have checked that the effective range formula gives in this case a very good fit to the exact phase shift. In fact, using it in Eq.(20) of [45] gives a curve almost indistinguishable from the dashed line in Fig. 2.17. The parameters obtained from the fit are: a_s=-14.8 fm, r_e= 7.5 fm. Notice that the scattering length value obtained instead as a_s=-

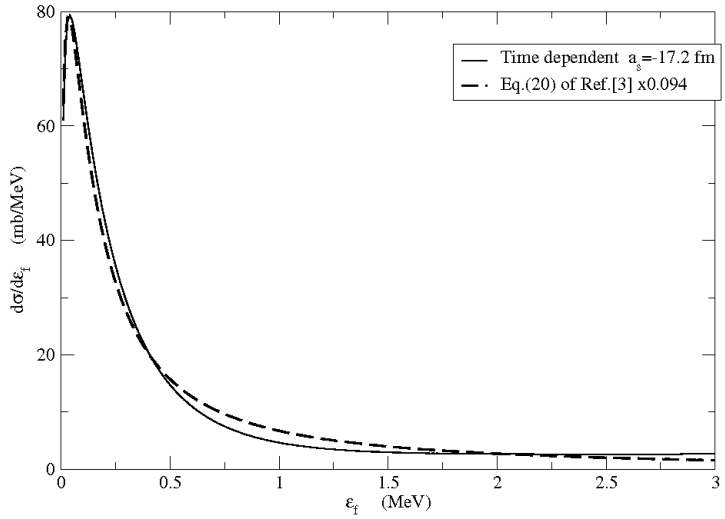

Figure 2.17: Comparison for the s to s transition of our calculation (solid curve) with that according to the sudden formula Eq. (20) of [45]. Both calculations use the *exact* phase shifts.

$\lim_{k\to 0} \frac{\delta_0}{k}$ and given in Table 2.9 was -17.2 fm. This is the kind of sensitivity one can find using the two different prescriptions for a_s. On the other hand we have checked that the value of r_e from the fit, is consistent with the behaviour of our continuum state potential, Eqs. (2.37). Such potential becomes indeed negligible, and consistent with zero, for $r > r_e = 7.5$ fm, as prescribed for the applicability of the effective range theory.

As already found for ^{11}Be and ^{13}Be, we can confirm here with the ^{10}Li example that, a part for the s to s transition, the excitation of resonances with $l > 0$ in the continuum of unbound nuclei in projectile fragmentation reactions, is a final state effect due to n-core interaction, rather than a process in which a bound component of the initial wave function becomes suddenly unbound. The results in Fig. 2.16 show clearly that the population of continuum resonance is dominated by the contributions from the s-initial state, while the transitions p to p or p to d are not large enough to explain the experimental spectrum. This is particularly clear for the d-resonance whose presence is necessary to explain the experimental spectrum tail but whose strength could not be justified by a d to d transition which would have a very small amplitude. Therefore the strength of the continuum resonances of a daughter nucleus does not reflect directly the occupation of the bound states of same angular momentum in the mother nucleus. This is different from the *common wisdom* on the breakup of two-neutron halo nuclei, as discussed for example in the recent Ref. [86].

In the case of ^{11}Li the two neutrons are in the same state for each component of the initial wave function. Therefore since the p and d wave functions have less pronounced tails, the stripping probability of one of the two neutrons will naturally diminish the absolute value of

the peaks due to transitions from these states, with respect to peaks due to transition from the bound s-component. This effect is not taken into account at the moment in our numerical implementations of the model. On the other hand our absolute cross sections should be multiplied by a factor two to take into account the fact that the experimental data do not distinguish the two neutrons in the continuum. The absolute value of our cross section can be read from the dashed curve in Fig. 2.16. Taking into account the factor two just mentioned, we see that in order to compare to the experimental data in Fig. 2.15, which are given on their absolute scale, we still have to renormalize our calculations by a factor two. Considering the incertitude in the value of the neutron-target delta-interaction potential and in the strong absorption radius, we can consider our estimates quite reasonable.

The initial state spectroscopic factors in ^{11}Li are quite well known experimentally, therefore the absolute values of our cross sections have also been checked, besides the shape of the n-core relative energy spectrum. Due to the closeness to threshold of the s virtual state we have seen that the sudden formula used in Ref. [45] and the effective range approximation to the phase shift, are both very well justified for ^{10}Li, contrary to what it was previously found for ^{13}Be. Finally we have found that, in agreement with the interpretation given by the authors of [84], their recent data provide a clear evidence on the excitation of a d resonance around 1.5 MeV. Such a resonance does not play much role in the composition of the ^{11}Li ground state but it is an important building bloc of its excited states.

2.7 Note on the convolution

One important aspect in the comparison between experimental spectra and theoretical results is the convolution of our calculation with the the experimental resolution. This convolution is different from one experiment setting to an other. In Sec. 2.4 we discussed this problem in relation to the ^{11}Be$\rightarrow^{10}$Be$+n$ fragmentation data. In that case the experimental resolution function Eq.(2.31) has been published in [54, 65]. In the case of the ^{13}Be spectrum we provided our results to the GSI group (Prof. Chulkov) which made the experiment on ^{14}Be [84]. To perform this calculation, results until a relative energy of 5-6 MeV was required. We decide to neglect the continuum structure for energy higher than 3 MeV, so our calculation was extrapolate at higher energy by a straight line. This approximation is justified because one of cross section term is going to zero very fast as the relative energy is increasing. This convolution has the effect to smooth the results. With this reaction model, this first bump around 0.5 MeV is associated to the $p_{1/2}$ state and the *s*-state. The *s*-state is the ground state of ^{13}Be, but is less populated by the reaction mechanism than the $p_{1/2}$ state and the $d_{5/2}$ state. The same procedure has been followed in the preparation of Fig. 2.15 for n+^{9}Li.

2.8 Conclusion

In this chapter, we have presented a model to study one neutron excitations from a bound initial state to an unbound resonant state in the neutron-core low energy continuum. This is the process by which unbound nuclei are created and studied via projectile fragmentation experiments [10]-[41, 83].

The model is based on a time dependent perturbation theory amplitude and the final state is described by an optical model S-matrix. It can be considered an evolution with respects to sudden and/or R-matrix theory models. The advantages are that the model can be applied to fragmentation from deeply bound states and to resonant and non resonant, large energy, continuum final states. Also core excitation effects can be modeled by an imaginary part of the neutron-core optical potential.

A related approach has been developed in the first chapter and applied to the treatment of transfer to the continuum in which, following the interaction between two passing-by nuclei, a neutron from one of them goes from a bound to an unbound state with final state interaction with the other nucleus. Comparison of the present formalism to the transfer to the continuum model shows that in principle projectile fragmentation does not reflect directly the properties of the neutron-core resonances because the reaction mechanism induces an extra phase with respect to the free particle neutron-core phase shift. It means that the measurements would probe an off-the-energy-shell S-Matrix. The distortion effects seem however small and negligible for the cases discussed in this work.

One neutron breakup can be studied in this way but also one step of two neutron breakup of a borromean nucleus. In this chapter we have presented some applications to both cases to study the properties of ^{11}Be continuum and of the unbound nuclei ^{13}Be and ^{10}Li. Our results are in agreement with the conclusions of Ref.[54, 65] for ^{11}Be. Due to the structure inputs we use, in particular the position of the $p_{1/2}$ resonance, the ^{13}Be continuum spectrum obtained from fragmentation of ^{14}B or ^{14}Be shows essentially the effect of the continuum p and d-resonances. The s-state although present in the calculations almost disappears inside the tail of the p-state but it would still determine the ground state spin and parity of ^{13}Be. Obviously we cannot be conclusive on the structure of ^{13}Be because at the moment we have not attempted to fit experimental data but simply to develop a good reaction model. A better structure study is done in the next chapter. Furthermore our structure inputs, although reasonable, are extremely simple compared to the complexity of the nucleus under study. However preliminary comparisons seem to indicate the reliability of our model. As for ^{11}Li, its initial state spectroscopic factors are quite well known experimentally, therefore the absolute values of our cross sections have also been checked, besides the shape of the n-core relative energy spectrum. Due to the closeness to threshold of the s virtual state we have seen that the sudden formula used in Ref. [45] and the effective range approximation to the phase shift, are both very well justified for ^{10}Li, contrary

to what it was previously found for ^{13}Be. Finally we have found that, in agreement with the interpretation given by the authors of [84], their recent data provide a clear evidence on the excitation of a d resonance around 1.5 MeV. Such a resonance does not play much role in the composition of the ^{11}Li ground state but it is an important building bloc of its excited states.

We have also shown that the excitation energy spectra of an unbound nucleus might reflect the structure of the parent nucleus from whose fragmentation they are obtained. In particular, in the case of ^{14}Be fragmentation, the initial state spectroscopic factors are not known experimentally, and the information from structure calculations indicate an important configuration mixing with components coupled to an excited ^{12}Be core. Thus the analysis of such spectra is expected to be even more complicated. However from the point of view of reaction theory, the results obtained here seem promising and we hope to use such a procedure to implement a fit of experimental data on unbound nuclei.

Chapter 3

Particle-Particle RPA

3.1 Purpose

Up to this point we have discussed only direct reaction models applied to the study of properties of halo nuclei. One of the limitation of the representation of these processes, is the description of the halo nuclei. Indeed for the initial wave function, we use an asymptotic state determined in a Woods-Saxon potential fitted to obtain the correct separation energy of the last neutron. The second neutron of the halo is not taken into account. In our previous fragmentation calculation, the scarce knowledge of the initial wave-function limits the interpretation of the results to the final state interaction for which we can deduce some characteritics by comparing the experimental data to the theoretical calculations. However, our understanding of the initial state will be only partial because the neutron-neutron interaction is not taken into account explicitly by the reaction model. In this chapter, we wish to present some new results on the structure of halo nuclei. This work has been done in collaboration with Nicole Vinh Mau of the IPN Orsay. We used the formalism developed in Ref. [71] as a starting point for new implementations.

The description of nuclei such that ^{11}Li, ^{12}Be or ^{14}C assumed to be formed of a core in its ground state and two extra neutrons is complicated by the fact that the core cannot be considered as a closed shell system. The two-body correlations in the core are very important and a simple two-neutron pairing model is not well adapted. It has been used and it is still used to describe these nuclei but it necessitates a renormalization of the effective neutron-neutron interaction. A model which takes into account two-body correlations in the core is the two-nucleon RPA model. It has been shown to be able to reproduce very well the properties of nuclei such as ^{11}Li, ^{12}Be or ^{14}C for example without any fitting of the effective interaction. It is particularly well adapted to the case of ^{14}Be, not yet completely understood, where we know that the ground

state wave function of ^{12}Be is an admixture of different configurations.

While particle-hole RPA has been extensively used since some fifty years, the two-nucleon RPA is very rarely used in nuclear physics. Perhaps this is due to the fact that the diagonalization of the two-nucleon RPA matrix, apart the energies of the systems, gives only two-nucleon amplitudes between the core correlated ground state and a given state of the systems described as the core plus or minus two nucleons. Then to study the properties of these three-body systems we have to find how they can be derived from the knowledge of two-body RPA amplitudes. Particularly interesting are the effects of RPA on the core ground state, single nucleon occupation number and correction to the binding energy, the properties of the A+2 system, its radius and the transition probability between the ground state and an excited state for example. We propose a number of methods to get such relations and give general expressions which can be applied to specific cases.

The first part of this chapter is devoted to the presentation of the theoretical formalism. We make a brief survey of the two-nucleon RPA model and introduce our notations. Then, we derive the expressions of the wave function, binding energy and single particle occupation numbers for the core nucleus with A nucleons. The final section of this theoretical part is devoted to the properties of the nuclei with A+2 or A-2 nucleons, such as wave functions, transition probabilities, radius.

The goal of the next section is to proceed to some structure calculation on a range of Beryllium isotopes going from ^{8}Be to ^{14}Be within the particle-particle (p-p) RPA formalism. This is a three-body model that takes into account the correlations in the core. Thus these nuclei are modelized as a core surrounded by two neutrons (^{12}Be=^{10}Be + 2 neutrons and ^{14}Be=^{12}Be+2 neutrons) or a core minus two neutrons (^{8}Be=^{10}Be - 2 neutrons and ^{10}Be=^{12}Be - 2 neutrons). A great interest of this particle-particle RPA is to give information about the core + 2 neutrons system and the core - 2 neutrons system, within the same calculation. It means that the results for these two systems cannot be adjusted separately which makes an important constraint when they are compared to experimental data. We wish to have a general understanding of these Beryllium isotopes by studying them within the same method. In practice, we proceed to the calculation with a ^{10}Be core and with a ^{12}Be core. We obtain in two ways the results for the ^{12}Be nucleus, once from the ^{10}Be + 2 neutrons calculation and once from the ^{12}Be - 2 neutrons calculation. Of course we expect to find the same results in both cases, which represents an even greater constraint. First, we proceed to the calculation with a ^{10}Be core. There one needs the experimentally known ^{11}Be spectrum as an input. Then we compare the results obtained for ^{8}Be and ^{12}Be to the available experimental data. In the case of a ^{12}Be core, we 'tune' the ^{13}Be structure to find the good two-neutron separation energy for ^{14}Be, and get some constraints on ^{13}Be which is not well understood. We then look at the ^{13}Be spectrum to see wether it corresponds to the one observed experimentally. Of course, this procedure gives us only the position in energy of the resonances of the ^{13}Be. A new reaction calculation, taking into account the

two neutrons explicitly, would be needed to evaluate the relative strength of these resonances, as they are observed experimentally.
First, we look at the formalism of the particle-particle RPA. In order to calculate different observables (rms, B(E1), B(E2)...), we determine the matrix elements of one- and two-body operators between RPA states; all formulae are given explicitly. The formalism is applied to a range of Beryllium isotopes. The 0^+, 1^- and 2^+ states are calculated and compared quite successfully to the experimental results.
We determine also the RPA wave function of ^{14}Be in terms of (2n+2) particles - (2n) holes configurations.

3.2 A brief survey of the two-nucleon RPA model

The two-nucleon RPA model concerns nuclei which can be described as a core plus or minus two nucleons. Similarly to the particle-hole RPA equations, the two-nucleon RPA equations can be derived by several methods. One of them, the Green's functions method relies on the expansion of the two-particle Green's function in terms of upwards and backwards ladder diagrams as shown in Fig 3.1 and it corresponds to introducing in the core ground state contributions of configurations with 2n particles and 2n holes. In this section we remind briefly the model and

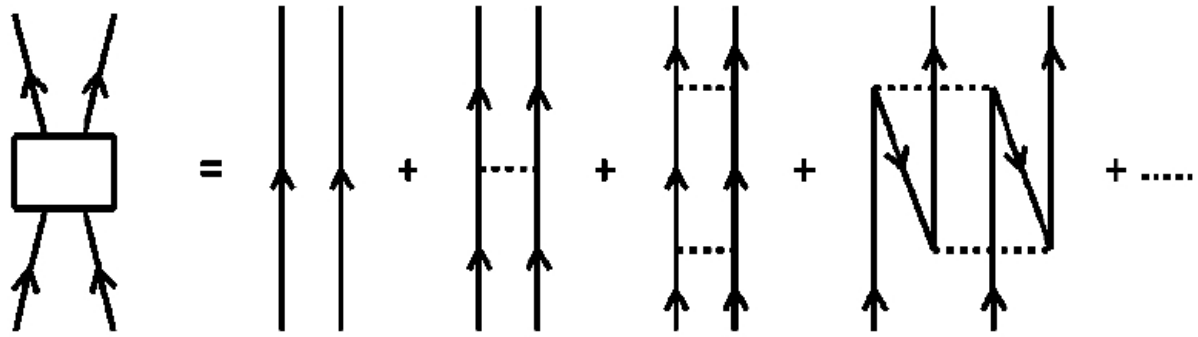

Figure 3.1: RPA diagrammatic expansion of the two-particle Green's function.

introduce our notations.
The single nucleon states are referred as a,b... (Latin letters) or α, β... (Greek letters) when the nucleon is in unoccupied or occupied Hartree-Fock states respectively.
We introduce pair operators A^+ such that

$$A^\dagger_{ab}(J,M_J) = \sum_{m_a,m_b} (j_a,j_b,m_a,m_b|J,M_J)a^\dagger_a a^\dagger_b \quad with \;\; a<b \tag{3.1}$$

$$A^\dagger_{\alpha\beta}(J,M_J) = \sum_{m_\alpha,m_\beta} (j_\alpha,j_\beta,m_\alpha,m_\beta|J,M_J)a^\dagger_\alpha a^\dagger_\beta \quad with \;\; \alpha<\beta \tag{3.2}$$

In the following to simplify the formalism we do not specify the total angular momentum (J,M$_J$) in the pair operators, except when necessary. We define two-nucleon amplitudes for the nuclei with A+2 (N states) and A-2 (M states) nucleons defined as:

$$X^{(N)}_{mn} = \langle A+2,N|A^{\dagger}_{mn}|A,\tilde{0}\rangle \quad m<n \tag{3.3}$$
$$X^{(N)}_{\mu\nu} = \langle A+2,N|A^{\dagger}_{\mu\nu}|A,\tilde{0}\rangle \quad \mu<\nu \tag{3.4}$$
$$Y^{(M)}_{mn} = \langle A-2,M|A_{mn}|A,\tilde{0}\rangle \quad m<n \tag{3.5}$$
$$Y^{(M)}_{\mu\nu} = \langle A-2,M|A_{\mu\nu}|A,\tilde{0}\rangle \quad \mu<\nu, \tag{3.6}$$

where $|A,\tilde{0}\rangle$ is the correlated RPA wave function of the core ground state and $|A+2,N\rangle$ and $|A-2,M\rangle$ the RPA wave functions of A+2 and A-2 nuclei respectively. Again we have omitted for simplicity the angular momentum (J,M$_J$) in both pair operators and wave functions.
The RPA equations read as:

$$(\Omega-[\varepsilon_a+\varepsilon_b])x_{ab}-\sum_{kl}\langle kl|V_{nn}|ab\rangle x_{kl}-\sum_{\kappa\lambda}\langle\kappa\lambda|V_{nn}|ab\rangle x_{\kappa\lambda} = 0, \tag{3.7}$$
$$(\Omega-[\varepsilon_\alpha+\varepsilon_\beta])x_{\alpha\beta}+\sum_{kl}\langle kl|V_{nn}|\alpha\beta\rangle x_{kl}+\sum_{\kappa\lambda}\langle\kappa\lambda|V_{nn}|\alpha\beta\rangle x_{\kappa\lambda} = 0. \tag{3.8}$$

The energies ε are the unperturbed single nucleon energies. The two-body matrix elements of V_{nn}, the effective nucleon-nucleon interaction, have to be antisymmetrized.
If we take N_0 configurations $(a,b),...$ and M_0 configurations $(\alpha,\beta),...$, the RPA equations (3.7) and (3.8) have N_0+M_0 solutions. N_0 solutions correspond to the states N of the A+2 nucleus with:

$$E_N(A+2)-E_0(A)=\Omega_N, \tag{3.9}$$
$$X^{(N)}_{ab}=x^{(N)}_{ab},\ X^{(N)}_{\alpha\beta}=x^{(N)}_{\alpha\beta}. \tag{3.10}$$

The other M_0 solutions correspond to the states M of the A-2 nucleus with:

$$E_M(A-2)-E_0(A)=-\Omega_M, \tag{3.11}$$
$$Y^{(M)}_{ab}=x^{(M)}_{ab},\ Y^{(M)}_{\alpha\beta}=x^{(M)}_{\alpha\beta}. \tag{3.12}$$

with the orthonormalization and closure relations:

$$\sum_{ab}X^{(N)}_{ab}X^{(N')}_{ab}-\sum_{\alpha\beta}X^{(N)}_{\alpha\beta}X^{(N')}_{\alpha\beta} = \delta_{NN'} \tag{3.13}$$
$$\sum_{ab}Y^{(M)}_{ab}Y^{(M')}_{ab}-\sum_{\alpha\beta}Y^{(M)}_{\alpha\beta}Y^{(M')}_{\alpha\beta} = -\delta_{MM'} \tag{3.14}$$
$$\sum_{N}X^{(N)}_{\alpha\beta}X^{(N)}_{\kappa\lambda}-\sum_{M}Y^{(M)}_{\alpha\beta}Y^{(M)}_{\kappa\lambda} = -\delta_{\alpha\beta,\kappa\lambda} \tag{3.15}$$
$$\sum_{N}X^{(N)}_{ab}X^{(N)}_{kl}-\sum_{M}Y^{(M)}_{ab}Y^{(M)}_{kl} = \delta_{ab,kl}. \tag{3.16}$$

We see from Eqs.(3.9) and (3.11) that the lowest eigenvalues among the N and M solutions are directly related to the two-neutron separation energy in the $A+2$ and A nuclei. We define two pairing operators, $Q_N^\dagger$ and $Q_M^\dagger$, such that:

$$\begin{aligned} |A+2,N\rangle &= Q_N^\dagger |A,\tilde{0}\rangle & (3.17)\\ Q_N|A,\tilde{0}\rangle &= 0 & (3.18)\\ |A-2,M\rangle &= Q_M^\dagger |A,\tilde{0}\rangle & (3.19)\\ Q_M|A,\tilde{0}\rangle &= 0. & (3.20) \end{aligned}$$

To find a relation between the operators Q and A we assume that the commutators of the $A^\dagger$ and A operators are approximated by their value on the uncorrelated core wave function (quasi boson approximation). This means that:

$$[A_{kl}, A_{mn}^\dagger] = \delta_{kl,mn} \tag{3.21}$$

$$[A_{\kappa\lambda}, A_{\mu\nu}^\dagger] = -\delta_{\kappa\lambda,\mu\nu}. \tag{3.22}$$

The orthonormalization of the wave functions of A+2 and A-2 nuclei, Eqs.(3.17) and (3.19), using the commutators of Eqs.(3.21) and (3.22), leads to the following relations:

$$\begin{aligned} Q_N^\dagger &= \sum_{kl} X_{kl}^{(N)} A_{kl}^\dagger - \sum_{\kappa\lambda} X_{\kappa\lambda}^{(N)} A_{\kappa\lambda}^\dagger & (3.23)\\ Q_M^\dagger &= \sum_{\kappa\lambda} Y_{\kappa\lambda}^{(M)} A_{\kappa\lambda} - \sum_{kl} Y_{kl}^{(M)} A_{kl}. & (3.24) \end{aligned}$$

From these relations it is easy to show that the pairing operators obey to the following commutation relations:

$$[Q_N, Q_{N'}^\dagger] \approx \delta_{N,N'} \tag{3.25}$$

$$[Q_M, Q_{M'}^\dagger] \approx \delta_{M,M'}. \tag{3.26}$$

All other commutators between two operators $Q^\dagger$ and Q are equal to zero. In the following we shall use the inverse of Eqs.(3.23) and (3.24), namely:

$$\begin{aligned} A_{kl}^\dagger &= \sum_N X_{kl}^{(N)} Q_N^\dagger + \sum Y_{kl}^{(M)} Q_M & (3.27)\\ A_{\kappa\lambda}^\dagger &= \sum_N X_{\kappa\lambda}^{(N)} Q_N^\dagger + \sum_M Y_{\kappa\lambda}^{(M)} Q_M & (3.28) \end{aligned}$$

3.3 Properties of the core nucleus

3.3.1 The correlated core wave function

Following the same method as Sanderson [114] and Rowe [115] for the particle-hole RPA we may write the correlated core wave function as:

$$|A,\tilde{0}\rangle = N_0 e^S |0\rangle \tag{3.29}$$

where $|0\rangle$ is the uncorrelated wave function, N_0 a normalization factor and S is given by:

$$S = \sum_{lm\lambda\mu JM_J} c_{lm,\lambda\mu}(J,M_J) A^\dagger_{lm}(J,M_J) A_{\lambda\mu}(J,M_J). \tag{3.30}$$

Expanding the exponential in Eq.(3.29) gives the core wave function as a mixture of 0p-0h, 2p-2h,4p-4h... configurations. The coefficients c are determined by using the property that the operators Q_N and Q_M should satisfy Eqs.(3.18) and (3.20) respectively. Replacing them by their expressions (3.23), (3.24) and the correlated wave function by its expression (3.29) leads to two equations:

$$X^{(N)}_{\lambda\mu}(J) = \sum_{lm} c_{lm,\lambda\mu}(J) X^{(N)}_{lm}(J) \tag{3.31}$$

$$Y^{(M)}_{lm}(J) = \sum_{\lambda\mu} c_{lm,\lambda\mu}(J) Y^{(M)}_{\lambda\mu}(J). \tag{3.32}$$

The amplitudes X being independent of M_J, the coefficients c have the same property and for simplicity we have suppressed this variable in all our equations. Eqs.(3.31) and (3.32) can be transformed in a more convenient form. Following da Providencia [116], we use the closure relations between amplitudes for N and M states and write Eq.(3.31) as:

$$\begin{aligned} X^{(N)}_{\alpha\beta}(J) &= \sum_{N'} X^{(N')}_{\alpha\beta}(J)\delta_{NN'} \\ &= \sum_{N'} X^{(N')}_{\alpha\beta}(J) \left(\sum_{lm} X^{(N)}_{lm} X^{(N')}_{lm} - \sum_{\lambda\mu} X^{(N)}_{\lambda\mu} X^{(N')}_{\lambda\mu} \right) \qquad (3.33) \\ &= \sum_{lm} c_{lm,\alpha\beta} X^{(N)}_{lm} \qquad (3.34) \end{aligned}$$

From the equality between the expressions of the second and third lines and by using again Eq.(3.31) for $X^{(N)}_{\lambda\mu}$, one gets a new equation:

$$c_{lm,\lambda\mu}(J) = \sum_N X^{(N)}_{lm} X^{(N)}_{\lambda\mu} - \sum_{N,\alpha\beta} c_{lm,\alpha\beta} X^{(N)}_{\lambda\mu} X^{(N)}_{\alpha\beta} \tag{3.35}$$

which can be solved by iteration. From Eq.(3.32), the same derivation leads to:

$$c_{lm,\lambda\mu}(J) = \sum_M Y^{(M)}_{lm} Y^{(M)}_{\lambda\mu} - \sum_{M,ab} c_{ab,\lambda\mu}(J) Y^{(M)}_{ab} Y^{(M)}_{lm}. \tag{3.36}$$

Using the closure relations again, we can check that the two equations are equivalent. We remark that only states N or M which have large enough "small" RPA components will contribute to the sums.

The normalization factor N_0 should be such that:

$$\langle A,\tilde{0}|A,\tilde{0}\rangle = N_0^2 \langle 0|e^{S^\dagger} e^S|0\rangle = 1, \tag{3.37}$$

with S given by Eq.(3.30). If the ground state correlations are not too large, we may expand the exponentials and write:

$$\langle 0|e^{S^\dagger} e^S|0\rangle = \langle 0|(1+S^\dagger + \frac{1}{2!}S^{\dagger 2} + ...)(1+S+\frac{1}{2!}S^2+...)|0\rangle, \tag{3.38}$$

using the following relations:

$$\begin{aligned} S^\dagger|0\rangle &= 0 && (3.39)\\ \langle 0|S^\dagger S|0\rangle &= \langle 0|\left[S^\dagger, S\right]|0\rangle \\ &= \sum_{lm\lambda\mu} |c_{lm,\lambda\mu}|^2 && (3.40) \end{aligned}$$

we can show that:

$$\langle 0|e^{S^\dagger} e^S|0\rangle \simeq 1 + \sum_{lm,\lambda\mu} |c_{lm,\lambda\mu}|^2 + \frac{1}{2!}\left(\sum_{lm,\lambda\mu} |c_{lm,\lambda\mu}|^2\right)^2 + \frac{1}{3!}\left(\sum_{lm,\lambda\mu} |c_{lm,\lambda\mu}|^2\right)^3 + ... \tag{3.41}$$

which are the first terms of the expansion of an exponential so that the normalization factor might be written as:

$$N_0^2 \simeq exp\left\{ - \sum_{lm\lambda\mu JM} |c_{lm,\lambda\mu}(J)|^2 \right\}. \tag{3.42}$$

3.3.2 Single nucleon occupation numbers

The two-body correlations introduced by the RPA model in the core wave function induce modifications of the Hartree-Fock nucleon occupation numbers in the core. Using the wave function of Eq.(3.29), it is easy to calculate f_a and f_α, the nucleon occupation numbers for

unoccupied (a) and occupied (α) states in the HF core. By definition the occupation number is given for any state i by:

$$f_i = \langle A,\tilde{0}|a_i^\dagger a_i|A,\tilde{0}\rangle, \tag{3.43}$$

which, with the help of Eq.(3.29), can be written as:

$$f_i = N_0\langle A,\tilde{0}|a_i^\dagger a_i e^S|0\rangle, \tag{3.44}$$

using the exact relation between any two operators O and S:

$$Oe^S = e^S\left\{O+[O,S]+\frac{1}{2!}[[O,S],S]+...\right\}, \tag{3.45}$$

leads to

$$f_i = N_0\langle A,\tilde{0}|e^S\left\{a_i^\dagger a_i+\left[a_i^\dagger a_i,S\right]+...\right\}|0\rangle, \tag{3.46}$$

where the commutators can be evaluated as:

$$\left[a_a^\dagger a_a,S\right] = \sum_{\alpha\beta b,JM_J} c_{ab,\alpha\beta}A_{ab}^\dagger A_{\alpha\beta} \tag{3.47}$$

$$\left[a_\alpha^\dagger a_\alpha,S\right] = -\sum_{ab\beta,JM_J} c_{ab,\alpha\beta}A_{\alpha\beta}A_{ab}^\dagger. \tag{3.48}$$

Because of the commutation relations satisfied by the operators A and $A^\dagger$, all further terms in Eq.(3.46) are zero such that:

$$e^S\left[a_i^\dagger a_i,S\right] = \left[a_i^\dagger a_i,S\right]e^S, \tag{3.49}$$

which leads to the following expressions

$$f_\alpha = 1-\sum_{ab\beta,JM_JN} c_{ab,\alpha\beta}X_{ab}^{(N)}X_{\alpha\beta}^{(N)}, \tag{3.50}$$

which, using Eq.(3.31) reads:

$$f_\alpha = 1-\sum_{\beta,NJM_J}|X_{\alpha\beta}^{(N)}|^2. \tag{3.51}$$

In the same way we can show that:

$$f_a = \sum_{b,MJM_J}|Y_{ab}^{(M)}|^2. \tag{3.52}$$

We may check that the total number of nucleons is conserved. Indeed, the modification of the particle number will be

$$\delta N = \sum_{M,ab}|Y_{ab}^{(M)}|^2-\sum_{N\alpha\beta}|X_{\alpha\beta}^{(N)}|^2, \tag{3.53}$$

finally using the closure relation between the amplitudes N and M, we get:

$$\begin{aligned}\delta N &= \sum_{ab}\left(-1+\sum_{N}|X^{(N)}_{ab}|^2\right)-\sum_{N,\alpha\beta}|X^{(N)}_{\alpha\beta}|^2 \\ &= -\sum_{ab}1+\sum_{N}1 \qquad (3.54)\\ &= 0, \qquad (3.55)\end{aligned}$$

since the number N of RPA states is equal to the number of particle-particle configurations.

3.3.3 The binding energy of the core nucleus

The total binding energy of the core is given by:

$$E_0 = \langle A,\tilde{0}|H|A,\tilde{0}\rangle, \qquad (3.56)$$

with

$$H = \sum_i \varepsilon_i a_i^\dagger a_i + \sum_{m<n,p<q} V_{mn,pq}a_m^\dagger a_n^\dagger a_q a_p, \qquad (3.57)$$

where the indices i,m,n... refer to occupied or unoccupied nucleon states. Rewriting H in terms of operators A and $A^\dagger$, using RPA equations and occupation numbers from Eqs.(3.51) and (3.52), we get, after a tedious but straightforward calculation, the final expression:

$$E_0 = E_{HF} - \sum_M E_M \sum_{ab}|Y^{(M)}_{ab}|^2 - \sum_N E_N \sum_{\alpha\beta}|X^{(N)}_{\alpha\beta}|^2, \qquad (3.58)$$

where E_{HF} is the Hartree Fock binding energy given by:

$$E_{HF} = \sum_\alpha \varepsilon_\alpha - \sum_{\alpha<\beta} V_{\alpha\beta,\alpha\beta}. \qquad (3.59)$$

3.4 Properties of the A+2 nucleus

We concentrate on the A+2 nucleus even though our RPA equations give at the same time a description of both, A+2 and A-2 nuclei. Therefore all our formulae derived for the A+2 nucleus can be automatically generalized to the case of A-2 nucleus. First the expansion of the wave function, Eq.(3.17), on configurations with two particles, four particles-two holes etc... is given. Then two classes of properties will be studied. We first consider some properties of the ground state or more precisely the properties due to the two nucleons added to the core

such as: the increase in the nucleus radius,which is particularly interesting in the case of two-neutron halo nuclei; the distance between the two extra-nucleons; their distance to the core center-of-mass. These calculations require the knowledge of matrix elements of one and two-body operators between RPA states. Their derivation will be the object of the second part of this chapter. Then a derivation of the transition matrix elements between the ground state and an excited state of the A+2 nucleus will be given. A two-particle RPA model gives only two-body amplitudes between the core and the A+2 nucleus so that transition within the A+2 nucleus requires further developments.

3.4.1 The wave function of the A+2 nucleus.

Following Eqs.(3.17) and (3.29), we write the A+2 nucleus wave function for a state N as:

$$\begin{aligned} |A+2,N\rangle &= Q_N^\dagger |A,\tilde{0}\rangle \\ &= N_0 Q_N^\dagger e^S |0\rangle. \end{aligned} \tag{3.60}$$

By using again Eq.(3.45) for the product $Q_N^\dagger e^S$ and Eq.(3.23) giving $Q_N^\dagger$ in terms of the pair operators A and $A^\dagger$ one gets:

$$|A+2,N\rangle = e^S \sum_a Z_{ab}^{(N)} A_{ab}^+ |0\rangle, \tag{3.61}$$

with:

$$Z_{ab}^{(N)} = N_0 \{ X_{ab}^{(N)} - \sum_{\alpha\beta} c_{ab,\alpha\beta}(J_N) X_{\alpha\beta}^{(N)} \}, \tag{3.62}$$

where J_N is the angular momentum of the state N. By expanding the exponential we get the components of the wave function on configurations with 2n+2 particles and 2n holes as:

$$\begin{aligned} |A+2,N\rangle &= \sum_a Z_a(N) A_a^\dagger(J_N) |A,0\rangle \\ &\quad + \sum_{ab\beta,J} (2J+1) c_{b\beta}(J) Z_a(J_N) A_b^\dagger(J) A_\beta(J) A_a^\dagger(J_N) |A,0\rangle + \ldots \end{aligned} \tag{3.63}$$

In the last equation, to simplify the notation, the indices a, b..., α, β refer to two-nucleon states.

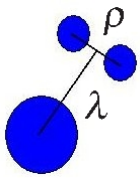

Figure 3.2: Definition of $\sqrt{\langle\rho^2\rangle}$ and $\sqrt{\langle\lambda^2\rangle}$.

3.4.2 The effect of the two extra nucleons on the properties of the whole system

The mean square radius of the A+2 system is an important observable which has to be calculated. It can be expressed as:

$$\langle r^2\rangle_{A+2} = \frac{A}{A+2}\langle r^2\rangle_A + \delta\langle r^2\rangle, \tag{3.64}$$

with:

$$\delta\langle r^2\rangle = \frac{1}{A+2}\left(\frac{2A}{A+2}\langle\lambda^2\rangle + \frac{1}{2}\langle\rho^2\rangle\right), \tag{3.65}$$

where λ and ρ are respectively the distance between the centers of mass of the two added nucleons and the core and the distance between the two nucleons. They are given by:

$$\lambda^2 = \frac{1}{4}(\overrightarrow{r_1} + \overrightarrow{r_2})^2 \tag{3.66}$$

$$\rho^2 = |\overrightarrow{r_1} - \overrightarrow{r_2}|^2 \tag{3.67}$$

where $\overrightarrow{r_1}$ and $\overrightarrow{r_2}$ are the coordinates of the two added nucleons relative to the center of mass of the core.

The calculation of the rms of Eq.(3.64) necessitates the calculation of the average value of one and two body operators on the system formed by the two extra nucleons. Then given an operator F, we have to calculate

$$\langle F\rangle = \langle A+2,0|F|A+2,0\rangle - \langle A,\tilde{0}|F|A,\tilde{0}\rangle. \tag{3.68}$$

The wave function $|A+2,0\rangle$ corresponds to the ground state. To the lowest order, the RPA solution with N=0, and following Eq.(3.17), is given by:

$$|A+2,0\rangle = Q_0^\dagger|A,\tilde{0}\rangle, \tag{3.69}$$

with:

$$Q_0^\dagger = \sum_{ab} X_{ab}^{(0)} A_{ab}^\dagger - \sum_{\alpha\beta} Y_{\alpha\beta}^{(0)} A_{\alpha\beta}^\dagger, \tag{3.70}$$

so that Eq.(3.68) can be transformed into:

$$\begin{aligned}\langle F\rangle &= \langle A,\tilde{0}|Q_0 F Q_0^\dagger|A,\tilde{0}\rangle - \langle A,\tilde{0}|F|A,\tilde{0}\rangle \\ &= \langle A,\tilde{0}|Q_0[F,Q_0^\dagger]|A,\tilde{0}\rangle. \end{aligned} \tag{3.71}$$

This formula can be applied to any one- or two-body operator respectively F_1 and F_2. In both cases the calculation of the commutators is straightforward, even though quite tedious. We show the details of this calculation as it has not been done before.

One-body operator

We want the average of a one-body operator for the two extra-neutrons in the halo

$$\begin{aligned}\langle F_1\rangle &= \sum_{mn}\langle m|F_1|n\rangle\{\langle\tilde{0}|Q_0 a_m^\dagger a_n Q_0^\dagger|\tilde{0}\rangle - \langle\tilde{0}|a_m^\dagger a_n|\tilde{0}\rangle\} \\ &= \sum_{mn}\langle m|F_1|n\rangle\langle\tilde{0}|Q_0[a_m^\dagger a_n, Q_0^\dagger]|\tilde{0}\rangle \end{aligned} \tag{3.72}$$

using Eq.(3.69) and (3.70). If m and n are unoccupied states,

$$[a_m^\dagger a_n, a_a^\dagger a_b^\dagger] = A_{mb}^\dagger\delta_{nb} + A_{am}^\dagger\delta_{nb} \tag{3.73}$$

we take $m\equiv\mu$ and $n\equiv\nu$ if they are occupied states,

$$[a_\mu^\dagger a_\nu, a_\alpha^\dagger a_\beta^\dagger] = A_{\mu\beta}^\dagger\delta_{\nu\beta} + A_{\alpha\mu}^\dagger\delta_{\nu\beta} \tag{3.74}$$

$$[a_m^\dagger a_n, Q_0^\dagger] = \sum_{ab} X_{ab}^{(0)}(A_{am}^\dagger\delta_{nb} + A_{mb}^\dagger\delta_{na}) - \sum_{\alpha\beta} X_{\alpha\beta}^{(0)}(A_{\alpha\beta}^{(0)}(A_{\alpha m}^\dagger\delta_{n\beta} + A_{m\beta}^\dagger\delta_{n\alpha})) \tag{3.75}$$

$$\langle\tilde{0}|Q_0 A_{mn}^\dagger|\tilde{0}\rangle = X_{mn}^{(0)}\langle\tilde{0}|Q_0 A_{\mu\nu}^\dagger|\tilde{0}\rangle = X_{\mu\nu}^{(0)} \tag{3.76}$$

$$\begin{aligned}\langle F_1\rangle &= \sum_{mn}\langle m|F_1|n\rangle\sum_{ab}X_{ab}^{(0)}(X_{am}^{(0)}\delta_{nb} + X_{mb}^{(0)}\delta_{na}) \\ &- \sum_{\mu\nu}\langle\mu|F_1|\nu\rangle\sum_{\alpha\beta}X_{\alpha\beta}^{(0)}(X_{\alpha\mu}^{(0)}\delta_{\nu\beta} + X_{\mu\beta}^{(0)}\delta_{\nu\alpha}) \\ &= \sum_{mn}\langle m|F_1|n\rangle\{\sum_a X_{an}X_{am} + \sum_b X_{nb}X_{mb}\} \\ &- \sum_{\mu\nu}\langle\mu|F_1|\nu\rangle\{\sum_\alpha X_{\alpha\nu}X_{\alpha\mu} + \sum_\beta X_{\mu\beta}X_{\nu\beta}\}. \end{aligned} \tag{3.77}$$

Finally, we obtain

$$\begin{aligned}\langle F_1\rangle &= 2\sum_{mn}\langle m|F_1|n\rangle\sum_a X^{(0)}_{an}X^{(0)}_{am} \\ &- 2\sum_{\mu\nu}\langle \mu|F_1|\nu\rangle\sum_\alpha X^{(0)}_{\alpha\mu}X^{(0)}_{\alpha\mu} \end{aligned} \tag{3.78}$$

If F_1 is chosen as the number operator,

$$\begin{aligned}\langle A+2|a^\dagger_m a_m|A+2\rangle - \langle A|a^\dagger_m a_m|A\rangle &= 2\sum_{ma}|X^{(0)}_{am}|^2 - 2\sum_{\mu\alpha}|X^{(0)}_{\alpha\mu}|^2 \\ &= 2. \end{aligned} \tag{3.79}$$

Two-body operator

Now we do the same calculation for a two-body operator F_2,

$$F_2 = \sum_{k<l,m<n}\langle kl|F_2|mn\rangle a^\dagger_k a^\dagger_l a_m a_n \tag{3.80}$$

with $k<l$ and $m<n$. Using the 'quasi boson approximation', we have the following commutation rules

$$\left[A_{kl}, A^\dagger_{mn}\right] = \delta_{kl,mn} \tag{3.81}$$

$$\left[A_{\kappa\lambda}, A^\dagger_{\mu\nu}\right] = -\delta_{\kappa\lambda,\mu\nu} \tag{3.82}$$

and the other operator combinations commute.

$$\left[A^\dagger_{kl}A_{mn}, Q^\dagger_0\right] = \sum_{ab}X^{(0)}_{ab}\left[A^\dagger_{kl}A_{mn}, A^\dagger_{ab}\right] - \sum_{\alpha\beta}X^{(0)}_{\alpha\beta}\left[A^\dagger_{kl}A_{mn}, A^\dagger_{\alpha\beta}\right]. \tag{3.83}$$

Here we treat the different cases separately:
I. *kl*,*mn* unoccupied

$$\begin{aligned}\left[A^\dagger_{kl}A_{mn}, A^\dagger_{ab}\right] &= A^\dagger_{kl}A_{mn}A^\dagger_{ab} - A^\dagger_{ab}A^\dagger_{kl}A_{mn} \\ &= A^\dagger_{kl}\left(\delta_{mn,ab} + A^\dagger_{ab}A_{mn}\right) - A^\dagger_{ab}A^\dagger_{kl}A_{mn} \\ &= A^\dagger_{kl}\delta_{mn,ab} \end{aligned} \tag{3.84}$$

$$\begin{aligned}\left[A^\dagger_{kl}A_{mn}, A^\dagger_{\alpha\beta}\right] &= A^\dagger_{kl}A_{mn}A^\dagger_{\alpha\beta} - A^\dagger_{\alpha\beta}A^\dagger_{kl}A_{mn} \\ &= A^\dagger_{kl}\left(\delta_{mn,\alpha\beta} + A^\dagger_{\alpha\beta}A^\dagger_{kl}A_{mn}\right) - A^\dagger_{\alpha\beta}A^\dagger_{kl}A_{mn} \\ &= 0 \end{aligned} \tag{3.85}$$

II. $\kappa\lambda$,$\mu\nu$ occupied

$$\begin{aligned}\left[A^\dagger_{\kappa\lambda}A_{\mu\nu},A^\dagger_{ab}\right] &= 0 \qquad (3.86)\\ \left[A^\dagger_{\kappa\lambda}A_{\mu\nu},A^\dagger_{\alpha\beta}\right] &= A^\dagger_{\kappa\lambda}A_{\mu\nu}A^\dagger_{\alpha\beta}-A^\dagger_{\alpha\beta}A^\dagger_{\kappa\lambda}A_{A_{\mu\nu}}\\ &= -\delta_{\alpha\beta,\mu\nu}A^\dagger_{\kappa\lambda} \qquad (3.87)\end{aligned}$$

III. kl,$\mu\nu$

$$\begin{aligned}\left[A^\dagger_{kl}A_{\mu\nu},A^\dagger_{ab}\right] &= A^\dagger_{kl}A_{\mu\nu}A^\dagger_{ab}-A^\dagger_{ab}A^\dagger_{kl}A_{\mu\nu}\\ &= 0\\ \left[A^\dagger_{kl}A_{\mu\nu},A^\dagger_{\alpha\beta}\right] &= A^\dagger_{kl}A_{\mu\nu}A^\dagger_{\alpha\beta}-A^\dagger_{\alpha\beta}A^\dagger_{kl}A_{\mu\nu}\\ &= -\delta_{\mu\nu,\alpha\beta}A^\dagger_{kl}. \qquad (3.88)\end{aligned}$$

IV. $\kappa\lambda$,mn

$$\begin{aligned}\left[A^\dagger_{\kappa\lambda}A_{mn},A^\dagger_{ab}\right] &= A^\dagger_{\kappa\lambda}A_{mn}A^\dagger_{ab}-A^\dagger_{ab}A^\dagger_{\kappa\lambda}A_{mn}\\ &= A^\dagger_{\kappa\lambda}\left(\delta_{mn,ab}+A^\dagger_{ab}A_{mn}\right)-A^\dagger_{ab}A^\dagger_{\kappa\lambda}A_{mn}\\ &= A^\dagger_{\kappa\lambda}\delta_{mn,ab}. \qquad (3.89)\end{aligned}$$

Finally

$$\begin{aligned}\langle F_2\rangle &= \sum_{klmn}\langle kl|F_2|mn\rangle X^{(0)}_{mn}\langle\tilde{0}|Q_0A^\dagger_{kl}|\tilde{0}\rangle\\ &+ \sum_{\kappa\lambda\mu\nu}\langle\kappa\lambda|F_2|\mu\nu\rangle X^{(0)}_{\mu\nu}\langle\tilde{0}|Q_0A^\dagger_{\kappa\lambda}|\tilde{0}\rangle\\ &+ \sum_{\kappa\lambda mn}\langle\kappa\lambda|F_2|mn\rangle X^{(0)}_{mn}\langle\tilde{0}|Q_0A^\dagger_{\kappa\lambda}|\tilde{0}\rangle\\ &+ \sum_{kl\mu\nu}\langle kl|F_2|\mu\nu\rangle X^{(0)}_{\mu\nu}\langle\tilde{0}|Q_0A^\dagger_{kl}|\tilde{0}\rangle, \qquad (3.90)\end{aligned}$$

using

$$\begin{aligned}\langle\tilde{0}|Q_0A^\dagger_{kl}|\tilde{0}\rangle &= X^{(0)}_{kl}\\ \langle\tilde{0}|Q_0A^\dagger_{\kappa\lambda}|\tilde{0}\rangle &= X^{(0)}_{\kappa\lambda}, \qquad (3.91)\end{aligned}$$

$$\begin{aligned}\langle F_2\rangle &= \sum_{klmn}\langle kl|F_2|mn\rangle X^{(0)}_{mn}X^{(0)}_{kl}\\ &+ \sum_{\kappa\lambda\mu\nu}\langle \kappa\lambda|F_2|\mu\nu\rangle X^{(0)}_{\mu\nu}X^{(0)}_{\kappa\lambda}\\ &+ \sum_{\kappa\lambda mn}\langle \kappa\lambda|F_2|mn\rangle X^{(0)}_{mn}X^{(0)}_{\kappa\lambda}\\ &+ \sum_{kl\mu\nu}\langle kl|F_2|\mu\nu\rangle X^{(0)}_{\mu\nu}X^{(0)}_{kl},\end{aligned} \tag{3.92}$$

and

$$\begin{aligned}\langle F_2\rangle &= \sum_{klmn}\langle kl|F_2|mn\rangle X^{(0)}_{mn}X^{(0)}_{kl}\\ &+ 2\sum_{kl\mu\nu}\langle kl|F_2|\mu\nu\rangle X^{(0)}_{\mu\nu}X^{(0)}_{kl}\\ &+ \sum_{\kappa\lambda\mu\nu}\langle \kappa\lambda|F_2|\mu\nu\rangle X^{(0)}_{\mu\nu}X^{(0)}_{\kappa\lambda}.\end{aligned} \tag{3.93}$$

Finally the average value for a two-body operator is given by

$$\begin{aligned}\langle A+2|F_2|A+2\rangle - \langle A|F_2|A\rangle &= \sum_{klmn}\langle kl|F_2|mn\rangle X^{(0)}_{mn}X^{(0)}_{kl}\\ &+ 2\sum_{kl\mu\nu}\langle kl|F_2|\mu\nu\rangle X^{(0)}_{\mu\nu}X^{(0)}_{kl} + \sum_{\kappa\lambda\mu\nu}\langle \kappa\lambda|F_2|\mu\nu\rangle X^{(0)}_{\mu\nu}X^{(0)}_{\kappa\lambda},\end{aligned}$$

then we have

$$\begin{aligned}\langle F_2\rangle &= \sum_{k<l,m<n}\langle kl|F_2|mn\rangle X^{(0)}_{mn}X^{(0)}_{kl}\\ &+ 2\sum_{k<l,\mu<\nu}\langle kl|F_2|\mu\nu\rangle X^{(0)}_{\mu\nu}X^{(0)}_{kl}\\ &+ \sum_{\kappa<\lambda,\mu<\nu}\langle \kappa\lambda|F_2|\mu\nu\rangle X^{(0)}_{\mu\nu}X^{(0)}_{\kappa\lambda}.\end{aligned} \tag{3.94}$$

These two equations can be used to calculate the radius and distances of Eqs.(3.64) and (3.67). Eq.(3.78) can be verified by using it to calculate the number of nucleons outside the core, which gives:

$$\begin{aligned}\delta N &= 2\sum_{ma}|X^{(0)}_{am}|^2 - 2\sum_{\mu\alpha}|X^{(0)}_{\alpha\mu}|^2\\ &= 2\end{aligned} \tag{3.95}$$

3.4.3 Transition amplitudes

We are interested by transitions between the ground state (N=0) and an excited state (N≠0) of the A+2 nucleus through a one-body operator (D). This is the case of electromagnetic transitions for example. The amplitude for such a transition is given by:

$$D(0 \rightarrow N) = \sum_{ij} \langle i|D|j\rangle \langle A,\tilde{0}|Q_N a_i^\dagger a_j Q_0^\dagger|A,\tilde{0}\rangle. \tag{3.96}$$

The sum over i and j runs on all nucleon states, occupied or not. We can rewrite D as:

$$D(0 \rightarrow N) = \sum_{ij} \langle i|D|j\rangle \langle A,\tilde{0}|Q_N[a_i^\dagger a_j, Q_0^\dagger]|A,\tilde{0}\rangle. \tag{3.97}$$

The commutator has already been calculated previously and using the relations:

$$\begin{aligned} \langle A,\tilde{0}|Q_N A_{ij}^\dagger|A,\tilde{0}\rangle &= \langle A+2,N|A_{ij}^\dagger|A,\tilde{0}\rangle & (3.98)\\ &= X_{ij}^{(N)}, & (3.99) \end{aligned}$$

we get:

$$\begin{aligned} D(0 \rightarrow N) &= \sum_{a_0 b_0 a_1 b_1} X_{a_1 b_1}^{(N)} X_{a_0 b_0}^{(0)} [\langle a_1|D|a_0\rangle \delta_{b_1 b_0} + \langle b_1|D|b_0\rangle \delta_{a_0 a_1}] \\ &- \sum_{\alpha_0 \beta_0 \alpha_1 \beta_1} X_{\alpha_1 \beta_1}^{(N)} X_{\alpha_0 \beta_0}^{(0)} [\langle \alpha_1|D|\alpha_0\rangle \delta_{\beta_0 \beta_1} + \langle \beta_1|D|\beta_0\rangle \delta_{\alpha_0 \alpha_1}]. \end{aligned} \tag{3.100}$$

Using the closure relation, we obtain the sum rule for the E1 strength. We can show that the total B(E1) obeys to a sum rule such that:

$$B(E1) = \frac{3}{\pi} e^2 \left(\frac{Z}{A}\right)^2 \lambda^2$$

where λ (stands for $\sqrt{\langle \lambda^2 \rangle}$) is the average distance between the two neutrons, see Fig. 3.2.

In this section, theoretical tools have been presented in order to get observables from the amplitudes provided by the p-p RPA. In the next section they are applied to some Beryllium isotopes.

3.5 Interactions

In the model, the three-body system, one core surrounded by two neutrons, is characterized by two interactions, see Fig. 3.3:

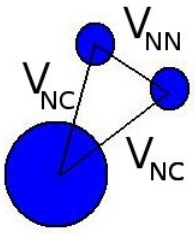

Figure 3.3: Different interactions of the three-body system. V_{NC}: neutron-core potential. V_NN: neutron-neutron potential.

- V_{NN} is the neutron-neutron interaction which is taken as the Gogny D1S [87, 88].
- V_{NC} is the neutron-core interaction. We take a Woods-Saxon plus a correction due to particle-vibration coupling.

These two interactions are described more accurately in the following.

3.5.1 NN Gogny effective interaction

For the neutron-neutron system we use the Gogny effective interaction given by:

$$\begin{aligned} V(1,2) &= \sum_{i=1}^{2} e^{-(\vec{r}_1-\vec{r}_2)^2/\mu_i^2}(W_i + B_i P_\sigma - H_i P_\tau - M_i P_\sigma P_\tau) \\ &+ t_3(1+x_0 P_\sigma)\delta(\vec{r}_1-\vec{r}_2)\left[\rho\left(\frac{\vec{r}_1+\vec{r}_2}{2}\right)\right]^\alpha \\ &+ iW_{LS}\overleftarrow{\nabla}_{12}\delta(\vec{r}_1-\vec{r}_2)\times\overrightarrow{\nabla}_{12}.(\vec{\sigma}_1+\vec{\sigma}_2) \\ &+ (1+2\tau_{1z})(1+2\tau_{2z})\frac{e^2}{|\vec{r}_1-\vec{r}_2|} \end{aligned} \tag{3.101}$$

In this expression, the first line represents the central part of the finite range part of the force (μ_j is the range parameter), the second line represents the density dependent term and the third line represents a zero-range spin-orbit term. The last line represents the Coulomb interaction between protons (τ_{iz}=1/2 for protons and τ_{iz}=-1/2 for neutrons). The interaction parameters have been adjusted to fit the global mean-field properties of stable nuclei and to fit the pairing correlations existing between nucleons [87, 88]. We notice that the Gogny interaction has been parameterized from characteristics of stable nuclei. In our calculation, we use it for light dripline nuclei and we will see that good results are obtained without any renormalization of the effective interaction. Thus the Gogny effective interaction seems already very promising far from β-stability. The D1S parameters are given in Table. 3.1.

Table 3.1: Force parameters of the Gogny force (D1S)

i	μ_i [fm]	W_i	B_i	H_i	M_i [MeV]
1	0.7	-1720.3	1300	-1813.53	1397.6
2	1.2	103.64	-163.48	162.81	-223.93

3.5.2 Woods-Saxon and Particle-Vibration Coupling

For the neutron-core interaction, we use a Woods-Saxon potential with the parameters given in [53] and in Table 2.6, corrected by a surface term, coming from particle-vibration coupling that we used also in the two previous chapters. We notice that the physical meaning of this interaction is slightly different from the one used in projectile fragmentation, calculation of chapter 2, as here we take into account explicitly the neutron-neutron interaction. In projectile fragmentation, we treat only one neutron so the interaction with the second neutron is included implicitly in the neutron-core interaction.

$$U(r) = V_{WS} + \delta V, \;\; \delta V(r) = 16\alpha_l e^{2(r-R)/a}/(1+e^{(r-R)/a})^4 \tag{3.102}$$

The α_l term is a l-dependent term, which means that the correction is different for each angular momentum, but the Woods-Saxon potential is the same for all the states. Thus we fit the neutron-core interaction with this α_l, but the correction in itself has a physical origin that give in the following.

The term $\left(\frac{dU(r)}{dr}\right)^2$, in the RHS of Eq.(3.102), which we add to the Woods-Saxon potential is a direct consequence of two papers. The first work [89] where the authors gave the general microscopic expression of the mass operator but they calculated only the p-h RPA term. In the second work [53], the authors gave an exact expression of the term correcting the HF potential and due to two-body correlations (Eq.1 of [53]). This term depends on the energy of the considered neutron, on the energy of the vibrational states involved, on what the authors called V_{ON}, the probability for exciting the N phonon and finally on the intermediate wave functions ϕ_λ. The form factor is non local and complicated to calculate. This is why, since they were interested by general properties, they simplified the calculation by using the collective model and using the fact that due to the energy denominators only low energy phonons contribute noticeably. Then the radial part becomes non local; and of the form

$$\sum_\lambda \phi^*_\lambda(\overrightarrow{r})\phi_\lambda(\overrightarrow{r'})\left(\frac{dU}{dr}\right)_r\left(\frac{dU}{dr}\right)_{r'}. \tag{3.103}$$

However with Bouyssy [110], they have shown that the non locality range is small and the ϕ_λ

does not play any role in the shape of the form factor since the $\frac{dU}{dr}$ term has a dominant radial dependence (i.e. the radial dependence is dominated by the derivative factor). Thus we may simplify this correction term as $\left(\frac{dU(r)}{dr}\right)^2$. The strength α_n of the correction term as shown in the Eq. 3.102 depends on the energy of the neutron considered. In our case, we decided to use α_n as a parameter to fit the neutron-core energies. As we consider states with different J^π, we do not calculate explicitly the energy dependence of the correction and we fit α_n to obtain the s and p level inversion.

This phenomenological way of proceeding can be adopted because we are interested by two-neutron systems and then it is important to have a good representation of one-neutron systems. It is however a phenomenology based on serious microscopic properties. The success of this approach can be seen in [90]. With such a potential fitted on ^{11}Be, the ^{11}N states measured experimentally, were calculated. The agreement was quite good and what is still more interesting is that experimentalists were not able to get a good agreement just by fitting the strength V_0 of a simple Woods-Saxon potential while by using a larger radius the agreement improved and this is exactly what the surface correction does to the potential.

In [105], the author showed the equivalence between assuming a deformation of the core deduced from the low energy 2^+ state properties and taking into account the coupling of the neutron with this 2^+ state interpreted as a spherical one-phonon state. If the 2^+ state is rotational, β_2 is interpreted as a deformation parameter. If the 2^+ state is vibrational, β_2 is a collective transition amplitude. This unify the two techniques usually used in halo nuclei structure: core deformation and particle-vibraction coupling.

3.6 Beryllium Isotopes

The p-p RPA implies a double constraint: one needs to reproduce both $A+2$ and $A-2$ nucleus characteristics within the same calculation. We cannot adjust independently the amplitudes related to the $A+2$ and $A-2$. We apply the p-p RPA to A=10 and A=12 Beryllium cores. This will give information about ^{8}Be, ^{10}Be, ^{14}Be, and twice about ^{12}Be. One more constraint will be to obtain the same results for ^{12}Be with a ^{10}Be and with a ^{12}Be core. As an input, we need the n+core and n+n interactions. In the case of the ^{10}Be core, we need to know the ^{11}Be spectrum. ^{11}Be is well known both experimentally and theoretically and its characteristics are summarized in the the following section. In order to reproduce the ^{11}Be spectrum, with an inversion of the s and p states, we use the particle-vibration coupling model described more accurately in the following. All the inputs are known in the p-p RPA model with a ^{10}Be core, we compare our results obtained for ^{10}Be and ^{12}Be, with experimental values of rms, energy of the states and

B(EL). A good agreement with experimental values will validate the model. In the case of a ^{12}Be core, we have to know the spectrum of the unbound ^{13}Be. Until now, it remains some doubts on the interpretation of experimental results for low-lying states. This subject has been discussed at length in chapter 2. The strategy is now to rely on the p-p model to test some possible inputs and see which one gives a better representation of ^{10}Be and ^{14}Be.
Let us remind that as a result of the p-p RPA, amplitudes are obtained. Therefore there is some work to do in order to obtain from these amplitudes experimental observables such as: rms, B(EL),etc... The determination of the theoretical expressions was treated in the previous section. Here, we present the interactions used in the model. Then, we give a brief summary of the experimental knowledge on Beryllium isotopes. We make also a review of the theoretical methods used until now to study these nuclei. Finally, we compare and discuss our results with respect to experimental values.

3.6.1 Experimental results on Beryllium isotopes

In this part, we summarize the main experimental results available on Beryllium isotopes. Experimental data on ^{11}Be, ^{13}Be and ^{14}Be has already been presented in Chapter 2. Here we show only results on ^{12}Be.

^{12}Be Experiments

Experimentally, ^{12}Be has a large two-neutron separation energy of 3.67 MeV, much larger than that for ^{11}Li, so it is perhaps not a very good example of halo nucleus, but it represents a good test for a three-body approach because ^{10}Be is a well closed core. It provides also a useful test of model with intruder-state mixing, and it is necessary to understand ^{12}Be before discussing ^{14}Be.

In recent years much evidence has been accumulated consistent with a strong quadrupole deformation. The associated coupled-channels analysis deduced a deformation length δ =2.00±0.23 fm for this state (corresponding to β=0.728±0.084 when $R = 1.2 \times A^{1/3}$), confirming that the closed shell structure does not dominate in ^{12}Be. The most direct observation of the disappearance of the $N = 8$ closed shell in ^{12}Be arises from the one-neutron knockout reaction, measured at MSU on a ^{9}Be target [96]. The spectroscopic factors and momentum distributions of the ^{11}Be residues in their $(1/2)^+$ ground state and $(1/2)^-$ excited state reveal that the last neutrons have a significant $\left[2s_{1/2}\right]^2 + \left[1d_{5/2}\right]^2$ configuration and the $(1p_{1/2})^2$ closed shell component is only of order 30%. The dipole strength B(E1; $1^- \rightarrow 0^+$) value is estimated to be 0.017±0.004 $e^2.fm^2$.

Iwasaki et al. [97] extracted a nuclear deformation length from proton inelastic scatter-

ing. Even though no electromagnetic experimental value is quoted, shell-model calculations performed therein, suggest the data is consistent with $\delta_{e.m.}$=2.79 fm. This corresponds to the quadrupole strength

$$\begin{aligned} B\left(E2, 0^+ \rightarrow 2^+\right) &= \left[\frac{3ZR\delta_{e.m.}}{4\pi}\right]^2 \\ &\approx 50\ e^2.fm^4. \end{aligned} \tag{3.104}$$

In a recent experiment at RIKEN, $^{18}O+^{9}$Be $\rightarrow^{12}$Be at 100 A.MeV, Shimoura and al. [98], identified several states of ^{12}Be: 0.0 MeV (0^+), 2.107 MeV (2^+), 2.251 MeV (0^+), 2.71 MeV (1^-) in excitation energy. They determined also some new transition rates:

$$\begin{aligned} M\left(E0; 0_2^+ \rightarrow 0_1^+\right) &= |\left\langle 0_2^+ | \sum e r_i^2 | 0_1^+ \right\rangle| \\ &= 0.87 \pm 0.03\ e.fm^2 \end{aligned} \tag{3.105}$$

$$B\left(E2; 0_2^+ \rightarrow 2^+\right) = 7.0 \pm 0.6\ e^2.fm^4 \tag{3.106}$$

Experimental results are then summarized in Table 3.2 and compared to p-p RPA results.

3.6.2 Overview of the theoretical methods

Some of the theoretical methods used to study ^{14}Be have already been presented in Chapter 2. Here we resume the theoretical methods used to study ^{12}Be.

^{12}Be Theoretically

The ground state of ^{12}Be can be sought as a solution of a three-body problem for two neutrons outside a ^{10}Be core, once the potentials are defined to ensure that the two-body n+^{10}Be subsystem has the known eigenstates for ^{11}Be, as given in Table 2.1. In [70], Thompson et al. obtained the parity inversion observed experimentally, by tuning the depth of the potential. In [70], the phenomenon of an s-intruder orbit was examined for the ^{12}Be and ^{14}Be isotopes. Although ^{11}Be has an s-wave ground state, a three-body model of two neutrons plus a ^{10}Be core reproduces properties of the ^{12}Be only if the valence neutrons occupy mainly the $(p_{1/2})^2$ configuration with about 25% admixture of $(sd)^2$ configurations. This results in a ground state wave function not extending to very large radii as it occurs instead with many halo nuclei. Another reason which makes the ^{12}Be nucleus interesting is that it differs by only one (deeply bound) proton from ^{11}Li, and hence its neutron wave function should show some similarities to the halo structure seen in ^{11}Li.

In Ref. [99], Nunes et al. consider ^{12}Be as a ^{10}Be+n+n in a three-body model, including core excitation. To reproduce the spectroscopy deduced from the single-neutron knock-out reaction,

the p-wave component of the ^{12}Be groud state wavefunction needs to be increased significantly. This can be achieved, within the three-body model, only through a reduced core deformation, and hence a reduced core excitation. Their results imply that adding an extra neutron to the ^{11}Be system depolarizes the core and reduces the deformation of the effective field it creates. This increasing sphericity of the ^{10}Be core leads to an enhanced probability of the core being in its ground state to an increased mixing of the valence neutron states between the p- and the sd-shell, and to a melting of the N=8 neutron shell closure, in agreement with recent findings. However, the three-body model underpredicts the B(E2) in ^{12}Be and also produces in ^{11}Be a too large B(E1).

Shell-model studies [106],[94] and [107] predict, consistently, a significant $(sd)^2$ component for the valence neutrons. The available shell model calculations treat the p- and sd-shells separately, each with up to four excitations, but do not include full (psd)-shell configuration mixing. While such calculations are becoming feasible, the determination of a suitable effective interaction in this extended model space is itself a major project. Between the microscopic and macroscopic models, the molecular orbital model was recently applied to Beryllium isotopes [109]. There, ^{12}Be is treated as a four-neutron plus two-α structure. Once again, the breakdown of the N=8 shell closure and the role of the spin orbit interaction are important issues.

In recent years, there have been a number of attempts to start from a state-independent effective nucleon nucleon interaction (such as the Volkov or the Minnesota potential), and deduce the existence of s-wave intruder states and N = 8 shell melting in nuclei such as ^{10,11}Li and ^{11}Be. All these attempts give p-shell states at energies below those of sd-shell states, and therefore fail to describe the inversions seen experimentally. Thus there is still need for few-body models which use phenomenological neutron core interactions fitted to measured resonances and virtual states.

3.7 RPA results for Beryllium isotopes

We apply now the p-p RPA calculation to the case of a ^{10}Be core and a ^{12}Be core surrounded by two neutrons. This enables us to cover a range of Beryllium isotopes going from ^{8}Be to ^{14}Be. As said previously, we obtain information on ^{12}Be from both calculations. In this way a good test of the consistence of the model will be to obtain the same results in the two cases. All these calculations are done in a 20 fm box so that we obtain discret states of positive energy.

First, we apply the method to study ^{12}Be. In this case, we need the interaction n+^{10}Be, which is known to present a shell inversion between $p_{1/2}$ and $s_{1/2}$ shells. In order to obtain this inversion, we use the correction due to particle-vibration coupling tuned in order to obtain the shells at the expected energies. For the neutron-neutron interaction, we use the Gogny effective interaction D1S. Once these two interactions are fixed, we do not adjust anything else. The purpose of this

calculation is to fix all the known inputs and then see whether the results obtained for ^{12}Be are in agreement with experiments. If this is the case, it will validate our calculation and we will apply the same method to ^{14}Be, where the subsystem ^{13}Be is not well determined.

From our first calculation with a ^{10}Be core, we obtain the spectrum of ^{8}Be. We do not find any excited 0^+ nor 1^- states at low energy. This is in agreement with the experimental results. We find a 2^+ excited state at 3.1 MeV instead of 3.04 MeV. Usually, ^{8}Be is considered as a two-α system and within such a picture good results are obtained for the energy of the 2^+ excited state of ^{8}Be. In the p-p RPA, we obtain good results considering ^{8}Be as a ^{10}Be minus two neutrons. In the future it will be interesting to explore further the agreement between these different models.

The results of the calculation of the ^{12}Be spectrum are summarized in Table. 3.2. Here the results from the RPA calculation are compared to the experimental values. The energies of several states have been calculated: 0^+, 1^- and 2^+. For the 0^+ and 1^- states, there is a good agreement with experimental results. Also, good results are found for the two-neutron separation energy in ^{10}Be and ^{12}Be and for the ^{12}Be rms. In the case of the 2^+ state, the calculation gives a state corresponding to the two extra neutrons in a 2^+ state with a ^{12}Be core in its ground state. This is in good agreement with the second experimental 2^+. Then a hypothesis can be made for the interpretation of the first experimental 2^+: it might have the configuration $(2n)_{0+} \otimes^{10} Be(2^+)$ as ^{10}Be has a 2^+ excited state at E^* =3.4 MeV. This assumption is corroborated by the fact that the B(E2) is very close for ^{10}Be and ^{12}Be. The energy difference between the 2^+ experimental energy ε_{2+}=2.10 MeV and the core excitation energy E^* =3.4 MeV, is very likely due to the residual interaction between the two neutrons and ^{10}Be and it is expected to be negative. This residual interaction is coming from the particle-vibration coupling which has to be added as shown in Eq.3.107.

$$\varepsilon(^{11}Be) \quad = \quad \varepsilon(n) + \varepsilon(^{10}Be) + V_{res} \tag{3.107}$$

Thus the p-p RPA gives a good agreement for the energies of the ^{12}Be spectrum without any adjustment.

Having checked the validity of the calculation in the ^{12}Be case, we apply it to ^{14}Be. As previously said, we rely on the p-p RPA model to test some different scenarii for the ^{13}Be spectrum and see which hypothesis gives a better representation of ^{14}Be. Of course our model must satisfy the experimentally known properties of ^{13}Be. We adjust the α_l parameter such as to reproduce the experimental energy of the $1d_{5/2}$ resonance equal to 2.0 MeV. The lowest continuum state of ^{13}Be is adjusted to reproduce the two-neutron binding energy of ^{14}Be. We want to test two hypothesis in order to see which one gives a better representation of ^{14}Be. The first one is with the normal shell ordering obtained in a Woods-Saxon potential. This is the hypothesis which is most of the time validated by the previous theoretical works with an s-state at the threshold. The second hypothesis is to consider an inversion between the $1/2^+$ and $1/2^-$ states. The two scenarii are illustrated in Fig. 3.4. The different notation in Fig. 3.4

Table 3.2: Theoretical results vs. Experimental data. E and S_{2n} are respectively the energy of the excited states and the two-neutron separation energy in MeV. rms, $\sqrt{\langle\rho^2\rangle}$ and $\sqrt{\langle\lambda^2\rangle}$ are respectively the root mean squared radius, the average distance between the two halo neutrons and the average distance between the c.m. of the core and the c.m. of the two neutrons out of the core (see Fig. 3.2) in fm. B(E1) is the total dipole strength. The sum rule is calculated with Eq.(3.101) in e.fm^2. B(E2) is the total quadrupole strength in e^2.fm^4.

		RPA ^{10}Be core	Experiment	RPA ^{12}Be core Inversion	RPA ^{12}Be core Without Inversion
^{8}Be	E_{2+}	3.1	3.04		
^{10}Be	S_{2n}	8.29	8.5		
	E_{0+}		6.18	5.4	7.2
	E_{1-}		5.96	4.8	
^{12}Be	S_{2n}	3.63	3.67±0.015	3.83	1.16
	rms	2.76	2.59±0.06		
	E_{0+}	2.47	2.25		
	E_{1-} (1)	2.57	2.71		
	E_{1-} (2)	4.25			
	E_{1-} (3)	4.47			
	E_{2+} (1)		2.10		
	E_{2+} (2)	3.72	3.37		
^{14}Be	S_{2n}		1.34±0.11	1.33	0.54
	rms		3.1±0.4	2.90	3.51
	$\sqrt{\langle\rho^2\rangle}$		5.4±1.0	4.6	8.7
	$\sqrt{\langle\lambda^2\rangle}$		4.5±1.0	4.0	5.6
	E_{0+} (1)		2.56	2.74	1.71
	E_{0+} (2)			3.11	2.71
	E_{0+} (3)				2.83
	E_{1-} (1)		3.14	2.89	1.79
	E_{1-} (2)			3.38	1.86
	E_{1-} (3)			3.50	3.52
	E_{2+} (1)		1.59		
	E_{2+} (2)			3.16	2.03
	E_{2+} (3)			3.67	2.45

for the states in the two cases comes from the fact that without inversion, one is dealing with single-particle states where as in the case with inversion, we consider pseudo-states coupled with a phonon of the kind: $1/2^+ = \alpha(2s)_{HF} \otimes {}^{12}\mathrm{Be}(0^+) + \beta(5/2^+)_{HF} \otimes {}^{12}\mathrm{Be}(2^+)$. There are indications that in the n+^{12}Be system the same inversion than in ^{11}Be is present, because: (i) the inversion in ^{11}Be is due to the strong coupling with the 2^+ state in ^{10}Be. Experimentally a 2+ state with the same energy and B(E2) is known in ^{12}Be then we may expect the same effect on the neutron states than in ^{11}Be, namely an inversion of 2s and $1p_{1/2}$. (ii) ^{11}Be could be described as a neutron-hole in ^{12}Be then the ground state of ^{11}Be would have the characteristic of the last occupied shell in ^{12}Be which then should be a $1/2^+$ corresponding to an inversion of 2s and $1p_{1/2}$.

First, ^{10}Be is obtained (as a ^{12}Be core - 2 neutrons). Without inversion, we do not have any low-lying 1^- state in ^{10}Be (whereas a $1-$ is known experimentally at 5.96 MeV). With inversion, we obtain a 1^- state at an excitation energy of 4.8 MeV. One gets also a second excited 0^+ at 5.4 MeV with inversion and at 7.2 MeV without inversion, whereas the experimental value is 6.18 MeV. Therefore the results obtained for ^{10}Be are in favour of the scenario with inversion.

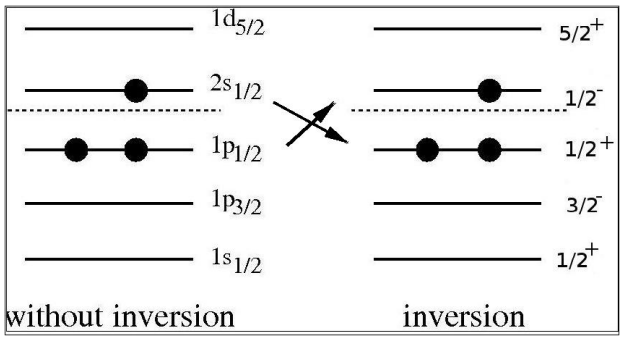

Figure 3.4: On the left hand side, scenario with no inversion in ^{13}Be. On the right hand side, scenario with inversion between s- and p-state.

The correction in Eq.(3.102) enables to make an inversion between the two states $1/2^+$ and $1/2^-$. In both cases, the first two core state are determined in a simple Woods-Saxon. In the case of inversion, the second $1/2^+$ is occupied and adjusted to have an energy of -3.15 MeV given by the experimental neutron separation energy in ^{12}Be.

In the following, we wish to calculate some observables corresponding to ^{14}Be in each scenario. Then a comparison will be made with the experimental values to check which scenario works better. The discretized spectrum adopted in each scenario for ^{13}Be is showed in Table. 3.3. Let us now analyse some features that can justify the inversion hypothesis. In Fig. 3.5, the various components of ^{12}Be are considered. The crosses represent the possible states available for the neutron. In each configuration only one neutron is added to form ^{13}Be, but we draw two crosses to show the two different possibilities. One can see that it is quite logical to conserve the inversion previously observed in ^{11}Be between the 2s and the $p_{1/2}$ shells. If the inversion

Table 3.3: ^{13}Be neutron spectrum with and without inversion with the corresponding α_l from Eq.(3.102). The continuum is discretized in a 20 fm box.

Inversion				Without Inversion			
Core							
l	j	ε (MeV)	α_l	l	j	ε (MeV)	α_l
0	1	-28.00	0	0	1	-28.00	0
1	3	-6.58	0	1	3	-6.58	0
0	1	-3.15	-23.3	1	1	-3.03	0
Continuum							
l	j	ε (MeV)	α_l	l	j	ε (MeV)	α_l (MeV)
1	1	0.67	8.9	0	1	0.09	-4.4
0	1	0.92	-35.5	1	3	1.20	0
1	3	1.20	0	1	1	1.27	0
1	1	1.27	0	2	3	1.83	0
2	3	1.83	0	0	1	1.97	0
2	5	2.00	-2.4	2	5	2.00	-2.4

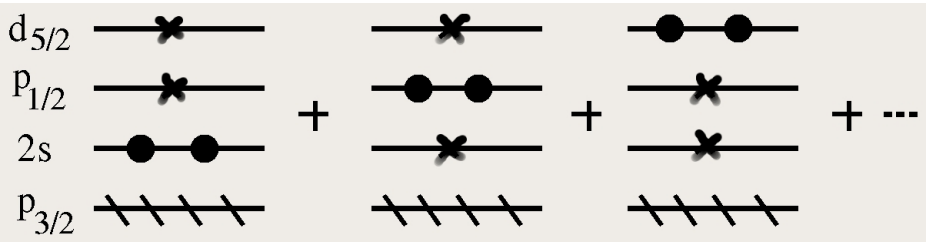

Figure 3.5: Formation of ^{13}Be with one neutron (crosses) added to an open shell ^{12}Be. Only one neutron is added in each configuration, but the cross indicates states which can be populated.

takes also place in ^{13}Be, we will observe a a low-lying p resonance and a d resonance in the n+^{12}Be spectrum corresponding to a closed shell ^{12}Be (first column in Fig. 3.5). On the other hand the two other configurations, corresponding to an open shell ^{12}Be allow the presence of p and d resonances coupled with an excited core. The very interesting point is that a low lying s-state in the continuum is present in the two last cases, thus showing the possibility of a $1/2^+$ ground state for ^{13}Be. However this s-state being coupled to an excited core would have a rather complicated structure and will not be a simple single particle state.

Thus the hypothesis we made in the previous chapter to interpret the n+^{12}Be spectrum obtained from ^{14}Be fragmentation seem to be confirmed by the structure calculations. We will come back to this point in the conclusions.

Afterwards using Eq.(3.78), we have determined the one-body density for a neutron in the halo. Let us remember that what we call density is in fact the density of the core substracted to the density of the whole nucleus in order to consider only the halo neutrons. This explains why, on Fig. 3.6, at small radii this 'density' is negative. We see that the no inversion scenario gives a bigger spatial extention than the case with inversion. Without inversion, because of the presence of a low-lying s-state in the continuum, a long tail in the matter distribution is expected. But as shown in Table 3.2, the rms obtained without inversion is too large compared to the experimental value. The agreement on rms is better in the case with inversion, even if the result obtained with the normal shell ordering is inside the error bars.
A more discriminating result is the one obtained for the two-neutron separation energy. Only

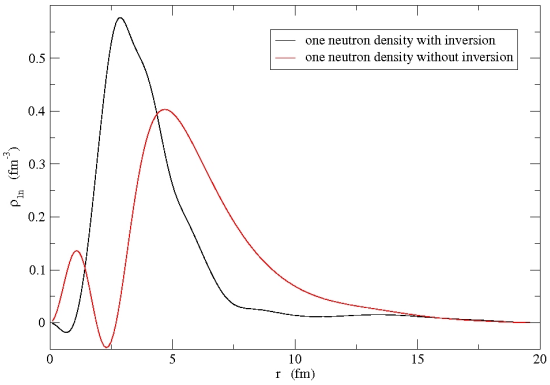

Figure 3.6: One-body density for a neutron in the halo of ^{14}Be. Results for the two ^{13}Be scenarii: inversion (black curve), without inversion (red curve).

the shell inversion enables to have good results both in ^{12}Be with S_{2n}=3.83 MeV (whereas the experimental value is S_{2n}=3.67$\pm$0.015 MeV) and in ^{14}Be with S_{2n}=1.33 MeV (whereas the experimental value is S_{2n}=1.34$\pm$0.11 MeV). Without inversion, it is not possible to bind enough the ^{14}Be. The s state is adjusted to be at the threshold as proposed in Ref. [66]. Once again we obtain a better agreement between the experimental and the theoretical spectrum for the 0^+ and 1^- states in ^{14}Be in case of the shell inversion. As seen previously in ^{12}Be calculation, we miss

the first experimental 2^+. And once again, the first excited experimental 2^+ state could be a $(2n)_{0^+}\otimes^{12}$Be(2^+) state as ^{12}Be has a 2^+ excited state at E^* =2.1 MeV. The difference between E^* =2.1 MeV and E_{2^+} =1.59 MeV being due to the residual energy typically negative.

Using the average value of a one- and a two-body operators developed in Eq.(3.78) and Eq.(3.94), we can calculate the average distance between the two neutrons of the halo, $\sqrt{\langle\rho^2\rangle}$ and between the center-of-mass of the halo neutrons and the center-of-mass of the core, $\sqrt{\langle\lambda^2\rangle}$; see Fig. 3.2. These values have been obtained experimentally by Sorlin et al. [119]. With inversion, we obtain $\sqrt{\langle\rho^2\rangle}$=4.9 fm which is in good agreement with the experimental value of 5.4$\pm$1.0 fm whereas with a normal shell ordering we get 8.7 fm. With inversion, $\sqrt{\langle\lambda^2\rangle}$ is equal to 4.0 fm which is in agreement with the experimental value of 4.5$\pm$ 1.0 fm whereas the result without inversion is 5.6 fm. Once again this result is in favor of the scenario with inversion.

3.8 Conclusions

The goal of this chapter has been to establish a formalism to explain the structure of two-neutron halo nuclei such as ^{14}Be . The p-p RPA is a three-body model that takes into account explicitly the two-body correlations in the core. We used a Woods-Saxon potential corrected by particle-vibration coupling for the neutron-core interaction and the effective Gogny D1S neutron-neutron interaction. It is worth noticing that such neutron-neutron interaction is not renormalized in this calculation. Thus we have shown the power of the Gogny interaction which initially has been parameterized for stable nuclei and it has given also good results near the drip-line. We have applied the p-p RPA method to different Beryllium isotopes from ^{8}Be to ^{14}Be. The first calculation with a ^{10}Be core gives indications on ^{8}Be and ^{12}Be. In this calculation, since the ^{11}Be spectrum is known experimentally, then once the ^{11}Be spectrum is adjusted through the α_l parameter, the calculation is parameter free. The good results obtained for ^{8}Be, which in our model is considered as ^{10}Be - 2 neutrons, represents a new vision of this system usually considered as a two α cluster. Results obtained for ^{12}Be from a ^{10}Be core are good. Then we applied the model to a ^{12}Be core. We proposed different scenarii for the input nuclei, as the unbound ^{13}Be is not well known. In one scenario, we proposed a normal single particle shell ordering as obtained in a standard Woods-Saxon potential. In the second scenario, we considered an inversion between the s and p shells. For both scenarii, we calculated the spectrum, rms and dipole strength for ^{14}Be. The results seem in favor of the inversion scenario. We find also the good two-neutron binding energy only in the case of the inversion. We obtain a too weak binding energy for ^{14}Be in the case without inversion. Between all the previous works on ^{14}Be, we are the only ones to propose this shell ordering. The inversion leads to the appearance of a p angular momentum contribution in the low energy continuum of ^{13}Be. We

have also given qualitative arguments to justify the possibility of an s-continuum state, coupled to an excited core and lower in energy than the p-state. The energy difference between the $1/2^+$ and the $1/2-$ states in ^{11}Be is 0.3 MeV. The same difference holds between the 0^+ and 1^- in ^{12}Be (cf. Table 3.2). Experimentally this last difference is about 0.4 MeV. One is tempted to argue that the same difference is expected in ^{13}Be as the residual interactions are supposed to be nearly the same in all these nuclei. Thus one can conclude that the difference in energy between the $1/2^+$ and the $1/2-$ in the ^{13}Be continuum is also to be expected of the order of 0.3-0.4 MeV. Interesting enough this is about the energy difference between the maxima of the s and p-state distributions found in Ch. 2 when trying to reproduce the experimental ^{13}Be spectrum.

Thus the structure work presented in this chapter is complementary to the work on reaction discussed in Ch.2. The neutron-neutron interaction was not taken explicitly into account in the fragmentation mechanism developed in chapter 2. We will see in the conclusion chapter of this thesis that the correction parameters extracted from the RPA model and from the fragmentation model to understand ^{13}Be are in agreement. One short term outlook to this chapter would be to do another reaction calculation taking into account both neutrons and using the RPA wave function as input within an Eikonal reaction mechanism.

Chapter 4

Study of neutron rich Sn, Ni isotopes for EURISOL

4.1 Purpose

Some nuclei are characterized by magic numbers of neutrons and protons for which their binding energy is enhanced. On the other hand, the changes of nuclear structure near the drip-lines are one of the key issues for nuclear physicists today. The validity of the present theories to describe the radioactive nuclei has been put under question. The first generation of RIB around the world and in particular the SPIRAL1 facility, has opened a first window on the light unstable nuclei region. The nuclei studied in the previous chapters belong to this category. Far away from the valley of stability the shell structure is predicted to be modified in terms of a weakening of the long-known magic numbers and the possible appearance of new shell gaps. For instance, it has been suggested that the harmonic oscillator shell gaps should become relevant when approaching the neutron drip-line. For medium-mass nuclei far away from stability the shell gaps at Z=28; N, Z=50, and N=82 are predicted to be weakened, and new gaps are expected to appear at N, Z=40, 70 when approaching the neutron drip-line.
The Skyrme and Gogny neutron-neutron (NN) effective interactions are determined from data on some double-magic nuclei (shell gaps and root mean square radii (rms)). We need information on double-magic nuclei further from stability in order to assess the validity of those interactions. In the last chapter of this thesis, we wish to study heavier neutron-rich nuclei. We propose a very preliminary study of what can be expected from the upcoming Radioactive Ion Beam (RIB) EURISOL (the European ISOL) facility. EURISOL will enable the study of nuclei richer in neutrons than those presently available. ISOL reads for Isotope Separation On-Line. Radioactive nuclides are produced by spallation, fission or fragmentation reactions of a projectile with a thick target. The products of these reactions diffuse out of the target, then they are

ionized, separated on-line, and reaccelerated. The secondary beams will be very intense at EURISOL which is one of two 'next generation' RIB infrastructures in Europe, the other project, FAIR (GSI, Germany), will use the in flight fragmentation technique.
To study the structure of more exotic nuclei and answer the questions raised by these observations, a facility like EURISOL is necessary to produce such nuclei in large amounts. Thanks to EURISOL new radioactive nuclei associated to usual magic proton and neutron numbers, like Z=28, N=20,28,50, ^{48,56,78}Ni, and Z=50, N=50,82, ^{100,132}Sn will be accessible and they will complete the set of the few key double-magic nuclei known in the valley of stability, ^{4}He, ^{16}O, ^{40,48}Ca, ^{208}Pb. To determine the evolution of the shell gap in the neighborhood of the expected new doubly magic nuclei several fundamental observables are or will be collected: S_n and S_{2n} deduced from mass measurements, excitation energies from Coulomb excitation experiments, and, the overlaps of wave functions, called spectroscopic factors (SF), to fix the single-particle picture. These SF and the single-particle configurations are deduced from neutron transfer reactions like (p,d) or (d,p). Using (d,p) reactions induced by the $^{133-134}$Sn SPIRAL2 beams, the most extreme cases will be $^{134-135}$Sn; with the EURISOL beams of $^{135-137}$Sn, we will access to the spectroscopy of $^{136-138}$Sn. For all these nuclei ($^{135-138}$Sn) the neutron break up threshold is low and we can expect that they will have no or very few (1 or 2) bound excited states. It means that, in order to clarify the shell picture in this region we will need to determine the energies of the unbound excited states and the SF from the light charged particle spectroscopy. The appropriate tool will be direct reactions on proton or deuteron targets and the detection of the light charged particle in coincidence with the heavy fragment detected in a spectrometer at forward angles. From the reconstruction of the kinematics of the light particle, by missing mass method, the excitation spectra of the heavy Tin product will be deduced and the (d,p) cross sections will be obtained.
Thus the physics case for EURISOL is very rich. Here we will concentrate on a subject close in spirit to the direct reaction studies presented in previous chapters. We present some tools used to extract structure information such as spectroscopic factors from experimental data. The study of these unstable nuclei is very challenging because new peculiarities have to be taken into account in the understanding of the reaction mechanisms. As these nuclei are very weakly bound they have only few bound excited states. They have also low-lying excited states in the continuum, and continuum couplings have to be included. Here we present some calculation made in the coupled channels formalism. We only couple to some bound excited states because coupling to the continuum has not been implemented in a standard way in numerical programmes. There are however somes works in progress such as those by Faes et al. [120] separating explicitly the contribution of the scattering states and the continuum and then using the SMEC (Shell Model Embedded in the Continuum) formalism [121]. We shall use the numerical code ECIS developed by J. Raynal [122] to perform the coupled channels calculations. Up-to-date we know only how to couple to bound states in the final nuclei.

These studies have to be made in order to determine which experiments will be feasible, with the future beams of the EURISOL facility. We plan to include the present results in an

EURISOL letter of intent. This work is in the following of works made by Valerie Lapoux in Ref. [123]. There the author presented some developments in the study of exotic nuclei with direct reactions. Their work has been performed in view of the letter of intent for the Spiral 2 facility [**?**]. The experiments that will be feasible with the EURISOL beams will be a continuity of those made on neutron-rich nuclei with Spiral 2. The topic of shell effects in exotic nuclei with direct reactions is part of the Spiral 2 physics case [125]. In the following, we consider more precisely the case of the Thin isotopes as an example of neutron-rich nuclei.

4.2 Beam intensities

The possible reactions will depend on the beam intensities. The first results from the study of the beam source have been provided by Strahinja Lukić [126]. In order to reach a good statistic, a high enough intensity is required. For the transfer reactions we are interested in, we need an intensity of at least 10^4 pps. With SPIRAL2 the last reaction feasible along the Tin isotopic chain is ^{134}Sn(d,p)^{135}Sn (^{134}Sn beam is expected to have $\sim 10^4$pps). With the maximum intensities from EURISOL, the reactions possible will be:

- ^{135}Sn(d,p)^{136}Sn I(^{135}Sn)=1.62×10^8pps
- ^{136}Sn(d,p)^{137}Sn I(^{136}Sn)=6.94×10^5pps
- ^{137}Sn(d,p)^{138}Sn I(^{137}Sn)=2.66×10^4pps.

4.3 Goals: Spectroscopy of Sn isotopes

According to the beam intensities provided by S. Lukić [126], the Sn isotope richer in neutron obtainable should be ^{138}Sn. In Fig. 4.1, we summarize the spectroscopic information presently available on the neutron-rich Sn isotopes. In heavy nuclei, the position of the drip-line is not known. Until now the heaviest Sn isotope known is ^{137}Sn. Only its ground state angular momentum and parity are known and its binding energy. Even if it is weakly bound, a bound excited state could be expected. Most probably, thanks to EURISOL, low-lying excited states will be discovered. The physics case is very challenging because of the high density of states so that the experimental set-up will have be very accurate in order to disentangle all these states of different parity. The knowledge of this region around the expected doubly magic ^{132}Sn is very important.
In an experiment, Radford et al. [127] have shown an unexpected behavior of the 2^+ state and of the transition strength $B(E2;0^+ \rightarrow 2^+)$ from the ground state to the lowest 2^+ for ^{132}Te,

^{134}Te, and ^{136}Te. The authors discovered for these isotopes that the $B(E2;0^+ \rightarrow 2^+)$ value decreases as the 2^+ state energy decreases; whereas in most isotopic chains, a decrease in E_{2^+} is accompanied by an increase in $B(E2;0^+ \rightarrow 2^+)$ as the states become collective. This unusual behavior has been explained by Terasaki et al. [128]. They studied Te and Sn isotopes around N=82 within a quasiparticle random phase approximation (QRPA), in conjunction with a simple schematic interaction. They identified the abnormal pattern of quadrupole collectivity in the neutron-rich Te isotope as due to the decrease of the neutron pairing gap going from ^{132}Te to ^{136}Te isotope. Then the authors predicted that the $B(E2;0^+ \rightarrow 2^+)$ in ^{132}Sn should be larger than in its immediate Sn neighbors. One can notice that this unexpected behavior is motivated by the observation of only few isotopes around ^{132}Sn. A larger range of Sn isotopes might be needed to confirm the above findings.

An important topic deals with the appearance of new magic numbers approaching the drip line. Several calculations predicted a so-called 'shell quenching' of the expected ^{132}Sn isotope, as observed in lighter nuclei where in regions of extreme isospin imbalance the effect of some magic numbers is eroded to the point of disappearence as in the case of N=20 and N=28. The strength of the ^{132}Sn shell has been shown not to reflect a doubly magic nuclide whose vibrational (spherical) properties are well established from spectroscopy studies. One hypothesis, from β-spectroscopy studies, was that the N=82 shell closure might be quenched [129]. In a recent experiment, Dworschak et al. [130] revealed a 0.5 MeV deviation of the binding energy of ^{134}Sn from the currently accepted value. It turned out that the strength of the ^{132}Sn shell closure was mistakenly determined to be too small. The corrected mass assignment of this neutron-rich nuclide restores the neutron-shell gap at N=82, previously considered to be a case of shell quenching. The study of these expected doubly magic nuclei is still open, and a facility as EURISOL is needed to reach heavy nuclei with such an extreme isospin imbalance.

In order to estimate the cross section, the kinematic calculations and to test the experimental tools, we can suppose, when excited states of the nucleus are unknown, that we are looking for excited states separated by 1 MeV below the S_n. Unbound states can be obtained experimentally by missing mass method, using kinematic variables, energies, angle in the laboratory of the backward emitted proton with a MUST2 telescope.
The estimate of the S_n and reaction Q-value comes from an extrapolation of the values given by the mass evaluation of Audi and Wapstra in 2003 [102].
The cross section estimate for (d,p) reactions to the ground state and to the first excited states are made by using the ECIS code [122]. The optical potentials for the entrance and exit channel are presented in the following section. A theoretical improvement will be to introduce for the p+nucleus system the JLM potential [131]. The JLM potential is obtained from a microscopic model and thus it is more physical significant than phenomenological potentials. In a first time it will be constructed from theoretical prescriptions (ex: 2pF form with parameters adjusted to have the values of the rms of proton and neutron densities given by the HFB theories [132]).

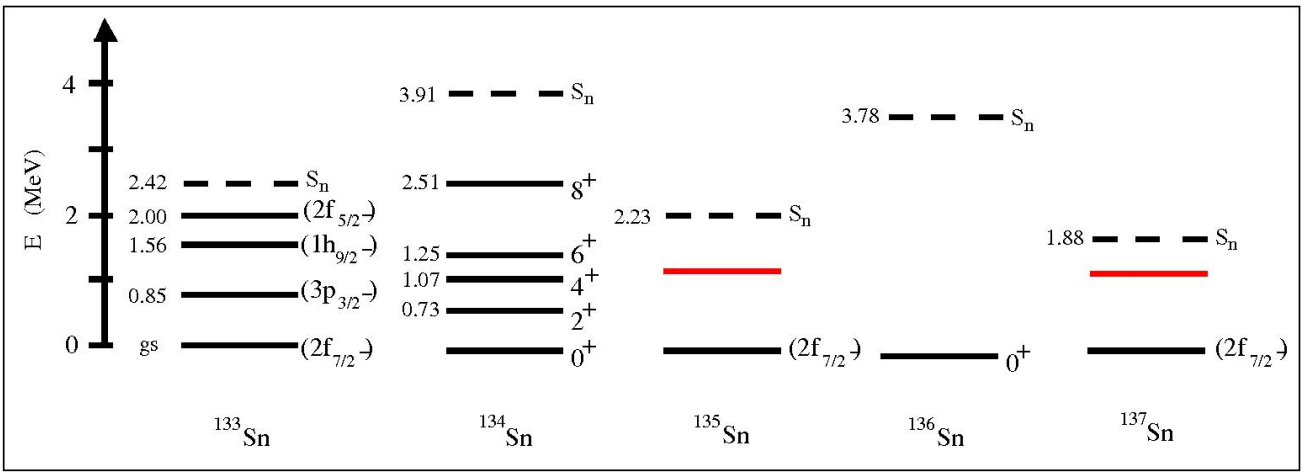

Figure 4.1: Spectroscopy of Sn isotopes (Taken from [124] and completed).

An important characteristic to determine is the selectivity of the reaction. To estimate reactions like A(d,p)A+1 at a given energy, preliminary calculations are needed: an estimate of the range of excited states that will be populated in the final nuclei A+1 will provide the selectivity of the transfer reaction (d,p) from the Sn beam.

4.4 Tools for the transfer calculations

4.4.1 Coupled-channels calculations

We want to use the coupled channels formalism in order to make some estimations of angular distribution for (d,p) reactions involving neutron-rich nuclei. We use the ECIS code to do these calculations. ECIS [122] is a numerical code which uses a sequential iteration method for solving the coupled differential equations arising from the scattering equation of two colliding nuclei. It also performs parameter searches to fit calculated results to experimental data. The inputs files, we used in this work, have been elaborated and provided by Valerie Lapoux from CEA-Saclay. The main ingredients of a (d,p) reaction calculation are: a deuteron-nucleus potential for the entrance channel, a proton-(nucleus + one neutron) for the exit channel. Then we used a semi-classical criterium in order to establish which channels are more likely populated. All these tools are presented in the following.

4.4.2 Ingredient:potentials

Phenomenological potentials: Daehnick, CH89

The Daehnick global potential [133] is a potential for deuteron-nucleus scattering fitted to data from 12 to 90 MeV and for $27 \leq A \leq 238$. It is a 11-parameter potential of the conventional form that fits all data analyzed to about 18% error on the rms calculation. Two of these parameters, V_R and a_I are functions of proton number and target mass, while five (V_R, a_0, W_S, W_D, V_{LS}) are smooth functions of bombarding energy. The remaining parameters: r_0, r_l, r_c, r_{LS}, a_{LS}, are constants. There is also a small three-parameter imaginary spin-orbit term, which requires short range and very small diffuseness.
The potential is of the form

$$\begin{aligned} V(r) = & - V_R f(r,r_0,a_0) + i4a_I W_D \frac{d}{dr} f(r,r_I,a_I) \\ & - iW_S f(r,r_I,a_I) \\ & + V_{LS} \left(\frac{\hbar}{m_\pi c}\right)^2 \left(\overrightarrow{L}.\overrightarrow{S}\right) \frac{1}{r}\frac{d}{dr} f(r,r_{LS},a_{LS}) + V_{Coul}, \end{aligned} \tag{4.1}$$

where the Woods-Saxon form factor f is given by

$$f(r,r_i,a_i) = \left[1 + exp\left(\frac{r - r_i A^{1/3}}{a_i}\right)\right]^{-1}. \tag{4.2}$$

A is the target mass number. The square of the pion Compton wavelength $(\hbar/m_\pi c)^2 \approx 2.00 fm^2$ is a conventional normalization factor. The Coulomb term is taken as the potential for a uniformly charged sphere of radius $R_c = r_c A^{1/3}$ and $r_c = 1.3$fm.
This parameterization has been obtained using data of $^{58-64}$Ni and $^{112-124}$Sn, therefore, in principle, it is not well suited to do calculation on neutron-rich nuclei. However, the Daehnick global potential can be used as a first approximation.

The Varner potential [134] is a global potential parameterized to fit nucleon-nucleus elastic scattering data. The CH89 parameterization proposes a decomposition in a Woods-Saxon potential with a volume real part, an imaginary volume and surface parts and a spin-orbit potential. Parameters have been adjusted in order to fit a lot of elastic scattering data of nucleon on stable nuclei, for masses between A=40 and A=209. But the validity of this potential has been shown to be even greater, so that it has been applied to lighter nuclei with success. One motivation of our study of drip-line nuclei is to test the validity of this global potential for high isospin nuclei. For the nuclei we are interested in different proton elastic scattering data sets have been considered during the parameterization: ^{58}Ni, ^{60}Ni, ^{62}Ni, ^{64}Ni, ^{116}Sn, ^{118}Sn, ^{120}Sn, ^{122}Sn, ^{124}Sn,

at 20.4 MeV. So this global potential can be used in a first approximation in calculations with ECIS.

Microscopic potentials, density-dependent potentials

The double folding potentials are calculated using the code written by D. T.Khoa [135], the double folding potential is described in Ref. [136]. The choice of the CDM3Y6 NN effective interaction is motivated by previous studies done for the analysis of the elastic scattering of exotic nuclei like ^{6}He [137]. The access to the executable of the code has been provided by Valerie Lapoux.

In the first order of the many-body theory, the microscopic nucleus-nucleus potential can be evaluated as an antisymmetrized HF-type potential for the dinuclear system

$$\begin{aligned} V &= V_D + V_{EX} \\ &= \sum_{i\in A_1, j\in A_2} \left[\langle ij|v_D|ij\rangle + \langle ij|v_{EX}|ji\rangle\right], \end{aligned} \tag{4.3}$$

where $|i>$ and $|j>$ refer to the single-particle wave functions of nucleons in the two colliding nuclei A_1 and A_2, respectively; v_D and v_{EX} are the direct and exchange parts of the effective NN interaction. By introducing the one-body density matrices $\rho_{1(2)}(\mathbf{r},\mathbf{r'})$ of the two colliding nuclei (with the diagonal terms giving the matter densities $\rho(\mathbf{r},\mathbf{r})$), one can explicitly write the energy-dependent direct and exchange potentials as

$$V_D(E,\mathbf{R}) = \int \rho_1(\mathbf{r}_1)\rho_2(\mathbf{r}_2)v_D(\rho,E,s)d\mathbf{r}_1 d\mathbf{r}_2 \tag{4.4}$$

with $\mathbf{s} = \mathbf{r}_2 - \mathbf{r}_1 + \mathbf{R}$,

$$V_{EX}(E,\mathbf{R}) = \int \rho_1(\mathbf{r}_1,\mathbf{r}_1+\mathbf{s})\rho_2(\mathbf{r}_2,\mathbf{r}_2-\mathbf{s})v_{EX}(\rho,E,s)exp\left[\frac{i\mathbf{k}(\mathbf{R})\mathbf{s}}{M}\right]d\mathbf{r}_1 d\mathbf{r}_2. \tag{4.5}$$

with $k(\mathbf{R})$ the relative-motion momentum given by

$$k^2(\mathbf{R}) = \frac{2mM}{\hbar^2}\left[E_{c.m.} - V(E,\mathbf{R}) - V_C(\mathbf{R})\right], \tag{4.6}$$

where $M = A_1A_2/(A_1+A_2)$ is the reduced mass, $E_{c.m.}$ the center of mass energy, E the projectile incident laboratory energy per nucleon, and m the bare nucleon mass. $V(E,\mathbf{R}) = V_D(E,\mathbf{R}) + V_{EX}(E,\mathbf{R})$ and $V_C(\mathbf{R})$ are respectively, the total nuclear and Coulomb potentials.
The direct (D) and exchange (E) potentials read as:

$$\begin{aligned} V_{D(EX)}(\rho,E,r) &= F(\rho)g(E)v_{D(EX)}(r), \\ g(E) &= 1 - 0.002E \\ F(\rho) &= C[1 + \alpha exp(-\beta\rho) - \gamma\rho] \end{aligned} \tag{4.7}$$

Table 4.1: Parameters of the CDM3Y6-PARIS NN effective interaction.

C	α	β (fm^3)	γ (fm^3)	K (MeV)
0.2658	3.8033	1.4099	4.0	252

In the double folding, we use the CDM3Y6-PARIS NN effective interaction whose parameters are presented in Table 4.1. with K the compressibility.

When theoretical densities are available, it is interesting to use the JLM potential to determine the nucleon-nucleus potential. This potential is likely to contain deeper information on peculiarities of exotic nuclei such as the appearance of a neutron skin for nuclei with a large neutron excess. Indeed the neutron skin should be visible looking at proton and neutron densities and seeing that the neutron density is far broader than the proton density. In our calculations, we use a JLM code provided by Tostevin to calculate the real and imaginary parts of the potential. The potential is then included as input in ECIS to calculate transfer reactions as well as elastic scattering.
Here are some test with JLM. We have made proton elastic scattering on ^{12}C using exactly the same parameters as Jouanne et al. for the ^{12}C density, see [138]. Comparing our JLM results with those obtained by C. Jouanne, we notice a slight difference between the two calculations that might be due to the fact that part of the Coulomb interaction is taken into account twice in our calculation, once in JLM potential and a second time in the ECIS calculation. But the difference between these two results is not striking. We have made also some comparison between JLM potential and the Varner potential. In this calculation ^{12}C proton and neutron densities are taken identical and parameterized as a Woods-Saxon with the following parameters, radius R_0 =2.1545 fm, diffuseness a=0.425 fm and ρ_0=0.207 fm^{-3}. These parameters are the same as those used in [138]. We notice in Fig. 4.3 and 4.4 that the surface's behavior of both potentials is similar. The surface is the relevant part of the potential for the direct reactions we are interested in, because they are peripheral. In Fig. 4.4, we compare the imaginary part of the Varner global potential to the JLM potential. We see that the imaginary JLM potential is similar to the surface part of the Varner potential. However, the imaginary JLM potential does not have a volume part.

As mentioned in previous chapters, the goal of reaction calculation is to make the bridge between experimental results and nuclear structure. Details of nuclear structure might be contained in the nuclear density determined theoretically from a nucleon-nucleon interaction. One ultimate goal of such approach is to disantangle what comes from the reaction and what comes from the structure in the experimental data. Once this is done, it is possible to go back to the nucleon-nucleon interaction and see which contribution is missing in it. Of course, we would need a very accurate understanding of each step of the calculation (structure and reaction) and of the experiment as well.

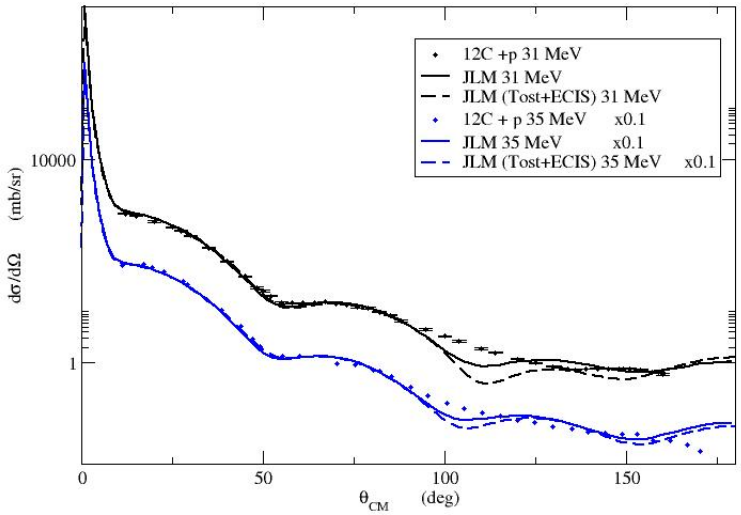

Figure 4.2: Differential cross section p+^{12}C elastic at 31 MeV (black curve) and 35 MeV (blue curve) with JLM using the prescription given in [138] for the ^{12}C density. Experimental points from [138]. Tostevin JLM version coupled to ECIS (dotted line). JLM version used in [138] (solid line).

In our present reaction calculation, we use a nuclear density provided by Antonov et al. [139]. The authors have calculated densities in several neutron-rich isotopes of Ni, Kr and Sn. The calculations are done within a selfconsistent HF+BCS framework using the Skyrme interaction SG2 of Sagawa and Van Gai [140]. We have verified the normalization of these densities in order to find the correct neutron and proton numbers. The rms have been determined and results are listed in Table 4.2. Fig. 4.5, Fig. 4.6 and Fig. 4.7 represent the neutron and the proton density respectively for $^{116-136}$Sn, $^{56-78}$Ni and $^{82-96}$Kr isotopes. In each isotope chain, going towards nuclei richer in neutron, the neutron volume increases considerably whereas the proton volume increases only slightly due to the proton-neutron interaction. This has the effect to form a core surrounded by a neutron skin in very neutron-rich nuclei. The topic of the neutron skin is treated at length in Ref. [139].

4.4.3 Discussions on the selectivity and on the angular momentum window

Here we give a semiclassical criterium to estimate approximately the most likely transfered momentum in a nucleon transfer reaction. It gives an idea about which final state will be populated

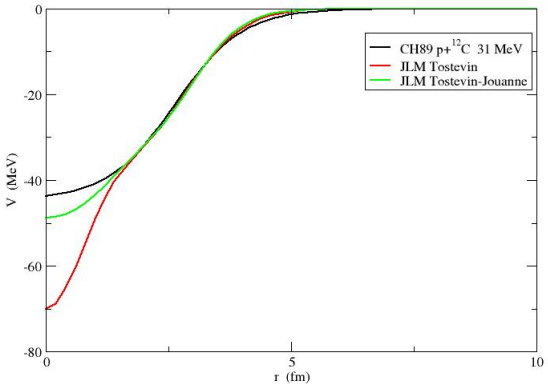

Figure 4.3: Real part of the potential used in 4.2 for p+^{12}C elastic, Daehnick global potential (black curve), JLM with 2pF density parameterization from the rms of ^{12}C.

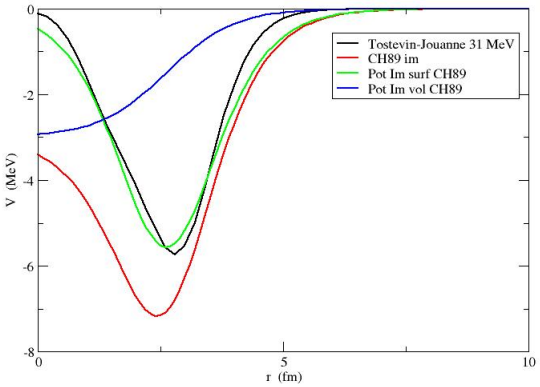

Figure 4.4: Same as Fig. 4.3 for the imaginary part of the potential.

with higher probability.

$$\begin{aligned} \delta L &\approx kR \\ k &= k_i - k_f \\ R &= R_p - R_t = R_0\left(A_p^{1/3} + A_t^{1/3}\right) \end{aligned} \tag{4.8}$$

Eqs.(4.8) are from Satchler [141]. For example if we consider a ^{132}Sn beam at 20 MeV/n Eqs.(4.8) give $\delta L \approx 3.2$, such that in ^{133}Sn the states more likely to be populated are $f_{7/2}$ and $p_{3/2}$.

4.5 Estimate of (d,p) cross sections

First, we have done some calculations at mass and energy corresponding to the parameterization of the Daehnick potential on reactions for which data are already available. This is only in order to check the validity of the procedure. As said previously, the Daehnick potential is a global potential parameterized to reproduce elastic scattering data without any coupled-channels. Here we consider differential elastic cross section of deuteron scattered by a ^{58}Ni at E$_d$=21.6 MeV (E$_d$ is the deuteron energy). In Fig. 4.8, we compare the different potentials we have in our tool box: Daehnick potential and the Khoa double folding potential (CDM3Y6-PARIS NN effective interaction) with two parameterizations for the deuteron: Gauss and fctH. We use the ^{58}Ni density provided by Antonov [139]. As the Khoa double folding method gives only the real part of

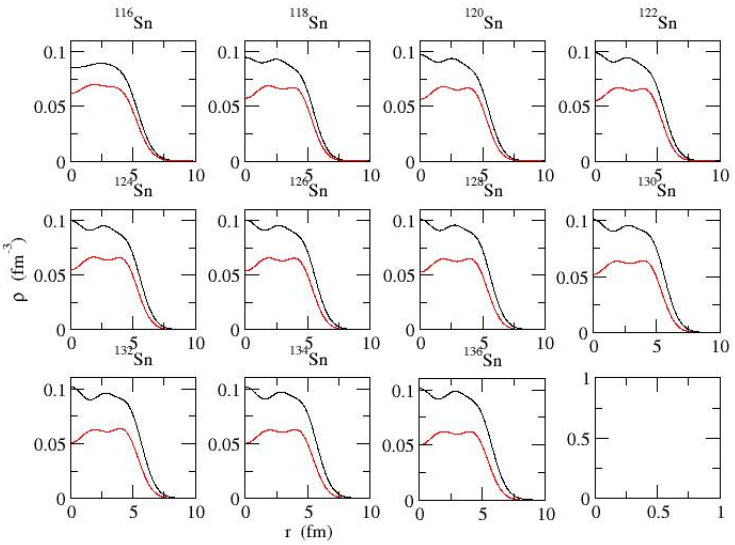

Figure 4.5: Neutron (black curve) and proton (red curve) densities for $^{116-136}$Sn provided by A. N. Antonov [139].

the d-nucleus potential, we use in the three cases the imaginary part coming from the Daehnick parameterization. Therefore differences between calculated differential cross sections observed in 4.9 are only due to the differences in the real part of the potential in Fig. 4.8. Experimental data are form Rawitscher [142]. In Fig. 4.9, we see that there is a good agreement between all the calculations and experimental data at small angles in center-of-mass. Of course the best results are obtained with the Daehnick potential which has been parameterized to reproduce the data. Results obtained with the fctH deuteron density are slightly better than those with Gaussian parametrization. In the following, we will use only the fctH deuteron density. The calculations presented are only preliminary and they intend to show what is to be expected from measurement at the EURISOL facility.

4.6 Some prospectives

The goal of this part is to give an idea of what could be possible to measure at the upcoming facility EURISOL. Of course it is a very preliminary study as EURISOL should be operative in more than 10 years from now. A prototype of (d,p) experiments has been done with stable nuclei (Xe beam) by G. Kraus et al. [143]. We use all the different tools presented previously and test the sensitivity of the results when changing some parameters. Until now we have made

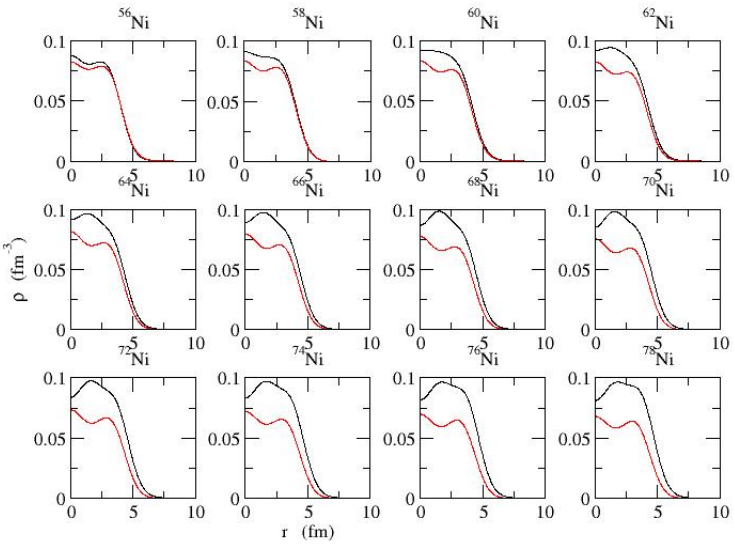

Figure 4.6: Neutron (black curve) and proton (red curve) densities for $^{56-78}$Ni provided by A. N. Antonov [139].

transfer calculations without transfer to the continuum. The coupling to the continuum is of a particular importance in the case of weakly bound nuclei. Some work has to be done in order to include this channel in the formalism used by ECIS. In Fig. 4.10, we compare different d-^{136}Sn real optical potentials at an energy of 20 MeV/n. The deuteron-nucleus potential is then used in the entrance channel of a (d,p) reaction calculation. It is interesting to have a look to the potentials and then proceed to the coupled channels calculation of the angular distributions.

In Fig. 4.11, we present the results of a coupled-channels calculation for the ^{136}Sn(d,p) reaction at 20 MeV/n. In the entrance channel for the deuteron-nucleus potential, we use the Daehnick global potential or the Khoa double folding potential with fctH deuteron density. In the exit channel here we use the Varner neutron-nucleus global potential. In the following, we present also some calculations made with JLM potential in the exit channel. As shown in Fig. 4.1, the spectroscopy of the final nucleus, here ^{137}Sn, is not known. So we only make some hypothesis. We choose its ground state as a $7/2^-$ state and we put a bound $3/2^-$ excited state at 1 MeV under the threshold. We go back to the fact that the global potentials used in the entrance and the exit channel, respectively Daehnick and Varner CH89 potentials, contain different order of interaction in order to reproduce the elastic experimental values. We have determined the elastic angular distribution with those two global potential once with coupling and once without coupling, see Fig. 4.12. At low angles in c.m., both results are equivalent, they differ only at larger angles where because of the couplings the elastic cross section is lowered. Even if using

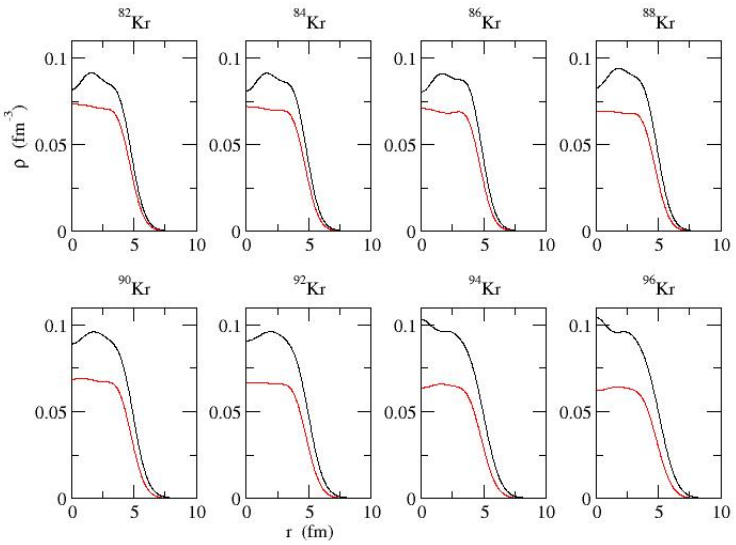

Figure 4.7: Neutron (black curve) and proton (red curve) densities for $^{82-96}$Kr provided by A. N. Antonov [139].

global potentials in a coupled-channels calculations induces a double counting of the couplings, global potentials are a simple way to obtain a good estimation of the angular ditributions in the the different channels.

The blue curve in Fig. 4.10 is a simulation of neutron skin. The neutron skin is the equivalent in heavy nuclei of the neutron halo phenomenon observed in light nuclei. In heavy neutron-rich nuclei it is expected to observe a core surrounded by neutrons. This phenomenon is partially observed in the densities depicted in Fig. 4.5, going closer to the neutron drip-line. In Fig. 4.10, we use a simulation of neutron skin. Fig. 4.5- 4.7 shows proton and neutron densities. In order to simulate the neutron skin, we fit the neutron density given by Antonov by a two-parameter Fermi (2pF) distribution. We have checked that the normalization of this 2pF density gives the correct neutron number. Finally we increase the radius and lower its amplitude in order to obtain a spatially extended neutron density without changing the neutron number. The 2pF density thus obtained gives the following matter rms: 6.58 fm instead of 4.87 fm from Antonov's densitity. The goal of this 'neutron skin' calculation is not so much to be realistic but rather to see the main effect of a neutron skin in (d,p) reactions. Results of the calculation with or without skin are presented in Fig. 4.14. We see that a change of 35% in the matter rms is quite difficult to observe with a (d,p) experiment. With (d,p) we are only sensitive to the matter density and it is impossible to be sensitive to neutron and proton matter separately.

Table 4.2: Matter rms obtained with Sn, Kr and Ni densities from Antonov [139].

Sn		Ni		Kr	
A	rms (fm)	A	rms (fm)	A	rms (fm)
116	4.68	56	3.70	82	4.16
120	4.68	60	3.77	86	4.20
122	4.70	62	3.82	88	4.24
124	4.72	64	3.85	90	4.28
126	4.74	66	3.96	92	4.34
128	4.76	68	3.93	94	4.41
130	4.78	70	3.97	96	4.47
132	4.81	72	4.01		
134	4.84	74	4.05		
136	4.87	76	4.08		
		78	4.17		

Table 4.3: Different depth of the imaginary surface potential used in Fig. 4.17.

	W_S Entrance channel	W_S Exit channel
Im0	11.3	10.23
Im1	13.3	12.23
Im2	15.3	14.23
Im3	17.3	16.23

It turns out that to get information on the neutron skin thickness one needs data obtained with probes having different sensitivities to the proton and neutron distributions. The methods for extracting the neutron skin thickness include hadron scattering, antiprotonic atoms, and parity violation scatterring, as well as the giant dipole resonance and spin-dipole resonance methods, [139]. (d,p) reactions are sensitive to matter distribution but it is not enough to extract the skin thickness.

In Fig. 4.17 and Fig. 4.18, we show the results of the coupled channels calculation for a ^{136}Sn(d,p) reaction with $3/2^-$ and $7/2^-$ as final states populated in ^{137}Sn. We vary the surface imaginary part of the entrance and exit potentials in order to simulate channels which are not taken into account explicitly. Indeed, approaching the drip-line the break up channel becomes very important because of the instability of these neutron-rich nuclei. As expected the increase of the strength of the surface imaginary part has the effect to lower the cross section in all the channels.

Finally we present some calculation made using the JLM potential in the exit channel. We still study the ^{136}Sn(d,p) reaction at an energy of 20 MeV/n. In Fig. 4.19, we compare the

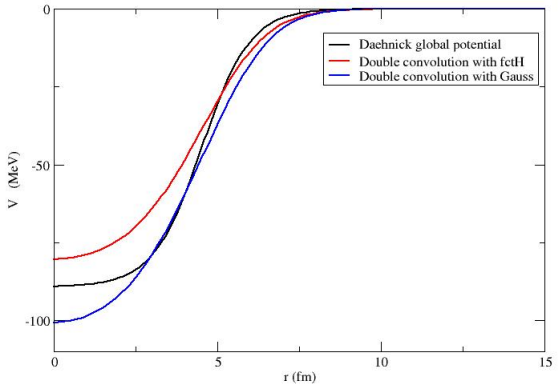

Figure 4.8: Comparison between potentials for ^{58}Ni+d. Daehnick global potential, Khoa double folding potential (CDM3Y6-PARIS NN effective interaction) with Gaussian density for the deuteron and Khoa double folding potential with fctH density for the deuteron.

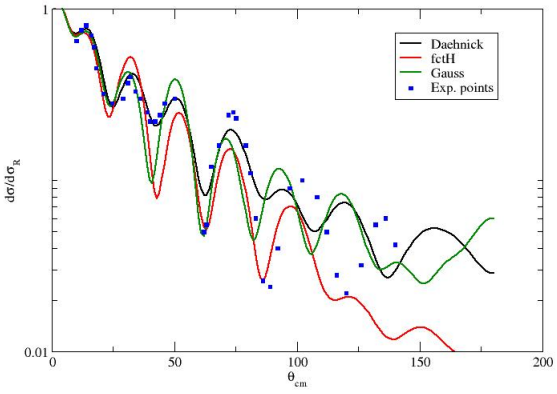

Figure 4.9: Elastic scattering angular distribution corresponding to potentials described in Fig. 4.8.

Varner global potential with the JLM potential. The densities provided by Antonov et al. were only for even Sn isotopes. We have obtained the matter density of ^{137}Sn by interpolation. Both real potentials are more or less equivalent. The difference comes from the imaginary part of the potential. Indeed the JLM imaginary potential corresponds approximately to the surface part of the Varner potential. The JLM potential seems not to have any volume imaginary part for such neutron-rich nuclei. Fig. 4.20 presents the same calculation that in Fig. 4.11 but with the JLM potential in the exit channel.

4.7 Conclusions and Outlooks

In this chapter, rather than obtaining definitive results, we have presented some tools necessay for the study of the data that might be obtained with EURISOL. We have estimated the angular distributions for the (d,p) reactions within the coupled-channels formalism. Calculations have been done with several optical potentials, in order to study the sensitivity to surface effects. Heavy exotic nuclei with neutron excess are in fact expected to present a neutron skin [132] . Transfer and break up reactions are expected to be sensitive to the presence of neutron skin. It is expected that information on the structure of such heavy nuclei might be obtained by including the main couplings to such reactions, in particular those to continuum final states or by using

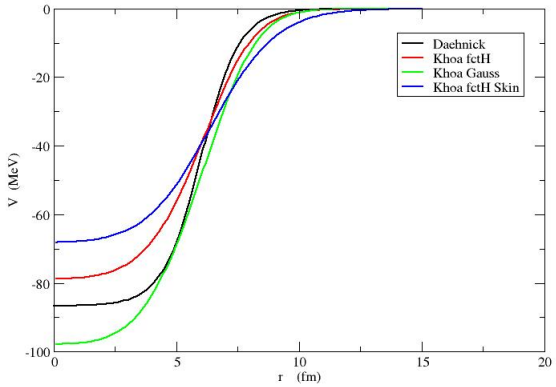

Figure 4.10: Deuteron-^{136}Sn potential at 20 MeV/n, Daehnick global potential (black curve), Khoa potential (CDM3Y6-PARIS NN effective interaction) with fctH (red curve) and with Gauss (green curve) deuteron densities and ^{136}Sn density from Antonov and with a simulation of a neutron skin (blue curve).

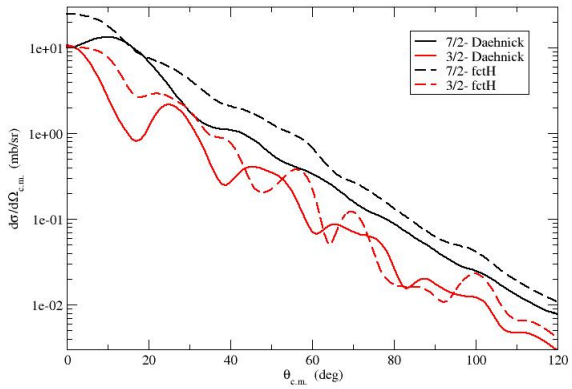

Figure 4.11: Angular distribution calculation for ^{136}Sn(d,p) at 20 MeV/n for $7/2^-$ (black) and $3/2^-$ (red) final channels with Daehnick deuteron global potential in the entrance channel (straight line) or Khoa double folding potential (CDM3Y6-PARIS NN effective interaction) with fctH deuteron density parameterization (dotted line). Varner global potential for the exit channel in both cases.

microscopic potentials which would fit transfer and elastic scattering data. The work presented here gives some cross section estimates, we have tested the sensitivity of the results to the parametrization of the potentials. In order to interpret the data from EURISOL, it will be useful to developed coupled-channels calculation using microscopic potentials. It will interesting to rely on studies such as the one developed by N. Keeley *et al.* in Ref. [144].

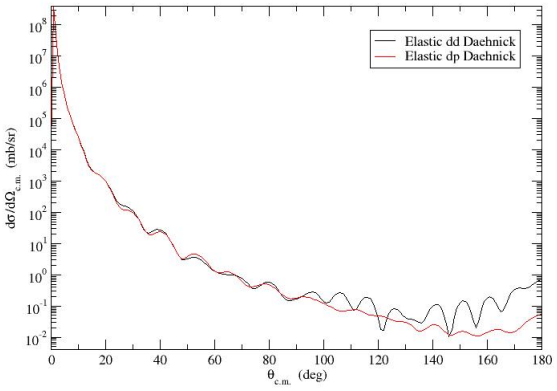

Figure 4.12: Elastic channel angular distribution for ^{136}Sn(d,p) at 20 MeV/n without coupling (black) and with coupling (red).

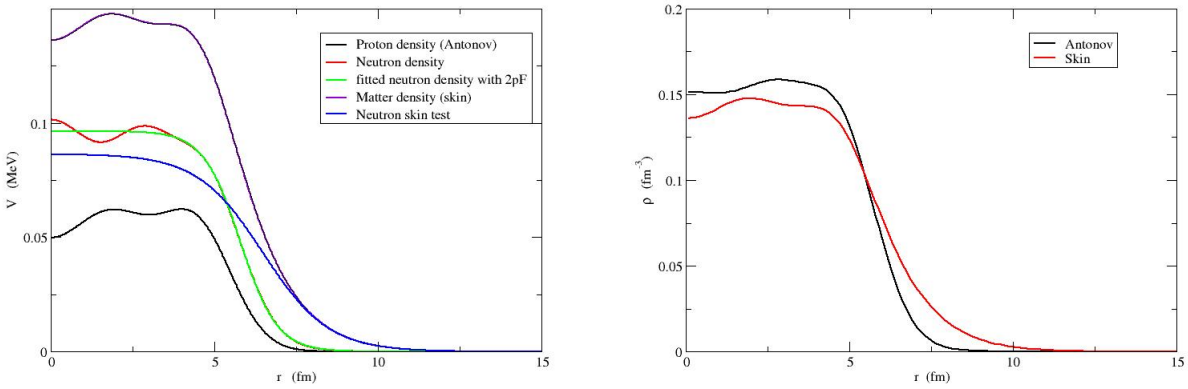

Figure 4.13: Neutron and proton density from Antonov and simulation of neutron skin in ^{136}Sn.

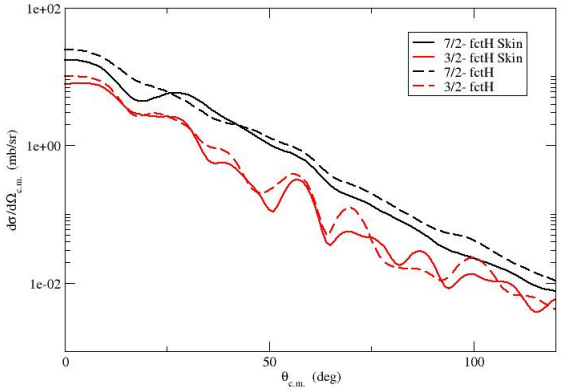

Figure 4.14: Angular distribution calculation for ^{136}Sn(d,p) at 20 MeV/n for $7/2^-$ (black) and $3/2^-$ (red) final channels with Khoa double folding potential (CDM3Y6-PARIS NN effective interaction) with fctH deuteron density parameterization with/without skin simulation.

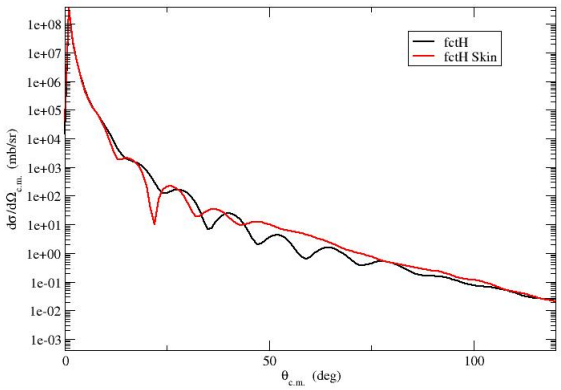

Figure 4.15: Elastic channel angular distribution corresponding to ^{136}Sn(d,p) at 20 MeV/n in Fig. 4.14.

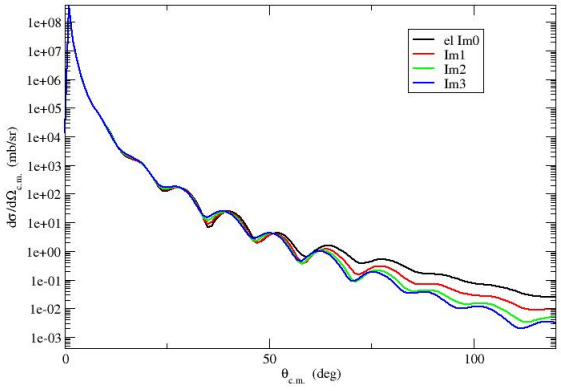

Figure 4.16: Elastic channel angular distribution corresponding to ^{136}Sn(d,p) at 20 MeV/n with progressive enhancement of the imaginary part in both entrance and final channels.

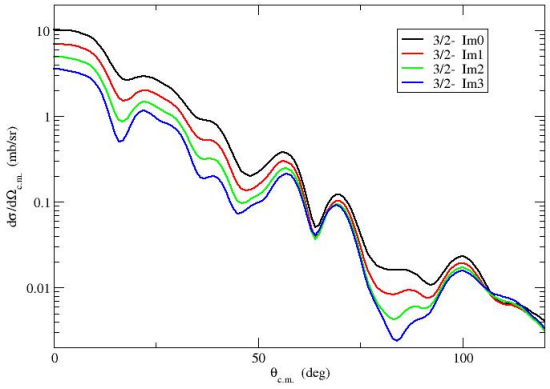

Figure 4.17: Angular distribution calculation for ^{136}Sn(d,p) at 20 MeV/n with $3/2^-$ final channel with enhancement of imaginary part in both the entrance and the final channels. Details on the parameters used are in Table 4.3

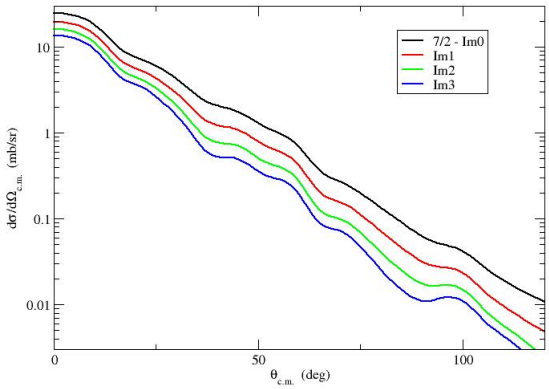

Figure 4.18: Same as in Fig. 4.17 for the $7/2^-$ final channel.

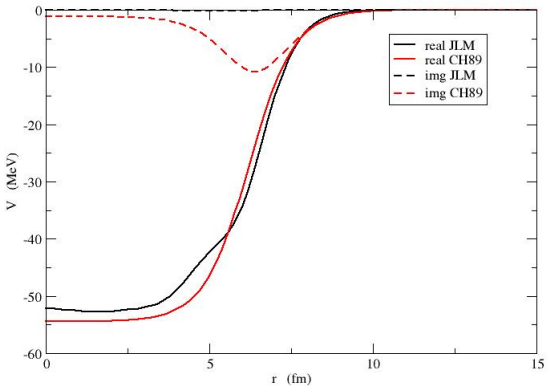

Figure 4.19: Comparison between p+^{137}Sn potential at 20 MeV/n. JLM potential (black curve), Varner CH89 potential (red curve). Real potential (solid curve), imaginary potential (dotted curve).

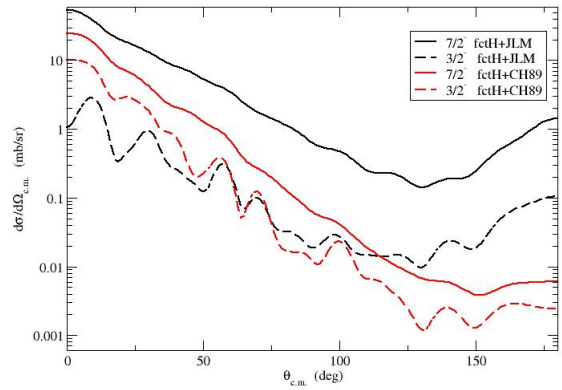

Figure 4.20: Angular distribution calculation for ^{136}Sn(d,p) at 20 MeV/n with $3/2^-$ final channel (dotted curve) and $7/2^-$ final channel (solid curve) with JLM potential (black curve), Varner global potential (red curve) and Khoa double folding in entrance channel (fctH deuteron density).

Conclusion

This thesis has been concerned with spectroscopic studies of exotic nuclei. We have mainly concentrated on the structure and reactions of two-neutron halo systems such as ^{11}Li and ^{14}Be. Our main goal has been to establish the single particle shell ordering in a series of cases through the use of pp-RPA structure calculations, appropriate reaction mechanism models and comparison with existing data. Two different formalisms have been developed in order to deal with the transfer to continuum and projectile fragmentation type of experiment. The goal of our work was to establish the form and parameters of the interaction potentials necessary to reproduce the shell ordering deduced from experimental spectra.The potentials found are strongly angular momentum dependent trought a surface term coming from particle-vibration couplings.

In the first part of this work, we have argued that, apart from the experimental difficulties, the transfer to the continuum method is well suited to study unbound systems such as ^{10}Li which are the building blocks of borromean nuclei. There is a very well tested theory to study such reactions, which allows to determine energy distributions for population of unbound states in absolute value. Provided the same information is available from the experimental point of view, the theory would allow the determination of the scattering length of *s*-states and the "resonance" energy of unbound single particle states, the associated l and j and the total strength. Those studies would eventually be used to determine the neutron-core interaction.

The advantage of our method is that the basic ingredient of the theory is the S-matrix describing the neutron-nucleus scattering. It can be calculated with an energy dependent potential which can incorporate consistently certain peculiarities of unbound nuclei such as ^{10}Li, whose continuum energy 0-0.5MeV range, for example, contains at least two states with l=0,1 obtainable only with two very different potential wells.

Furthermore the spin-orbit interaction can also be included so that at any energy the contribution from all states with given l and j can be obtained. This is very useful because not only the excitation of states of fixed angular momentum can be studied, but also the background due to the presence of all other possible angular momentum states can be calculated and in this way the strength of just one single particle state can be obtained unambiguously from data which would contain the contribution from all angular momenta. The theory has the correct behavior

when the continuum energy approaches threshold such that the contribution from virtual states can be distinguished from that from weakly bound or unbound states.

We have calculated neutron transition probabilities for going from an initial bound state in a nucleus to a scattering state including final state interaction with another nucleus. Our way of describing the final state interaction in the continuum is through an optical model S-matrix. A similar approach has been applied to the treatment of inelastic-like projectile excitations in which, following its interaction with the target, a neutron goes from a bound to an unbound state with final state interaction in the same nucleus. This is the process which creates ^{10}Li in the final state in the projectile-breakup-type of experiments [8]. By using such a procedure a very accurate theory of two neutron breakup could be obtained, incorporating properly the two step mechanism implicit in the formation of a neutron-core resonance state in reactions like $^{11}\mathrm{Li} + \mathrm{X} \rightarrow ^{10}\mathrm{Li}^{*} + \mathrm{n} \rightarrow ^{9}$Li+2n [10].

In fact ^{11}Li breakup and other 2n breakup reactions have often been treated as a process in which the two neutrons are emitted simultaneously in a single breakup process, which corresponds to the assumption of two highly correlated neutrons. This in principle could be improved by considering the second neutron which decays in flight from a resonant state, as seen for ^{6}He, by a breakup form factor different than that of the first neutron and by taking into account explicitly the sequential nature of the process.

In chapter 2, we have presented a model to study one neutron excitations from a bound initial state to an unbound resonant state in the neutron-core low energy continuum. This is the process by which unbound nuclei are created and studied via projectile fragmentation experiments [10]-[41, 83].

The model is based on a time dependent perturbation theory amplitude and the final state is described by an optical model S-matrix. It can be considered an evolution with respects to sudden and/or R-matrix theory models. The advantages are that the model can be applied to fragmentation from deeply bound states and to resonant and non resonant, large energy, continuum final states. Also core excitation effects can be modeled by an imaginary part of the neutron-core optical potential.

Comparison of the fragmentation formalism to the transfer to the continuum model shows that in principle projectile fragmentation does not reflect directly the properties of the neutron-core resonances because the reaction mechanism induces an extra phase with respect to the free particle neutron-core phase shift. It means that the measurements would probe an off-the-energy-shell S-Matrix. The distortion effects seem however small and negligible for the cases discussed in this work.

One neutron breakup can be studied in this way but also one step of two neutron breakup of a borromean nucleus. In this thesis we have presented some applications to both cases to study the properties of ^{11}Be continuum and of ^{13}Be. Our results are in agreement with the conclusions

of Ref. [54, 65] for ^{11}Be. Due to the structure inputs we use, in particular the position of the $p_{1/2}$ resonance, the ^{13}Be continuum spectrum obtained from fragmentation of ^{14}B or ^{14}Be shows essentially the effect of the continuum p and d-resonances. The s-state although present in the calculations almost disappears inside the tail of the p-state but it would still determine the ground state spin and parity of ^{13}Be. Obviously we cannot be conclusive on the structure of ^{13}Be because at the moment we have not attempted to fit experimental data but simply to develop a good reaction model. Furthermore our structure inputs, although reasonable, are extremely simple compared to the complexity of the nucleus under study. However preliminary comparisons seem to indicate the reliability of our model.

We have also shown that the excitation energy spectra of an unbound nucleus might reflect the structure of the parent nucleus from whose fragmentation they are obtained. In particular, in the case of ^{14}Be fragmentation, the initial state spectroscopic factors are not known experimentally, and the information from structure calculations indicate an important configuration mixing with components coupled to an excited ^{12}Be core. Thus the analysis of such spectra is expected to be even more complicated.

The goal of chapter 3 was to attempt some structure calculations to improve our understanding of such very complex nuclei. The p-p RPA is a good tool to study two-neutron halo nuclei. This is a three-body model that takes into account explicitly the two-body correlations in the core. We used a Woods-Saxon potential corrected by particle-vibration coupling for the neutron-core interaction and the effective Gogny D1S interaction for the neutron-neutron one. It is worth noticing that the neutron-neutron interaction is not renormalized in this calculation. This show the power of the Gogny interaction which initially has been parameterized for stable nuclei and gives also good results near the drip-line. We have applied the p-p RPA method to different Beryllium isotopes from ^{8}Be to ^{14}Be. The first calculation with a ^{10}Be core gives some results on ^{8}Be and ^{12}Be. In this calculation, as the ^{11}Be spectrum is already known, once the ^{11}Be spectrum is adjusted through the α_l parameter, then the calculation is parameter free. We can notice that the good results obtained for ^{8}Be, which in our model is considered as ^{10}Be - 2 neutrons, point out to an interpretation of ^{8}Be different from the usual vision of ^{8}Be as two α clusters.

Results obtained for ^{12}Be starting from a ^{10}Be core are good. Then we applied the model to a ^{12}Be core. We proposed different scenarii for the input nuclei, as the unbound ^{13}Be is not well known. In one scenario, we proposed a normal shell ordering as obtained in a standard Woods-Saxon potential. In the second scenario, we considered an inversion between the s and p shells. For both scenarii, we calculated the spectrum, rms and dipole strength for ^{14}Be. All results seem in favor of the inversion scenario. We found also the good two-neutron binding energy only in the case of the inversion. We can also notice that we obtained a too weak binding energy for ^{14}Be in the case without inversion. Between all previous works on ^{14}Be, we are the only ones to propose this shell ordering. The inversion leads to the appearance of a p angular momentum contribution at low energy in ^{13}Be, in agreement with the discussion in Ch.2.

To conclude this work we look at the α_l (cf. Eq.3.102)obtained from projectile fragmentation and from the RPA structure model. This parameter determines the strength of the surface potential coming from the particle-vibration couplings. The small differences the α_{frag} obtained with fragmentation and α obtained with RPA model are coming from the fact that in the RPA model the states are determined in a box whereas in the fragmentation calculation we determine the S-matrix then we find explicitly the position in energy of the resonance. For the d state it was expected to obtain nearly the same correction as the d resonance is known to be at an energy of 2.0 MeV and has been adjusted in both calculations in order to reproduce the experimentally known value. The p resonance has been obtained in a different way in the two methods. In the fragmentation model, the contribution of a p state near threshold was necessary to interpret the experimental n+^{12}Be spectrum. In the RPA model, the low energy p resonance has been adjusted in order to reproduce the binding energy of ^{14}Be. The agreement between these two independents findings is one of the main achievements of our approach.

Table 4.4: Energies and widths of unbound *p*- and *d*-states in ^{13}Be and corresponding strength parameters for the δV potential obtained in with fragmentation and in the RPA calculation.

	ε_{res} (MeV)	Γ_j (MeV)	α_{frag} (MeV)	α_{RPA} (MeV)
$1p_{1/2}$	0.67	0.28	8.34	8.9
$1d_{5/2}$	2.0	0.40	-2.36	-2.4

Finally, in the last chapter, we have been interested in devellopping some tools to study heavy neutron-rich nuclei, such as Tin isotopes. This prospective work was focused on the study of (d,p) reactions. Of course experimental data would be needed in order to determine quantities such as spectroscopic factors and parameters of an optical potential. These data will hopefully be obtained at the planned new facility EURISOL. We have shown that calculated results are very sensitive to the introduction of an imaginary surface potential taking into account the break up probability. This study has been performed at the CEA with Prof. Nicolas Alamanos and Dr. Valerie Lapoux and it has given me the possiblity to learn how to use new reaction tools such as the coupled channel formalism implemented in the ECIS code and the the double-folding technique to calculate microscopic optical potentials. Thus I have acquired expertise in one more approach to direct reaction calculations.

Bibliography

[1] I. Tanihata, H. Hamagaki, O. Hashimoto, Y. Shida, N. Yoshikawa, K. Sugimoto, O. Yamakawa, T. Kobayashi and N. Takahashi, Phys. Rev. Lett. **55** (1985) 2676; Phys. Lett. B **206**, 592 (1988).

[2] F. M. Marquès Moreno, Cours Ecole Joliot-Curie 2002.

[3] Y. Suzuki, Rezso G. Lovas, Kazuhiro Yabana and Kálmán Varga, *Structure and Reactions of light Exotic Nuclei*, Ed. Taylor & Francis (2003).

[4] Y. Tosaka and Y. Suzuki, Nucl. Phys. **A512** (1990) 46.

[5] Y. Tosaka, Y. Suzuki and K. Ikeda, Prog. Theor. Phys. **83** (1990) 1140.

[6] S. Mukai, S. Aoyama, K. Kato and K. Ikeda, Prog. Theor. Phys. **99** (1999) 381.

[7] M. V. Zhukov et al., Phys. Rep. **231** (1993) 150.

[8] M. Thoennessen, Proceedings the International School of Heavy-Ion Physics, 4th Course: Exotic Nuclei, Erice, May 1997, Eds. R. A. Broglia and P. G. Hansen, (World Scientific, Singapore 1998), pag.269.

[9] S. Pita, Thesis University Paris 6 (2000), IPN Orsay IPNO-T-00-11. S. Fortier, Proc.Int.Symposium on Exotic Nuclear Structures ENS 2000, Debrecen (Hungary), *Heavy Ion Physics* **12** (2001) 255.

[10] J. L. Lecouey, Ph. D. thesis, University of Caen, (2002), unpublished and nucl-ex/0310027.

[11] P. Santi, Ph. D. thesis, University of Notre Dame, (2000), unpublished. P. Santi et al., Phys. Rev. **C67** (2003) 024606.

[12] H. B. Jeppesen for ISOLDE Collaboration, REX-ISOLDE Collaboration, Nucl. Phys. **A748** (2005) 374; H.B. Jeppesen *et al.*, Phys. Lett. B **642** (2006) 449.

[13] C. Mahaux and R. Sartor, Adv. Nucl. Phys. **20** (1991) 1.

[14] R. Lipperheide, Nucl. Phys. **A89** (1966) 97.

[15] M. Zinser, F. Humbert, T. Nilsson, W. Schwab, H. Simon, T. Aumann, M. J. G. Borge, L. V. Chulkov, J. Cub, Th. W. Elze, H. Emling, H. Geissel, D. Guillemaud-Mueller, P. G. Hansen, R. Holzmann, H. Irnich, B. Jonson, J. V. Kratz, R. Kulessa, Y. Leifels, *et al.*, Nucl. Phys. **A619** (1997) 151.

[16] J. A. Caggiano, D. Bazin, W. Benenson, B. Davids, B. M. Sherrill, M. Steiner, J. Yurkon, A. F. Zeller and B. Blank, Phys. Rev. **C60** (1999) 064322.

[17] M. Thoennessen, S. Yokoyama, A. Azhari, T. Baumann, J. A. Brown, A. Galonsky, P. G. Hansen, J. H. Kelley, R. A. Kryger, E. Ramakrishnan, and P. Thirolf, Phys. Rev. **C59** (1999) 111.

[18] M. Chartier, J. R. Beene, B. Blank, L. Chen, A. Galonsky, N. Gan, K. Govaert, P. G. Hansen, J. Kruse, V. Maddalena, M. Thoennessen, R. L. Varner, Phys. Lett. **B510** (2001) 24.

[19] H. G. Bohlen, W. von Oertzen, Th. Stolla, R. Kalpakchieva, B. Gebauer, M. Wilpert, Th. Wilpert, A. N. Ostrowski, S. M. Grimes, T. N. Massey, Nucl. Phys. **A616** (1997) 254.

[20] B. M. Young et al., Phys. Rev. **C49** (1994) 279.

[21] A. Bonaccorso and D. M. Brink, Phys. Rev. **C38** (1988) 1776.

[22] A. Bonaccorso and D. M. Brink, Phys. Rev. **C43** (1991) 299.

[23] A. Bonaccorso and D. M. Brink, Phys. Rev. **C44** (1991) 1559.

[24] A. Bonaccorso and D. M. Brink, Phys. Rev. **C46** (1992) 700.

[25] A. Bonaccorso, Phys. Rev. **C51** (1995) 822.

[26] A. Bonaccorso, Phys. Rev. **C60** (1999) 054604.

[27] A. Bonaccorso, I. Lhenry and T. Suomijärvi, Phys. Rev. **C49** (1994) 329, and references therein.

[28] S. Galès, Ch. Stoyanov and A. I. Vdovin, Phys. Rep. **166** (1988) 125.

[29] S. Fortier, S. Galès, S. M. Austin, W. Benenson, G. M. Crawley, C. Djalali, J. S. Winfield and G. Yoo, Phys. Rev. **C41** (1990) 2689 .

[30] C. P. Massolo, S. Fortier, S. Galès, F. Azaiez, E. Gerlic, J. Guillot, H. Hourani, H. Langevin-Joliot, J. M. Maison, J. P. Shapira, and G. M. Crawley, Phys. Rev. **C43** (1991) 1687.

[31] G. H. Yoo, G. M. Crawley, N. A. Orr, J. S. Winfield, J. E. Finck, S. Galès, Ph. Chomaz, I. Lhenry and T. Suomijärvi, Phys. Rev. **C47** (1993) 1200.

[32] I. Lhenry. Ph. D. Thesis, IPNO-T92-01, Orsay April 1992 and I. Lhenry, T. Suomijärvi, Y. Blumenfeld, Ph. Chomaz, N. Frascaria, J. P. Garron, J. C. Roynette, J. A. Scarpaci, D. Beaumel, S. Fortier, S. Galès, H. Laurent, A. Gillibert, G. Crawley, J. Finck, G. Yoo and J. Barreto, Phys. Rev. **C54** (1996) 593.

[33] D. Beaumel, S. Fortier, S. Galès, J. Guillot, H. Langevin-Joliot, H. Laurent, J. M. Maison, J. Vernotte, J. A. Bordewijk, S. Brandenburg, A. Krasznahorkay, G. M. Crawley, C. P. Massolo, and M. Renteria, Phys. Rev. **C49** (1994) 2444.

[34] H. Laurent, J. A. Scarpaci, D. Beaumel, Y. Blumenfeld, S. Fortier, N. Frascaria, S. Galès, J. P. Garron, J. Guillot, I. Lhenry, J. C. Roynette, J. M. Maison, T. Suomijärvi, A. Gillibert, P. Roussel-Chomaz, and A. Van der Woude, Phys. Rev. **C52** (1995) 3066.

[35] G. Blanchon, A. Bonaccorso and N. Vinh Mau, Nucl. Phys. **A739** (2004) 259.

[36] G. Blanchon, A. Bonaccorso, A. Garcia-Camacho, D. M. Brink and N. Vinh Mau, Nucl. Phys. **A784** (2007) 49.

[37] G. Blanchon, A. Bonaccorso, D. M. Brink and N. Vinh Mau, Nucl. Phys. **A791** (2007) 303.

[38] P. G. Hansen and B. M Sherrill, Nucl. Phys. **A693** (2001) 133.

[39] N. Vinh Mau, Nucl. Phys. **A592** (1995) 33.

[40] G. Colò, T. Suzuki and H. Sagawa, Nucl. Phys. **A695** (2001) 167.

[41] L. V. Chulkov et al, Phys. Rev. Lett. **79** (1997) 201. L. V. Chulkov and G. Schrieder, Z. Phys. **A359** (1997) 231. D. Aleksandrov et al., Nucl. Phys. **A669** (2000) 51 and references therein.

[42] E. Garrido, D. V. Fedorov, A. S. Jensen, Nucl. Phys. **A708** (2002) 277 and references therein.

[43] I. J. Thompson and M. V. Zukhov, Phys. Rev. **C49** (1994) 1904.

[44] A. Bonaccorso and N. Vinh Mau, Nucl. Phys. **A615** (1997) 245.

[45] G. F. Bertsch, K. Hencken and H. Esbensen, Phys. Rev. **C57** (1998) 1366.

[46] J. Margueron, A. Bonaccorso and D. M. Brink, Nucl. Phys. **A720** (2003) 337.

[47] C. J. Joachain, *Quantum Collision Theory*, North-Holland Publishing Company, Amsterdam-Oxford, 1975.

[48] D. M. Brink, Phys. Lett. **40B** (1972) 37.

[49] L. Lo Monaco and D.M.Brink, J. Phys. G **11** (1985) 935.

[50] W. von Oertzen, Phys. Lett. **B151** (1985) 95.

[51] H. Hashim and D. M. Brink, Nucl.Phys. **A476** (1988) 107.

[52] K. W. McVoy, Nucl. Phys. **A115** (1968) 481. K. W. McVoy, P. Van Isacker, Nucl. Phys. **A576** (1994) 157.

[53] N. Vinh Mau and J. C. Pacheco, Nucl. Phys. **A607** (1996) 163.

[54] N. Fukuda, T. Nakamura, N. Aoi, N. Imai, M. Ishihara, T. Kobayashi, H. Iwasaki, T. Kubo, A. Mengoni, M. Notani, H. Otsu, H. Sakurai, S. Shimoura, T. Teranishi, Y. X. Watanabe, and K. Yoneda, Phys. Rev. **C70** (2004) 054606.

[55] F. M. Marqués et al., Phys. Rev. **C64** (2001) 061301(R). N.Orr, nucl-ex/0201017, Prog. Theor. Phys. Suppl. **146** (2003) 201.

[56] U. Datta-Pramanik et al., ENAM04 conference, https://www.phy.ornl.gov/enam04/WebTalks/

[57] B. Jonson, Phys. Rep. **389** (2004) 1.

[58] D.V. Aleksandrov et al., Sov. J. Nucl. Phys. **37**(3) (1983).

[59] A. N. Ostrowski et al., Z. Phys. **A343** (1992) 489.

[60] A. A. Korsheninnikov, E. Yu. Nikolskii, T. Kobayashi, D. V. Aleksandrov, M. Fujimaki, H. Kumagai, A. A. Ogloblin, A. Ozawa, I. Tanihata, Y. Watanabe, K. Yoshida, Phys. Lett. **B343** (1995) 53.

[61] A. V. Belozyorov, R. Kalpakchieva, Yu. E. Penionzhkevich, Z. Dlouhy, S. Piskor, J. Vincour, H. G. Bohlen, M. von Lucke-Petsch, A. N. Ostrowski, D. V. Alexandrov, E. Yu. Nikolskii, B. G. Novatskii, D. N. Stepanov, Nucl. Phys. **A636** (1998) 419; Phys. Rev. **C63** (2000) 014308.

[62] K. Adler, A. Bohr, T.Huus, B. Mottelson and A. Winther, Rev. Mod. Phys. **28** (1956) 432. K. Alder and A. Winther, *Electromagnetic Excitation* (North-Holland, Amsterdam, 1975).

[63] R. A. Broglia, and A. Winther, *Heavy Ion Reactions*, Benjamin, Reading, Mass, 1981.

[64] S. Kox, A. Gamp, C. Perrin, J. Arvieux, R. Bertholet, J. F. Bruandet, M. Buenerd, R. Cherkaoui, A. J. Cole, Y. El-Masri, N. Longequeue, J. Menet, F. Merchez, and J. B. Viano , Phys. Rev. **C35** (1987) 1678.

[65] P. Capel, D. Baye, Phys. Rev. **C70** (2004) 064605.

[66] M. Thoennessen, S. Yokoyama, and P.G. Hansen, Phys. Rev. **C60** (1999) 027303.

[67] H. Simon, T. Aumann, M.J.G. Borge, L.V. Chulkov, Th.W. Elze, H. Emling, C. Forssen, H. Geissel, M. Hellstrom, B. Jonson, J.V. Kratz, R. Kulessa, Y. Leifels, K. Markenroth, M. Meister, G. Munzenberg, F. Nickel, T. Nilsson, G. Nyman, V. Pribora, *et al.*, Nucl. Phys. **A734** (2004) 323.

[68] T. Nakamura, private communication.

[69] G.F. Bertsch, H. Esbensen, Ann. Phys. (N.Y.) 209 (1991) 327.

[70] I. J. Thompson and M. V. Zhukov, Phys. Rev. **C53** (1996) 708.

[71] J. C. Pacheco and N. Vinh Mau, Phys. Rev. **C65** 044004 (2002).

[72] P. Descouvemont, Phys. Lett. **B331** (1994) 271.

[73] P. Descouvemont, Phys. Rev. **C52** (1995) 704.

[74] A. Adahchour, D. Baye and P. Descouvemont, Phys. Lett. **B356** (1995) 445

[75] D. Baye, Nucl. Phys. **A627** (1997) 305.

[76] T. Tarutina, I. J. Thompson, J. A. Tostevin, Nucl. Phys. **A733** (2004) 53.

[77] V. Guimarães, J. J. Kolata, D. Bazin, B. Blank, B. A. Brown, T. Glasmacher, P. G. Hansen, R. W. Ibbotson, D. Karnes, V. Maddalena, A. Navin, B. Pritychenko, B. M. Sherrill, D. P. Balamuth and J. E. Bush, Phys. Rev. **C61** (2000) 064609.

[78] http://nucleardata.nuclear.lu.se/database/masses/

[79] M. Rodriguez-Gallardo, J. M. Arias, J. Gomez-Camacho, A. M. Moro, I. J. Thompson, and J. A. Tostevin, Phys. Rev. **C72**, (2005) 024007.

[80] I. J. Thompson, J. S. Al-Khalili, and J. A. Tostevin, Phys. Rev. **C47** (1993) R1364.

[81] M. Labiche, F. M. Marques, O. Sorlin, and N. Vinh Mau, Phys. Rev. **C60** (1999) 027303.

[82] J. M. Blatt and V. F. Weisskopf, *Theoretical Nuclear Physics*, Springer-Verlag, Berlin, 1979.

[83] H. Simon *et al.*, private communication.

[84] H. Simon, M. Meister, T. Aumann, M.J.G. Borge, L.V. Chulkov, U. Datta Pramanik, Th.W. Elze, H. Emling, C. Forssen, H. Geissel, M. Hellstrom, B. Jonson, J.V. Kratz, R. Kulessa, Y. Leifels, K. Markenroth, G. MÃijnzenberg, F. Nickel, T. Nilsson, G. Nyman, *et al.*, Nucl. Phys. **A791** (2007) 267.

[85] S. N. Ershov, B. V. Danilin, J. S. Vaagen, A. A. Korsheninnikov and I. J. Thompson, Phys. Rev. **C70** (2004) 054608.

[86] I. Brida, F.M. Nunes and B.A. Brown, Nucl. Phys. **A775** (2006) 23.

[87] J.F. Berger, M. Girod and D.Gogny, Comp. Phys. Comm., 63 (1991) 365.

[88] J.Dechargé and D.Gogny, Phys. Rev. **C21** (1980) 1568.

[89] N. Vinh Mau, *Theory of nuclear structure: Trieste Lectures 1969*, (IAEA, Vienna 1970).

[90] S. Grévy, O. Sorlin and N. Vinh Mau, Phys. Rev. **C56** (1997) 2885.

[91] F. Ajzenberg-Selove, Nucl. Phys. **A506**, 1 (1990).

[92] G. Audi and A. H. Wapstra, Nucl. Phys. **A595**, 409 (1995).

[93] M. Bernas, J.C. Peng and N. Stein, Phys. Lett. **B116** (1982) 7.

[94] H.T. Fortune, G.-B. Liuand, and D.E. Alburger, Phys. Rev. **C50** 1355 (1994).

[95] D.E. Alburger, D. P. Balamuth, J. M. Lind, L. Mulligan, K. C. Young, Jr., R. W. Zurmuhle, and R. Middleton, Phys. Rev. **C17** (1978) 1525.

[96] A. Navin, D. W. Anthony, T. Aumann, T. Baumann, D. Bazin, Y. Blumenfeld, B. A. Brown, T. Glasmacher, P. G. Hansen, R. W. Ibbotson, P. A. Lofy, V. Maddalena, K. Miller, T. Nakamura, B. V. Pritychenko, B. M. Sherrill, E. Spears, M. Steiner, J. A. Tostevin, J. Yurkon, and A. Wagner, Phys. Rev. Lett. **85** (2000) 266.

[97] H. Iwasaki, T. Motobayashi, H. Akiyoshi, Y. Ando, N. Fukuda, H. Fujiwara, Zs. Fulop, K. I. Hahn, Y. Higurashi, M. Hirai, I. Hisanaga, N. Iwasa, T. Kijima, T. Minemura, T. Nakamura, M. Notani, S. Ozawa, H. Sakurai, S. Shimoura, S. Takeuchi, *et al.*, Phys. Lett. **B481** (2000) 7.

[98] S. Shimoura, S. Ota, K. Demichi, N. Aoi, H. Baba, Z. Elekes, T. Fukuchi, T. Gomi, K. Hasegawa, E. Ideguchi, M. Ishihara, N. Iwasa, H. Iwasaki, S. Kanno, S. Kubono, K. Kurita, M. Kurokawa, Y.U. Matsuyama, S. Michimasa, K. Miller, *et al.*, Phys. Lett. **B654** (2007) 87.

[99] F.M. Nunes, I.J. Thompson, J.A. Tostevin, Nucl. Phys. **A703** (2002) 593-602.

[100] R. Gilman, H. T. Fortune, L. C. Bland, Rex R. Kiziah, C. Fred Moore, Peter A. Seid, C. L. Morris and W. B. Cottingame *et al.*, Phys. Rev **C30** (1984) 958.

[101] J. M. Wouters, *et al.*, Z. Phys. A 331 (1988) 229.

[102] G. Audi and A. H. Wapstra, Nucl. Phys. **A565** (1993) p1. and p66.

[103] T. Sugimoto, T. Nakamura, Y. Kondo, N. Aoi, H. Baba, D. Bazin, N. Fukuda, T. Gomi, H. Hasegawa, N. Imai, M. Ishihara, T. Kobayashi, T. Kubo, M. Miura, T. Motobayashi, H. Otsu, A. Saito, H. Sakurai, S. Shimoura, A.M. Vinodkumar, *et al*, Phy. Lett. **B654** (2007) 160.

[104] A. Ozawa, T. Suzuki, I. Tanihata, Nucl. Phys. **A693**(2001) 32.

[105] N. Vinh Mau, arXiv:0711.3171v1 [nucl-th] 20 Niv 2007.

[106] B. Alex Brown, in: M. de Saint Simon, O. Sorlin (Eds.), Proc. Int. Conf. on Exotic Nuclei and Atomic Masses, Editions Frontieres, Gif-sur-Yvette, 1995, pp. 451-460.

[107] F.C. Barker, Phys. Rev. **C59** (1999) 535.

[108] R. Sheer, H.T. Fortune, Phys. Rev. **C60** (2000) 064323.

[109] Yoshiko Kanada-Enýo and Hisashi Horiuchi, Phys. Rev. **C68** (2003) 014319.

[110] A.Bouyssy and N. Vinh Mau, Nucl. Phys. **A229** (1974) 1.

[111] G. Ripka and R. Padjen, Nucl. Phys. **A132** (1969) 489.

[112] A. Bouyssy and N. Vinh Mau, Nucl. Phys. **A224** (1974) 331.

[113] G. E. Brown and G. Jacob, Nucl. Phys. **42** (1963) 177.

[114] E. A. Sanderson, Phys. Lett. **19** (1965) 141.

[115] D. J. Rowe, Phys. Rev. **175**, 1283 (1968).

[116] J. da Providencia, Phys. Lett. **21**, 668 (1966).

[117] M. Zahar, M. Belbot, J. J. Kolata, K. Lamkin, R. Thompson, N. A. Orr, J. H. Kelley, R. A. Kryger, D. J. Morrissey, B. M. Sherrill, J. A. Winger, J. S. Winfield, A. H. Wuosmaa, Phys. Rev. **48** (1993) R1484.

[118] M. Labiche et al., Phys. Rev. Lett. **86** (2001) 4.

[119] M. Labiche, F. M. Marques, O. Sorlin and N. Vinh Mau, Phys. Rev. **C60** (1999) 027303.

[120] J. B. Faes and M. Ploszajczak, arXiv:0709.2971v1 [nucl-th] 19 sep 2007.

[121] K. Bennaceur, F. Nowacki, J. Okolowicz, M. Ploszajczak, Nucl. Phys. **A651** (1999) 289; ibid. **A671** (2000) 203.

[122] J. Raynal, Phys. Rev. **C23** (1981) 2571.

[123] Valerie Lapoux, Paris XI-Orsay 12th September 2005, *Structure de noyaux radioactifs faiblement liés par diffusion élastique et inélastique (p,p'), influence des couplages de ces noyaux exotiques sur les réactions directes.* internal report DAPNIA 05-502.

[124] LOI Spirale 2:
http://www.ganil.fr/research/developments/spiral2/files/LoIs_SP2_final/LoI_SP2_16_Lapoux.pdf

[125] Physics case SPIRAL2: http://www.ganil.fr/research/developments/spiral2/files/WB_SP2_Final.pdf

[126] GSI group, Strahinja Lukic, K. H. Schmidt *et al.* ; K. H. Schmidt private communication in 2006.

[127] D. C. Radford *et al.*, Phys. Rev. Lett. **88**, 222501 (2002).

[128] J. Terasaki, J. Engel, W. Nazarewicz and M. Stoitsov, Phys. Rev. **C66** (2002) 054313.

[129] I. Dillmann, K.-L. Kratz, A. Wohr, O. Arndt, B. A. Brown, P. Hoff, M. Hjorth-Jensen, U. Koster, A. N. Ostrowski, B. Pfeiffer, D. Seweryniak, J. Shergur, and W. B. Walters (the ISOLDE Collaboration), Phys. Rev. Lett. **91**, 162503 (2003).

[130] M. Dworschak, G. Audi, K. Blaum, P. Delahaye, S. George, U. Hager, F. Herfurth, A. Herlert, A. Kellerbauer, H.-J. Kluge, D. Lunney, L. Schweikhard, and C. Yazidjian, Phys. Rev. Lett. **100**, 072501 (2008).

[131] J.-P. Jeukenne, A. Lejeune and C. Mahaux, Phys. Rev. **C16** (1977) 80.

[132] M. V. Stoitsov, J. Dobaczewski, W. Nazarewicz, S. Pittel, and D. J. Dean, Phys. Rev. **C68** (2003) 054312.

[133] W. W. Daehnick, J. D. childs and Z. Vrcelj, Phys. Rev. **C21** (1980) 2253.

[134] R. L. Varner, Phys. Rep. **201** (1991) 57.

[135] D. T. Khoa, private communication to the SPhN group of CEA-Saclay.

[136] D. T. Khoa, W. von Oertzen, and H. G. Bohlen, Phys. Rev. **C49** (1994) 1652.

[137] V. Lapoux *et al.*, Phys. Rev. **C66** (2002) 034608.

[138] C. Jouanne *et al.*, Phys. Rev. **C72** (2005) 014308.

[139] P. Sarriguren, M. K. Gaidarov, E. Moya de Guerra, and A. N. Antonov, Phys. Rev. **C76** (2007) 044322. And private communication with A. N. Antonov.

[140] Nguyen van Giai and H. Sagawa, Phys. Lett. **B106**, 379 (1981).

[141] R. Satchler, *Direct Nuclear Reactions*, Ed. Clarendon Press NY (1983).

[142] G. H. Rawitscher, Phys. Rev. **C9** (1974) 6.

[143] G. Kraus *et al.*, Z. Phys. **A340** (1991) 339.

[144] N. Keeley, N. Alamanos, and V. Lapoux, Phys. Rev. **C69** (2004) 064604.

Appendix A

Modifications to the δ-interaction

Figure A.1: Graph of variables used in the calculation.

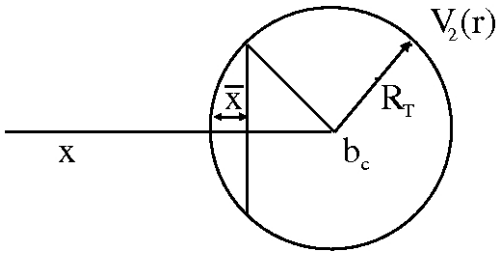

The purpose of this section is to justify the use of a δ-interaction as an approximation for the finite range n-target interaction and to derive Eq.(2.8). We then calculate

$$J = \int_{-\infty}^{\infty} dxdydzdz' \, \frac{e^{-(\gamma - ik)r}}{r^2} e^{-iq(z-z')} V_2(x - b_c, y, z'). \tag{A.1}$$

If γ is large the integral is concentrated near the surface of $V_2(r)$. To simplify the discussion put $q = 0$. Also, as in Sec. 2.3 put

$$\begin{aligned} e^{-(\gamma - ik)r} &\approx e^{-\alpha x} e^{-\alpha(y^2+z^2)/2x} \\ &\approx e^{-\alpha x} e^{-\alpha z^2/2R_0}, \end{aligned} \tag{A.2}$$

where $\alpha = \gamma - ik$ and we used the fact that the gaussian term $e^{-\alpha(y^2+z^2)/2x}$ gives the largest contribution at $R_0 = b_c - R_T$ which is the position of the surface of $V_2(r)$. To simplify further

the calculation we have neglected the y-dependence in Eq.(A.2) but kept the z-dependence so that the integral J will converge. Indicate $\bar{x} = x - \mathrm{R}_0 = x - (\mathrm{b}_c - \mathrm{R}_T)$. Take V_2(r) to be a square well potential of depth V_0 and radius R_T. Then

$$\int_{-\infty}^{\infty} V_2(x - b_c, y, z')\, dydz' = \pi V_0 \beta^2 = 2\pi V_0 R_T \bar{x} \tag{A.3}$$

where the upper limit of the two dimensional integral is given by $\beta^2 + (\bar{x} - \mathrm{R}_T)^2 = \mathrm{R}_T^2$ and $\beta^2 \approx 2\bar{x}\mathrm{R}_T$.

So that

$$\begin{aligned} J &= \frac{2\pi V_0 R_T}{b_c^2} \int dx e^{-\alpha x} \bar{x} \int dz e^{-\frac{\alpha z^2}{2R_0}} \\ &= \frac{V_0}{b_c^2} \sqrt{\frac{2\pi(b_c - R_T)}{\gamma - ik}} e^{-\alpha(b_c - R_T)} 2\pi R_T \int_{b_c - R_T}^{\infty} d\bar{x} e^{-\alpha\bar{x}} \bar{x} \\ &= \frac{V_0}{b_c^2} \sqrt{\frac{2\pi(b_c - R_T)}{\gamma - ik}} 2\pi \frac{R_T}{\alpha^2} e^{-\alpha(b_c - R_T)} \end{aligned} \tag{A.4}$$

The ratio of the integral J to the integral I of Eq.(2.25) is

$$\frac{J}{I} = \left(\frac{b_c - R_T}{b_c}\right)^{\frac{1}{2}} e^{(\gamma - ik)R_T} \frac{3}{2} \frac{v_2}{R_T^2(\gamma - ik)^2}, \tag{A.5}$$

Where we imposed that the strength of the δ-interaction be equal to the volume integral of the square well potential $v_2 = \frac{4}{3}\pi V_0 R_T^3$. Thus to represent the effect of a finite range potential by a δ-interaction when $\gamma \mathrm{R}_T >> 1$, replace

- (1) $\mathrm{b}_c \rightarrow \mathrm{b}_c - \mathrm{R}_T$ i.e. the interaction is at the surface of the target.
- (2) Multiply the strength of the interaction by $\frac{3}{2}\frac{1}{\mathrm{R}_T^2(\gamma - ik)^2}$.

This factor is less than one. The change (1) increases the breakup integral, the factor (2) decreases it.

Appendix B

Spin

B.1 Including spin

To include spin variables in the initial and final states is mainly an angular momentum coupling problem. The angle-spin wave function of the initial and final states are

$$\Psi_i(j_i,n_i,l_i,\theta,\phi) = \sum_{m_i\sigma_i} \langle j_i n_i | l_i m_i \frac{1}{2}\sigma_i\rangle Y_{l_i m_i}(\theta,\phi)\chi_{\sigma_i}(\rho) \tag{B.1}$$

$$\Psi_f(j_f,n_f,l_f,\theta,\phi) = \sum_{m_f\sigma_f} \langle j_f n_f | l_f m_f \frac{1}{2}\sigma_f\rangle Y_{l_f m_f}(\theta,\phi)\chi_{\sigma_f}(\rho). \tag{B.2}$$

We choose the quantization axis along the y-direction, such that $\phi = 0$. Then after integration over ρ, the angle spin part of the overlap Eq. (2.7) is:

$$\begin{aligned}\mathscr{D}(j_f n_f, j_i n_i) &= \sum_{m_f m_i \sigma} \langle j_f n_f | l_f m_f \frac{1}{2}\sigma\rangle \langle j_i n_i | l_i m_i \frac{1}{2}\sigma\rangle Y^*_{l_f m_f}(\theta,0) Y_{l_i m_i}(\theta,0) \\ &= \sum_{m_f m_i \sigma} (-1)^{m_f} \langle j_f n_f | l_f - m_f \frac{1}{2}\sigma\rangle \langle j_i n_i | l_i m_i \frac{1}{2}\sigma\rangle Y_{l_f m_f}(\theta,0) Y_{l_i m_i}(\theta,0),\end{aligned} \tag{B.3}$$

where we have put $Y^*_{lm} = (-1)^m Y_{l-m}$. Next we use the relation for coupling two spherical harmonics of the same argument and introduce the notation $\hat{i} = \sqrt{2i+1}$

$$Y_{l_i m_i}(\theta,0)Y_{l_f m_f}(\theta,0) = \sum_{LM}\langle LM|l_i m_i l_f m_f\rangle\langle L0|l_i 0 l_f 0\rangle \frac{\hat{l}_i\hat{l}_f}{\sqrt{4\pi}\hat{L}}Y_{LM}(\theta,0). \tag{B.4}$$

Substituting into the relation for $\mathscr{D}(j_f n_f, j_i n_i)$ there is a sum of products of three Clebsch-Gordan coefficients which reduces to a product of a Clebsch-Gordan coefficient and a 6-j symbol. Collecting together the terms evaluated above we get:

$$\mathscr{D}(j_f n_f, j_i n_i) = (-)^f \sum_{LM}\langle LM|j_i n_i j_f - n_f\rangle\langle L0|l_i 0 l_f 0\rangle \frac{\hat{l}_i\hat{l}_f\hat{j}_i\hat{j}_f}{\sqrt{4\pi}\hat{L}}Y_{LM}(\theta,0)\left\{\begin{array}{ccc} l_i & l_f & L \\ j_f & j_i & \frac{1}{2}\end{array}\right\}. \tag{B.5}$$

With the phase $f = n_f + l_f - j_f$

In this scheme the integral Eq.(2.24)

$$I_{l_i m_i, l_f m_f} = \int_{-\infty}^{\infty} dz e^{iqz} i^{l_i}\gamma h_{l_i}^{(1)}(i\gamma r)Y_{l_i,m_i}(\theta,0)k\frac{i}{2}h_{l_f}^{(-)}(kr)Y_{l_f,m_f}(\theta,0) \tag{B.6}$$

is substituted by a new integral I_{LM} defined as

$$I_{LM} = \int_{-\infty}^{\infty} dz e^{iqz} i^{l_i}\gamma h_{l_i}^{(1)}(i\gamma r)k\frac{i}{2}h_{l_f}^{(-)}(kr)Y_{L,M}(\theta,0). \tag{B.7}$$

Summing over n_f and averaging over n_i and using the orthogonality of the $\langle LM|j_i n_i j_f n_f\rangle$ coefficients while calculating $|A(j_f n_f, j_i n_i)|^2$ as in Eq.(2.20) we find that Eq.(2.23) can be replaced by:

$$\frac{dP_{in}}{d\varepsilon_f} = \frac{2}{\pi}\frac{v_2^2}{\hbar^2 v^2}C_i^2\frac{m}{\hbar^2 k}\sum_{LM}C(l_i,j_i,l_f,j_f;L)|\langle L0|l_i 0 l_f 0\rangle|^2|1-\bar{S}_{LM}|^2|I_{LM}|^2, \tag{B.8}$$

where

$$C(l_i,j_i,l_f,j_f;L) = \frac{(2j_f+1)(2l_i+1)(2l_f+1)}{4\pi(2L+1)}\left\{\begin{array}{ccc} l_i & l_f & L \\ j_f & j_i & \frac{1}{2}\end{array}\right\}^2. \tag{B.9}$$

A sum rule for $6-j$ symbols gives

$$\sum_{j_f}C(l_i j_i, l_f, j_f; L) = \frac{(2l_f+1)}{4\pi(2L+1)}. \tag{B.10}$$

On the other hand, if in Eq.(2.23) and (2.24) or (B.6) we use the angular momentum coupling formula for spherical harmonics

$$\sum_{m_i m_f} \langle LM|l_i m_i l_f m_f\rangle Y_{l_i m_i}(\theta,0) Y_{l_f m_f}(\theta,0) = \langle L0|l_i 0 l_f 0\rangle \frac{\hat{l}_i \hat{l}_f}{\sqrt{4\pi}\hat{L}} Y_{LM}(\theta,0), \tag{B.11}$$

then the relation between $I_{m_i m_f}$ and I_{LM} is

$$I_{l_i m_i, l_f m_f} = \sum_{LM} (-1)^{m_f} \langle LM|l_f - m_f l_i m_i\rangle \langle L0|l_i 0 l_f 0\rangle \frac{\hat{l}_i \hat{l}_f}{\sqrt{4\pi}\hat{L}} I_{LM} \tag{B.12}$$

and Eq.(2.23) is replaced by

$$\frac{dP_{in}}{d\varepsilon_f} = \frac{2}{\pi}\frac{v_2^2}{\hbar^2 v^2} C_i^2 \frac{m}{\hbar^2 k} \sum_{LM} \frac{(2l_f+1)}{4\pi(2L+1)} |\langle L0|l_i 0 l_f 0\rangle|^2 |1-\bar{S}_{LM}|^2 |I_{LM}|^2, \tag{B.13}$$

which could also be obtained using Eq.(B.10) in (B.8).

B.2 Spin

We take into account the spin part of the initial and final wave functions. The initial state is:

$$\Psi_{l_i,s_i}(\mathbf{r},\rho) = \sum_{m_i,\sigma_i} < l_i\ m_i\ s_i\ \sigma_i|J_i\ M_i > R_{l_i}(r) Y^*_{l_i m_i}(\widehat{\mathbf{r}}) \chi_{s_i\sigma_i}(\rho), \tag{B.14}$$

The conjugate of the scattering wave fonction is:

$$\begin{aligned}\left(\Psi^-_{\sigma_f,\mathbf{k}_f}(\mathbf{r},\rho)\right)^* &= 4\pi i \sum_{J_f M_f l_f m_f} \left(R_{l_f,J_f}(r,k_f)\right)^* (-i)^{l_f} Y^*_{l_f m_f}(\widehat{\mathbf{k}_f}) < l_f\ m_f\ s_f\ \sigma_f|J_f\ M_f > \\ &\times\ \varphi^{l_f}_{M_f J_f}(\widehat{\mathbf{r}},\rho)\end{aligned} \tag{B.15}$$

with

$$\varphi^{l_f}_{M_f J_f}(\widehat{\mathbf{r}},\rho) = \sum_{m_f,\sigma_f} < l_f\ m_f\ s_f\ \sigma_f|J_f\ M_f > Y_{l_f m_f}(\widehat{\mathbf{r}}) \chi_{s_f\sigma_f}(\rho)$$

The amplitude comes from

$$A_{fi} = \frac{1}{i\hbar}\int_{-\infty}^{\infty} dt \langle \Psi^-_{\sigma_f,\mathbf{k}_f}(\mathbf{r},\rho)|V_2(\mathbf{r}-\mathbf{R}(t))|\Psi_{l_i,s_i}(\mathbf{r},\rho)\rangle, \tag{B.16}$$

where $<|>$ means that we integrate over ρ, $\mathbf{r}$ and $\widehat{\mathbf{k}_f}$

Then

$$\begin{aligned} A_{fi} &= \sum_{all} R^*_{l_f} R_{l_i} Y^*_{l_f m_f}(\widehat{k_f}) < l_f\ m_f\ s_f\ \sigma_f | J_f\ M_f > \\ &\times < l_f\ m'_f\ s_f\ \sigma'_f | J_f\ M_f > Y_{l_f m'_f}(\widehat{r}) \chi_{s_f \sigma'_f}(\rho) \\ &\times < l_i\ m_i\ s_i\ \sigma_i | J_i\ M_i > Y_{l_i m_i}(\widehat{r}) \chi_{s_i \sigma_i}(\rho) \end{aligned} \tag{B.17}$$

with $all = J_f, M_f, l_f, m_f, m'_f, \sigma'_f, m_i, \sigma_i$.

Integrating on ρ, it gives $\delta_{s_i s_f}, \delta_{\sigma_i \sigma'_f}$ and

$$\begin{aligned} A_{fi} &= \sum_{all} R^*_{l_f} R_{l_i} Y^*_{l_f m_f}(\widehat{k_f}) < l_f\ m_f\ s_f\ \sigma_f | J_f\ M_f > \\ &\times < l_f\ m'_f\ s_f\ \sigma'_f | J_f\ M_f > Y_{l_f m'_f}(\widehat{r}) \\ &\times < l_i\ m_i\ s_f\ \sigma'_f | J_i\ M_i > Y_{l_i m_i}(\widehat{r}) \end{aligned} \tag{B.18}$$

with $all = J_f, M_f, l_f, m_f, m'_f, \sigma'_f, m_i$.

We call

$$a_{l_f m_f l_i m_i J_f} = \int_{-\infty}^{+\infty} \left(R_{l_f, J_f}(\mathbf{b}, z, k_f) \right)^* R_{l_i}(\mathbf{b}, z)\, dz \tag{B.19}$$

then the amplitude is written as

$$\begin{aligned} A_{fi} &= \sum_{all} a_{l_f m'_f l_i m_i J_f} Y^*_{l_f m_f}(\widehat{k_f}) < l_f\ m_f\ s_f\ \sigma_f | J_f\ M_f > \\ &\times < l_f\ m'_f\ s_f\ \sigma'_f | J_f\ M_f >< l_i\ m_i\ s_f\ \sigma'_f | J_i\ M_i > \end{aligned} \tag{B.20}$$

We calculate the probability

$$\begin{aligned} |A_{fi}|^2 &= \sum_{all} a_{l_f m'_f l_i m_i J_f} Y^*_{l_f m_f}(\widehat{k_f}) < l_f\ m_f\ s_f\ \sigma_f | J_f\ M_f > \\ &\times < l_f\ m'_f\ s_f\ \sigma'_f | J_f\ M_f >< l_i\ m_i\ s_f\ \sigma'_f | J_i\ M_i > \\ &\times a^*_{l'_f m'''_f l_i m'_i J'_f} Y_{l'_f m''_f}(\widehat{k_f}) < l'_f\ m''_f\ s_f\ \sigma_f | J'_f\ M'_f > \\ &\times < l'_f\ m'''_f\ s_f\ \sigma''_f | J'_f\ M'_f >< l_i\ m'_i\ s_f\ \sigma''_f | J_i\ M_i > \end{aligned} \tag{B.21}$$

with $all = J_f, M_f, l_f, m_f, m'_f, \sigma'_f, m_i, J'_f, M'_f, l'_f, m''_f, m'''_f, \sigma''_f, m'_i$.

We integrate on $\widehat{k_f}$, that gives $\delta_{l_f l'_f}, \delta_{m_f m''_f}$

$$\begin{aligned} |A_{fi}|^2 &= \sum_{all} a_{l_f m'_f l_i m_i J_f} < l_f\ m_f\ s_f\ \sigma_f | J_f\ M_f > \\ &\times < l_f\ m'_f\ s_f\ \sigma'_f | J_f\ M_f >< l_i\ m_i\ s_f\ \sigma'_f | J_i\ M_i > \\ &\times a^*_{l'_f m'''_f l_i m'_i J'_f} < l_f\ m_f\ s_f\ \sigma_f | J'_f\ M'_f > \\ &\times < l_f\ m'''_f\ s_f\ \sigma''_f | J'_f\ M'_f >< l_i\ m'_i\ s_f\ \sigma''_f | J_i\ M_i > \end{aligned} \tag{B.22}$$

with $all = J_f, M_f, l_f, m_f, m'_f, \sigma'_f, m_i, J'_f, M'_f, m'''_f, \sigma''_f, m'_i$.

We sum on m_f and σ_f with,

$$\sum_{m_1 m_2} < j_1\ m_1\ j_2\ m_2 | J\ M >< j_1\ m_1\ j_2\ m_2 | J'\ M' >= \delta_{JJ'} \delta_{MM'} \tag{B.23}$$

then it gives $\delta_{J_f J'_f}, \delta_{M_f M'_f}$,

$$\begin{aligned} |A_{fi}|^2 &= \sum_{all} a_{l_f m'_f l_i m_i J_f} < l_f\ m'_f\ s_f\ \sigma'_f | J_f\ M_f > \\ &\times < l_i\ m_i\ s_f\ \sigma'_f | J_i\ M_i > \\ &\times a^*_{l'_f m'''_f l_i m'_i J_f} < l_f\ m'''_f\ s_f\ \sigma''_f | J_f\ M_f > \\ &\times < l_i\ m'_i\ s_f\ \sigma''_f | J_i\ M_i > \end{aligned} \tag{B.24}$$

with $all = J_f, M_f, l_f, m'_f, \sigma'_f, m_i, m'''_f, \sigma''_f, m'_i$.

We sum on final polarizations and and average on the initial ones. We change the indexation as follows: $m'_f \to m_f, m'''_f \to m'_f, \sigma'_f \to \sigma$,
$\sigma''_f \to \sigma', s_f \to s$

$$\begin{aligned} |A_{fi}|^2 &= \frac{1}{2J_i+1} \sum_{all} a_{l_f m_f l_i m_i J_f} < l_f\ m_f\ s\ \sigma | J_f\ M_f > \\ &\times < l_i\ m_i\ s\ \sigma | J_i\ M_i > \\ &\times a^*_{l_f m'_f l_i m'_i J_f} < l_f\ m'_f\ s\ \sigma' | J_f\ M_f > \\ &\times < l_i\ m'_i\ s\ \sigma' | J_i\ M_i > \end{aligned} \tag{B.25}$$

with $all = J_f, M_f, l_f, m_f, \sigma_f, m_i, m'_f, \sigma'_f, m'_i, M_i$.

Then we use the relation:

$$\begin{aligned} &\sum_{\varepsilon} < a\ \alpha\ b\ \beta | e\ \varepsilon >< e\ \varepsilon\ d\ \delta | c\ \gamma > \\ &= \sum_{f\phi} < b\ \beta\ d\ \delta | f\ \phi >< a\ \alpha\ f\ \phi | c\ \gamma > \widehat{e}\widehat{f} W(abcd;ef) \end{aligned} \tag{B.26}$$

where $\widehat{x} = \sqrt{2x+1}$ and $W(abcd;ef)$ the Racah symbol.

We have to switch some component in the Clebsch-Gordan coefficients. We use the relation:

$$< j_1\ m_1\ j_2\ m_2 | J\ M >= (-1)^{j_1 - J + m_2} \sqrt{\frac{2J+1}{2j_1+1}} < J\ M\ j_2\ -m_2 | j_1\ m_1 > \tag{B.27}$$

$$\begin{aligned} |A_{fi}|^2 &= \frac{1}{2J_i+1} \sum_{all} a_{l_f m_f l_i m_i J_f} < l_f\ m_f\ s\ \sigma | J_f\ M_f > \\ &\times\ a^*_{l_f m'_f l_i m'_i J_f} < l_i\ m'_i\ s\ \sigma'_f | J_i\ M_i > \\ &\times\ (-1)^{l_f - J_f + \sigma'} \sqrt{\frac{2J_f+1}{2l_f+1}} < J_f\ M_f\ s\ -\sigma' | l_f\ m'_f > \\ &\times\ (-1)^{l_i - J_i + \sigma'} \sqrt{\frac{2J_i+1}{2l_i+1}} < J_i\ M_i\ s\ -\sigma' | l_i\ m'_i > \end{aligned} \tag{B.28}$$

with $all = J_f, M_f, l_f, m_f, \sigma, m_i, m'_f, \sigma', m'_i, M_i$.

We sum on M_i and M_f

$$\begin{aligned} |A_{fi}|^2 &= \left(\widehat{J_i}\right)^{-1} \sum_{all} (-1)^{l_f - J_f + l_i - J_i + 2\sigma'} \frac{\widehat{J_f}}{\widehat{l_f}\widehat{l_i}}\ a_{l_f m_f l_i m_i J_f} a^*_{l_f m'_f l_i m'_i J_f} \\ &\times\ \sum_{f\phi} < s\ \sigma\ s\ -\sigma' | f\ \phi >< l_f\ m_f\ f\ \phi | l_f\ m'_f > \widehat{J_f}\widehat{f} W(l_f s l_f s; J_f f) \\ &\times\ \sum_{g\beta} < s\ \sigma\ s\ -\sigma' | g\ \beta >< l_i\ m_i\ g\ \beta | l_i\ m'_i > \widehat{J_i}\widehat{g} W(l_i s l_i s; J_i f) \end{aligned} \tag{B.29}$$

with $all = J_f, l_f, m_f, \sigma, m_i, m'_f, \sigma', m'_i$.

We sum on σ and $\sigma' \rightarrow \delta_{fg}\delta_{\phi\beta}$

$$\begin{aligned} |A_{fi}|^2 &= \sum_{all}(-1)^{l_f-J_f+l_i-J_i+1}\frac{\left(\widehat{J_f}\right)^2\left(\widehat{f}\right)^2}{\widehat{l_f}\widehat{l_i}}\, a_{l_f m_f l_i m_i J_f} a^*_{l_f m'_f l_i m'_i J_f} \\ &\times < l_f\ m_f\ f\ \phi | l_f\ m'_f > W(l_f s l_f s; J_f f) \\ &\times < l_i\ m_i\ g\ \phi | l_i\ m'_i > W(l_i s l_i s; J_i f) \end{aligned} \tag{B.30}$$

with $all = J_f, l_f, m_f, m_i, m'_f, m'_i, f, \phi$.

Using

$$\left\{ \begin{array}{ccc} j_1 & j_2 & j_3 \\ J_1 & J_2 & J_3 \end{array} \right\} = (-1)^{j_1+j_2+J_1+J_2} W(j_1 j_2 J_2 J_1; j_3 J_3), \tag{B.31}$$

we get

$$\begin{aligned} |A_{fi}|^2 &= \sum_{all}(-1)^{-(l_f+J_f+l_i+J_i+1)}\frac{\left(\widehat{J_f}\right)^2\left(\widehat{f}\right)^2}{\widehat{l_f}\widehat{l_i}}\, a_{l_f m_f l_i m_i J_f}(\mathbf{b}, k_f)\ a^*_{l_f m'_f l_i m'_i J_f}(\mathbf{b}, k_f) \\ &\times < l_f\ m_f\ f\ \phi | l_f\ m'_f > \left\{ \begin{array}{ccc} l_f & s & J_f \\ s & l_f & f \end{array} \right\} \\ &\times < l_i\ m_i\ f\ \phi | l_i\ m'_i > \left\{ \begin{array}{ccc} l_i & s & J_i \\ s & l_i & f \end{array} \right\} \end{aligned} \tag{B.32}$$

with $all = J_f, l_f, m_f, m_i, m'_f, m'_i, f$ and ϕ. One could go further in the calculation using the fact that one of the 6J component (s) is equal to 1/2.Then we do the integration over the impact parameter.

B.3 Correspondence between B.1 and B.2

David does a calculation with every couplings and finds finaly an easier relation. Coming back to

$$\begin{aligned} |A_{fi}|^2 &= \frac{1}{2J_i+1}\sum_{all} a_{l_f m_f l_i m_i J_f} < l_f\ m_f\ s\ \sigma | J_f\ M_f > \\ &\times < l_i\ m_i\ s\ \sigma | J_i\ M_i > \\ &\times a^*_{l_f m'_f l_i m'_i J_f} < l_f\ m'_f\ s\ \sigma' | J_f\ M_f > \\ &\times < l_i\ m'_i\ s\ \sigma' | J_i\ M_i > \end{aligned} \tag{B.33}$$

with $all = J_f, M_f, l_f, m_f, \sigma, m_i, m'_f, \sigma', m'_i, M_i$.
We put the m dependence out of the a (all the Y) and using

$$Y_{l_i m_i}(\theta,0) Y_{l_f m_f}(\theta,0) = \sum_{LM} < l_i\ m_i\ l_f\ m_f | L\ M >< l_i\ 0\ l_f\ 0 | L\ 0 > \sqrt{\frac{(2l_i+1)(2l_f+1)}{4\pi(2L+1)}} Y_{LM}(\theta,0), \tag{B.34}$$

we obtain

$$\begin{aligned} |A_{fi}|^2 &= \frac{1}{2J_i+1} \sum_{all} a_{l_f l_i J_f} < l_f\ m_f\ s\ \sigma | J_f\ M_f > \\ &\times < l_i\ m_i\ s\ \sigma | J_i\ M_i > \\ &\times a^*_{l_f l_i J_f} < l_f\ m'_f\ s\ \sigma' | J_f\ M_f > \\ &\times < l_i\ m'_i\ s\ \sigma' | J_i\ M_i > \\ &\times < l_i\ m_i\ l_f\ m_f | L\ M >< l_i\ 0\ l_f\ 0 | L\ 0 > Y_{LM}(\theta,0) \\ &\times < l_i\ m'_i\ l_f\ m'_f | L\ M' >< l_i\ 0\ l_f\ 0 | L\ 0 > Y^*_{LM'}(\theta,0) \frac{(2l_i+1)(2l_f+1)}{4\pi(2L+1)} \end{aligned} \tag{B.35}$$

with $all = J_f, M_f, l_f, m_f, \sigma, m_i, m'_f, \sigma', m'_i, M_i, L, M, M'$.

Then we have

$$\begin{aligned} |A_{fi}|^2 &= \frac{1}{2J_i+1} \sum_{all} |a_{l_f l_i J_f}|^2 < l_f\ m_f\ s\ \sigma | J_f\ M_f > \\ &\times < l_i\ m_i\ s\ \sigma | J_i\ M_i >< l_f\ m'_f\ s\ \sigma' | J_f\ M_f > \\ &\times < l_i\ m'_i\ s\ \sigma' | J_i\ M_i >< l_i\ m_i\ l_f\ m_f | L\ M > \\ &\times |< l_i\ 0\ l_f\ 0 | L\ 0 >|^2 < l_i\ m'_i\ l_f\ m'_f | L\ M' > \end{aligned}$$

$$Y_{LM}(\theta,0) Y^*_{LM'}(\theta,0) \frac{(2l_i+1)(2l_f+1)}{4\pi(2L+1)}. \tag{B.36}$$

We use

$$\begin{aligned} \sum_{m_i m_f \sigma} (-1)^{m_f} &< l_f\ -m_f\ 1/2\ \sigma | J_f\ M_f >< l_i\ m_i\ 1/2\ \sigma | J_i\ M_i >< l_i\ m_i\ l_f\ m_f | L\ M > \\ &= < J_i\ M_i\ J_f\ M_f | L\ M > \left\{ \begin{array}{ccc} l_i & l_f & L \\ J_f & J_i & 1/2 \end{array} \right\} \end{aligned} \tag{B.37}$$

and

$$\begin{aligned}|A_{fi}|^2 &= \frac{1}{2J_i+1}\sum_{all}|a_{l_f l_i J_f}|^2|<l_i\,0\;l_f\,0|L\,0>|^2 \\ &\times <J_i\,M_i\,J_f\,M_f|L\,M>\left\{\begin{array}{ccc} l_i & l_f & L \\ J_f & J_i & 1/2\end{array}\right\} \\ &\times <J_i\,M_i\,J_f\,M_f|L\,M'>\left\{\begin{array}{ccc} l_i & l_f & L \\ J_f & J_i & 1/2\end{array}\right\} Y_{LM}(\theta,0)Y^*_{LM'}(\theta,0)\frac{(2l_i+1)(2l_f+1)}{4\pi(2L+1)}\end{aligned} \tag{B.38}$$

with $all = J_f, M_f, l_f, M_i, L, M, M'$.

Finally,

$$\begin{aligned}|A_{fi}|^2 &= \frac{1}{2J_i+1}\sum_{all}|a_{l_f l_i J_f}|^2|<l_i\,0\;l_f\,0|L\,0>|^2 \\ &\times <J_i\,M_i\,J_f\,M_f|L\,M>\left\{\begin{array}{ccc} l_i & l_f & L \\ J_f & J_i & 1/2\end{array}\right\}^2 \\ &\times <J_i\,M_i\,J_f\,M_f|L\,M'>Y_{LM}(\theta,0)Y^*_{LM'}(\theta,0)\frac{(2l_i+1)(2l_f+1)}{4\pi(2L+1)}\end{aligned} \tag{B.39}$$

with $all = J_f, M_f, l_f, M_i, L, M, M'$.

then we sum on M_i and M_f that gives $\delta_{MM'}$

$$\begin{aligned}|A_{fi}|^2 &= \frac{1}{2J_i+1}\sum_{all}|a_{l_f l_i J_f}|^2|<l_i\,0\;l_f\,0|L\,0>|^2 \\ &\times \left\{\begin{array}{ccc} l_i & l_f & L \\ J_f & J_i & 1/2\end{array}\right\}^2 |Y_{LM}(\theta,0)|^2\frac{(2l_i+1)(2l_f+1)}{4\pi(2L+1)}.\end{aligned} \tag{B.40}$$